# CHARACTERIZATION OF FLOW FREEZING IN SMALL CHANNELS FOR ICE VALVE APPLICATIONS

by

**Aakriti Jain**

**A Dissertation**

*Submitted to the Faculty of Purdue University*

*In Partial Fulfillment of the Requirements for the degree of*

**Doctor of Philosophy**


School of Mechanical Engineering

West Lafayette, Indiana

December 2019

## THE PURDUE UNIVERSITY GRADUATE SCHOOL
## STATEMENT OF COMMITTEE APPROVAL

**Dr. Suresh V. Garimella, Co-chair**

School of Mechanical Engineering

**Dr. Justin A. Weibel, Co-chair**

School of Mechanical Engineering

**Dr. Amy Marconnet**

School of Mechanical Engineering

**Dr. Steven D. Pekarek**

School of Electrical Engineering

**Approved by:**

Dr. Nicole Key

# ACKNOWLEDGMENTS

I would like to thank my academic advisors, Dr. Suresh V. Garimella and Dr. Justin A. Weibel, whose guidance and support has been invaluable to my educational, professional and personal development. Their constant encouragement has been vital in developing both critical and creative thinking during my research at Purdue University. I am fortunate to have learnt from them both and I truly appreciate their commitment and understanding as mentors.

I would also like to thank Dr. Amy Marconnet and Dr. Steven D. Pekarek for serving on my committee. Their guidance and feedback had been valuable to my research.

I would like to acknowledge Dr. Yonghua Huang, from Shanghai JiaoTong University, without whose collaboration this research would not have been possible. And Dr. Ankur Miglani, whose ingenuity and perseverance helped this work reach completion.

I am also truly grateful for the help and cooperation of my colleagues and labmates, who have unconditionally shared their time and ideas with me; they have also inspired me and humored me through the tough times. Special thanks to Dr. Carolina Mira Hernández, Dr. Gaurav Patankar, Dr. Todd Kingston, Dr. Aditya Chandramohan, Dr. Kevin Drummond, Sara Lyons, Rishav Roy, Srivathsan Sudhakar, and Matthew Clark.

I would like to thank my friends, both at home and at Purdue, who never let me give up. I would like to thank Apoorv Maheshwari, whose faith in me is stronger than my own and who unconditionally supported and encouraged me through and through, and Saurabh Misra, whose optimism and guidance has kept me sane in the most stressful times. Special thanks to Aparajita Nath, Sugandha Srivastava, and Vivek Singla.

Finally, I would like to express my gratitude for the love of my parents, Dr. Rakesh and Dr. Rachana Jain, siblings, Aishwarya and Anmol, and both my grandmothers, who have stood by me and my decisions like unwavering pillars of support. And it is through them that I find the strength and confidence to follow my own path and be where I am.

# TABLE OF CONTENTS

# LIST OF TABLES

# LIST OF FIGURES

# ABSTRACT

Freezing of water flowing through a small channel can be used as an efficient and cost-effective flow control mechanism for microfluidic platforms. Ice valves provide a leak-proof, non-invasive and high-pressure-tolerant method of flow control compared to their conventional micromechanical counterparts. To develop, design and implement ice valves an understanding of the processes and parameters that govern ice formation in small channels is required. The aim of this dissertation is to understand the freezing process of water flowing in small diameter channels and the factors affecting the same, so as to develop a simple physical model that predicts the ice growth process and channel closing time. Further, a stand-alone ice valve formation device is developed that is suitable for implementation in high-pressure microfluidic applications.

While ice valves have various advantages over conventional microvalves, their successful implementation is in part hindered due to their long response time. An understanding of the factors that affect the ice growth process during flow freezing in small diameter channels (commonly encountered in microfluidic devices) would allow reduction and control of the response time of ice valves. In this dissertation, freezing in a pressure-driven water flow through a channel is investigated using measurements of external channel wall temperature and flow rate synchronized with high-speed visualization. A test setup is designed and demonstrated to control the external cooling boundary conditions during visualization of the ice formation modes in a small channel; the external wall thermocouple and the water flow rate readings are synchronized with the high-speed images. Firstly, the effect of water flow rate on the freezing process is investigated in a glass channel of 500 $\mu$m inner diameter in terms of the external wall temperature, the growth duration of different ice modes, and the channel closing time. Freezing initiates as a thin layer of ice dendrites that grows along the inner wall and partially blocks the channel, followed by the formation and inward growth of a solid annular ice layer that leads to complete flow blockage and ultimate channel closure. A simplified analytical model is developed to determine the factors that govern the annular ice growth, and hence the channel closing time. The model identifies the water flow rate and the channel diameter as the two key parameters that govern the channel closing time. For a given channel, the model predicts that the annular ice growth is driven purely by conduction due to the temperature difference between the outer channel wall and the equilibrium ice-water

interface. The flow rate affects the initial temperature difference, and thereby has an indirect effect on the annular ice growth. Higher flow rates require a lower wall temperature to initiate ice nucleation and result in faster annular ice growth (and shorter closing times) than at lower flow rates.

The effect of the channel diameter on the flow freezing process and the channel closing time is further studied. The freezing process is investigated for a pressure-driven water flow (0.3 ml/min flow rate) through three glass channels with inner diameters (IDs) 500 $\mu$m, 300 $\mu$m and 100 $\mu$m, respectively. The modes observed in the freezing process are the same for all the channel diameters; complete channel closure is caused by annular ice growth. The growth time of the annular ice is observed to decrease monotonically with the channel ID such that the 100 $\mu$m channel has the shortest closing time. Specifically, the mean closing time of 100 $\mu$m ID channel is measured to be 0.25 s at a water flow rate of 0.3 ml/min, which is an extremely short closing time given the relatively high flow rate compared to studies in the existing literature. A model-based analysis of the freezing process shows that the annular closing time is a function of the total latent heat released by the freezing mass (which varies as square of the channel diameter), the thermal resistance to the radial flow of this latent heat, and the temperature difference between the ice-water interface and the external wall temperature (which drives the conduction of the latent heat). A comparison of magnitudes of these terms for the presented cases leads to the conclusion that the total latent heat released is the dominating controlling factor in closing time calculations and, hence, the closing time varies directly with the of the channel inner diameter.

After studying the key factors governing the freezing process and the closing time during flow freezing in a small channel, an ice value is designed and demonstrated for a microfluidic application. While the ice valves are simple to operate, the current cooling methods used to induce ice formation are bulky, expensive, or have a footprint much larger than the valve itself, which are all detrimental to application in complex multi-channel microfluidics. A novel design for an effective, simple and stand-alone cryogen-driven ice-valve cooling mechanism is proposed and demonstrated for use on microfluidic chips, for possible application in high-pressure microfluidics. The presented design is compact enough to be interfaced with complex microfluidic devices, can precisely control the location of ice valve formation, and also prevents wastage of cryogen by self-

shutting the cryogen flow when cooling is not required. The ice valve is formed by freezing the water flow in channels, by placing the cooler in contact with the channel substrate. The valve formation is studied in water flowing through square cross-section channels, fabricated on PMMA and glass chips, using high-speed visualization synchronized with temperature data. The effect of flow rate (10 μl, 20 μl, 30 μl, and 40 μl), channel size (50 μm, 100 μm, and 200 μm), and channel material (PMMA and Glass) on the response time is analyzed; the pressure tolerance of the valves is also reported. Additionally, the cooling process of the chip is modeled using both 3-D numerical and simplified 1-D analytical models to obtain an estimate of the response time and the channel pitch that could help develop guidelines for incorporation of the proposed cooling mechanism into chip design.

# CHAPTER 1. INTRODUCTION

## 1.1 Background

Microfluidic systems have been widely employed for chemical and biomedical analysis as they enable high analytical throughput at low sample volumes as well as ease and flexibility of integration on small chips at low cost [1–5]. Flow control is a crucial step that enables complex functionality in such microfluidic systems through flow management of the reagents, including routing, timing and segregation. However, miniaturization and commercialization of fully integrated microfluidic systems have been hindered by the lack of reliable flow control elements [6]. Flow control in microfluidics is typically achieved through conventional microvalves, which tend to be miniaturized versions of their macroscale counterparts. They are generally actuated through contact between a micromachined orifice and a flexible membrane [7]. Thermal [8,9] piezoelectric [10,11] or electromagnetic [12] actuation deforms the membrane, which makes contact with the valve seat to close the channel. Such microvalves are difficult to fabricate, suffer from unavoidable flow leakage due to the presence of moving elements, and the small gap between the sealing element and the valve seat can generate excessive flow resistance [13].

Considerable effort has been directed at developing innovative microvalves that actuate using intelligent materials like elastomers [14], hydrogels [15], sol-gels [16], or phase-change materials like paraffins [17,18] and ice [7,19–23]. These alternative microvalving approaches introduce other challenges while benefiting from operation with no moving parts. For instance, all the microvalves, except the hydrogel and the ice-based phase change valves, require an external sensor for timing the valve closure. In some hydrogel and paraffin valves, the phase change material is in direct contact with the working fluid, raising contamination and biocompatibility concerns [22]. In addition, accurate positioning of the molten paraffin at the desired location, as required for proper sealing, is difficult [18]. Moreover, once the paraffin solidifies and plugs the channel, an external pressure is required to re-open the valve, thus making it more suitable for a ‘one-shot’ operation. In contrast, ice valves utilize the working fluid (aqueous solution) itself as the phase change material to shut off the flow; they are non-invasive and leak-proof, have no moving parts and no dead volume, are free from foreign material, and offer no extra flow resistance in the default

open state. As a result, ice valves have been explored for applications ranging from lab-on-a-chip devices where the rate of reaction can be controlled by freezing the flow of reactants [7,22] to complex microfluidic systems involving separating and routing fluids [24] by freezing small water droplets that are immiscible with fluids.

Another key feature of ice valves is that they can withstand very high-pressures (e.g., 413 MPa [25]), without any deformation or leakage, thus, making them suitable for high-pressure applications, like high- and ultra-high performance liquid chromatography (HPLC and UHPLC), sampling under extreme conditions, and in microreactors. In these applications, pressures can exceed 100 MPa, making flow control using conventional microvalves difficult to implement and expensive. Ice valves can be used in these applications as injection, check, purge or switching valves. They also provide contamination-free and no-pressure-loss valving as they do not have any moving parts or external components in the flow path; their zero-dead-volume makes them especially beneficial for UHPLC applications which are sensitive to gradient mixing.

However, a drawback of ice valves is that they have long response times, on the order of seconds (~2.5–30 s [19–22]) compared to a few milliseconds (as low as 1 ms [26]) for conventional microvalves. This long response time is a result of the limited cooling capacity of the cooling mechanisms employed and the inherent need of supercooling for the ice to nucleate. While a number of the existing studies have focused on modifying the device design or the cooling method [20,23,27] to reduce the response time of ice valves, the current methods are less than ideal and unsuitable for easy integration in complex multi-channel microfluidics, owing to their high thermal mass and large footprint (e.g., thermoelectric coolers [7,20–23]), expensive and complex fabrication (e.g., on-chip Peltier coolers [28,29]), or difficulty controlling the location and the size of ice valve formation for microfluidic applications (cryogenic refrigerants [19,30]).

While most prior studies have focused on design modifications at the device scale or changes in operating conditions, the ice formation and growth process occurring within the channel flow remains relatively unexplored. Once nucleation occurs, water-to-ice conversion takes a finite amount of time [31], which may constitute a considerable duration of the valve response time, depending on the mode of ice formation. It is essential to develop an understanding of the factors

that govern the flow freezing process in small channels, commonly encountered in microfluidic ice valve applications, in order to reduce and control the response time of ice valves, and to design a suitable ice valve cooling method for use on a complex microfluidic device for high-pressure operations.

## 1.2 Objectives and Major Contributions

The main objectives of the present work are to: (1) delineate and characterize the different ice formation modes occurring during the freezing process in water flowing in a small channel using high-speed visualization; (2) understand the effect of water flow rate on the channel closing time; (3) develop a simple finite-element-based model to determine the factors that affect the annular ice growth rate and channel closing time; (4) understand the effect of channel diameter on the channel closing time; (5) design and demonstrate an ice-valve formation method and characterize the response time of the ice valve; and (6) develop a model for the chip cooling process as a means to provide guidelines for chip design where ice valve can be used. This dissertation focuses on obtaining a complete understanding of the fundamental flow freezing process occurring inside small cooled channels as a step toward arriving at techniques to efficiently form an ice valve for microfluidic applications.

An experimental setup is designed to study the ice formation process in water flowing through small microchannels, using liquid $N_2$ as the coolant. Two qualitatively different ice modes formed during the freezing process in a glass microchannel (ID = 500 $\mu$m) are observed using high-speed visualization: dendritic and annular. These modes are characterized based on the time history of the external channel wall temperature and the water flow rate, both synchronized with the visualization images. The effect of flow rate (0.5 ml/min, 1.0 ml/min, and 1.5 ml/min) on the ice formation behavior and the channel closing time is studied and the results are presented.

A simple model is developed to understand the effect of flow rate and channel wall temperature on closing time of the annular ice growth responsible for channel closure. Model-predicted annular closing time varies inversely with the temperature difference driving the latent heat ($T_i - T_{wall,ext}$) (which is indirectly controlled by the water flow rate), and directly with both the square of the channel diameter and the effective thermal resistance to radial heat flow.

Further, the effect of channel diameter on the ice formation modes and the channel closing time is studied. The freezing process is investigated using high-speed visualization synchronized with the external channel wall temperature data for three channel diameters ($D$ = 100 $\mu$m, 300 $\mu$m, and 500 $\mu$m, respectively) at a constant-pressure-driven water flow rate (0.3 ml/min) and the results are presented.

Lastly, a liquid $CO_2$ based ice-valve cooler, which is compact enough to be interfaced with complex, multi-channel microfluidic devices and can precisely control the location of cold-spot for ice valve formation, is designed and demonstrated. The cooler is designed to self-limit the flow of cryogen, reducing the wastage. The effect of flow rate (10 µl/min – 40 µl/min), channel size ($x_{channel}$ = 50 $\mu$m,100 $\mu$m, and 200 $\mu$m) and chip metrical (PMMA and Glass) on the response time of the ice valve is studied using high-speed visualization. The pressure tolerance of the ice valve is reported. Finally, 3-D numerical and 1-D analytical models are developed to evaluate the cooling process of the chip in contact with this cooler, with the purpose of developing chip design guidelines.

### 1.3 Organization of the Document

The document is organized into five chapters. CHAPTER 1 contains background information regarding the flow freezing process in small channels and presents the objectives and major contributions of this work. CHAPTER 2 reviews relevant literature regarding the experimental and modeling studies on freezing process in large channels, the modeling studies on freezing in small channels, the existing ice valve technologies and the high-pressure microfluidics. CHAPTER 3 describes the ice formation modes formed during flow freezing in a small channel and their characterization, the effect of flow rate on the closing time of the channel and development of a simple finite-element based model to predict the annular ice formation rate and channel closing time. CHAPTER 4 describes the effect of channel diameter on the closing time of the channel. CHAPTER 5 is focused on designing and demonstrating a stand-alone and simple ice valve formation technique and characterizing the valve response time as well as developing chip design guidelines for use with the cooling mechanism. CHAPTER 6 presents a summary of the work done in this dissertation and proposes future research direction.

# CHAPTER 2. LITERATURE REVIEW

## 2.1 Freezing in Large Channels

Several studies [32–44] have explored the different ice formation modes and the thermophysical parameters affecting their growth behavior in supercooled, large-diameter channels under different flow configurations, including stagnant liquid, flow entering an empty channel, and continuous flow through the channel.

The temperature history during the freezing of pure water in a cylindrical channel is introduced in Figure 2.1 for the canonical case of stagnant conditions [32]. The channel is initially placed into a cold isothermal environment well below the equilibrium freezing point. When the water is cooled, it does not necessarily freeze at the saturation freezing point ($T_f$ = 0°C at atmospheric pressure), but must be cooled by several degrees below $T_f$ before nucleation occurs [33], *i.e.*, the nucleation temperature $T_n < T_f$. For example, the nucleation temperature for normal tap water is 4–6°C below the freezing point [34]. Water existing in liquid phase below the equilibrium freezing point is in a thermodynamically metastable state and is classically termed as undercooled or supercooled water, with the degree of supercooling given by $(T_n - T_f)$. For microchannel closure, the phenomenon of supercooling is important in two ways. First, the time required to achieve supercooling can be long. For example, in a microchannel (233 $\mu$m×172 $\mu$m×38.2 $\mu$m) water had to be supercooled to –17°C before the initiation of nucleation, which required a time of ~3–8 s [22]. Second, in supercooled water, ice does not grow as a solid layer, but rather as dendrites which can have a markedly faster growth rate and hence affect the channel closing time. As shown in Figure 2.1, once nucleation occurs, ice dendrites form within the channel cross-section and a large amount of latent heat is released (at a faster rate than can be removed from the system). This causes the water temperature to increase rapidly to the equilibrium freezing point. Subsequently, the water-to-ice phase change occurs at this constant temperature in the form of a solid ice annulus at the channel circumference, which grows radially inward. Once the channel cross-section is filled, the ice loses sensible heat and its temperature begins to decrease.

The freezing of water *entering* an empty pipe was investigated by Gilpin [38], who observed that as water filled an empty supercooled pipe of 10 mm diameter, ice could form and cause pipe blockage through one of the three modes: dendritic, annular, or a dendritic-annular mixed mode. A criterion to determine which mode of formation occurs was proposed based on the wall temperature, the wall material, and the nucleation temperature. Dendritic closure was found to be more probable for pipe wall temperatures close to the freezing point and for lower flow rates, while annular ice appeared at higher wall supercooling and at higher flow rates. Inaba *et al.* [39] extended the work of Ref. [38] to experimentally study the effects of water supercooling temperature on the modes of ice formation during *flow* freezing (*i.e.*, freezing during continuous water flow) in a pipe ($D$ = 15 mm). Again, the dendritic mode was observed at lower degrees of supercooling (*i.e.*, higher absolute temperatures); the radial rate of growth of the dendritic ice front was also significantly higher than that of the annular ice.

Systematic studies on *flow* freezing are limited to channels undergoing flow blockage due to formation of annular ice. In particular, these studies investigated the effect of operating conditions such as the channel wall temperature, liquid supercooling, and the liquid flow rate on the growth rate and heat transfer characteristics of annular ice formation. An early attempt to predict the conditions under which the channel freezes shut was made by DesRuisseaux and Zerkle [41]. Assuming a constant-pressure-driven steady laminar flow in a channel with a parabolic liquid velocity profile and uniform wall temperature, they predicted that the minimum pressure-drop needed across the channel to prevent closure for a given liquid increased on decreasing liquid inlet and wall temperatures; their experimental results were in reasonable agreement with the theory. Various studies that have developed analytical models to predict the flow blockage by freezing have found that it depends on the liquid inlet temperature, flow rate, the subcooled channel wall temperature, and the channel size [42–44]; these dependencies have been experimentally verified in Refs. [42] and [43].

### 2.2 Freezing in Small Channels

Only a few studies in the literature have modeled flow freezing in *small* channels, each with specific and highly restrictive assumptions. For example, in developing the model for flow freezing, some studies [7,22] neglected the ice formation completely and assumed that the channel

closure occurs instantaneously when water is supercooled to a specified temperature below equilibrium freezing point. Myers and Low [45] developed a 2-D mathematical model for predicting the annular ice growth in rectangular and circular microchannels, using lubrication theory assumption for a long and thin channel geometry. Their model calculated the ice front growth in a pressure-driven flow by taking both the conduction and the convection energy terms into account and predicted that, for the flow rates smaller than a certain value, the annular front growth and the channel closing time is driven purely by the radial conduction of latent heat. Hence, their expression for model-predicted closing time showed a functional dependence on the driving temperature and the hydraulic diameter similar to that reported in CHAPTER 3, for the range of flow rates studied. These studies indicate that the channel closing time may be reduced by one of the two methods, i.e., either by increasing the temperature difference driving the radial conduction or by reducing the channel diameter. From a practical viewpoint, the latter is a simple and cost-effective approach compared to the former, since it eliminates the need of a complex device design or a high-thermal-inertia multistage cooling system to achieve fast closure which may otherwise be required to generate the high degree of supercooling (high temperature difference: $T_i - T_{wall,ext}$).

In summary, while flow freezing has been explored in *large* channels and pipes (although closure has often been predicted using highly simplified models), no studies have characterized the differing ice formation modes that may occur during flow freezing in *small* channels suitable for microfluidic ice valve applications. High-speed visualization and characterization of the flow freezing phenomenon in such small channels can assist in understanding the factors affecting the modes of ice formation and the flow blockage time.

## 2.3 Ice Valves in Microfluidics

Valves are vital components for the proper functioning of a microfluidic device. An ideal microvalve should be easy to fabricate, cost-efficient, integrable with the complex functionalities of a microchip, multi-use, contamination- and leak free, reliable and reusable. Because ice valves function by simply freezing the operating reagent itself to stop the flow, they satisfy most of these requirements. However, they suffer from an inherent drawback of long response times, as mentioned in CHAPTER 1. The long response time is principally due to: (1) the high thermal

inertia and limited cooling capacity of the refrigeration systems used to cool the liquid, and (2) the need to supercool the working fluid to temperatures below the freezing point to trigger phase change. While an ice valve is simple to operate, the bottleneck in its design process is the cooling mechanism itself. Unsurprisingly, multiple efforts have been made to address the aforementioned issues and to design ice valves with fast response time and integrability with the microfluidic devices, as reviewed below.

The two common cooling methods used for ice valve formation are thermoelectric coolers (TECs) and cryogenic refrigerants. TECs are easy to operate using electricity; the set temperature can be simply controlled by controlling the power supplied to the device and they be used for both freezing and thawing the valve. TECs were first used in ice valve applications by He *et al.* [21] to freeze the buffer solution in a fused silica capillary to form ice valve in a micro-PCR device, which was capable of closing the capillary in approximately 2 min. The method was then implemented on-chip by Gui and Liu [7]. They used a single-stage TEC and welded it to a stainless-steel channel (OD 0.4 mm and wall thickness 0.1 mm) to ensure proper thermal contact. The closing time, as observed by tracing the motion an air bubble upstream of the channel, was measured as 16 s. To speed up the cooling process, Chen *et al.* [22] lowered the initial temperature of the system by pre-cooling the fluid/device upstream of a TEC and obtained a closing time of 5.6 s. Gui *et al.* [20] used a two-stage TEC to further decrease the closing time to 2.72 s; one stage reduced the device temperature close to 0 ℃ and the other provided the subcooling. Si *et al.* [23] employed a movable four-stage TEC unit to generate a large temperature difference between the cooling surface and the channel (TEC surface temperature = -42.5 ℃); they also embedded a conductive aluminum metal piece into the channel which enhanced the heat conduction. The closing time for a 300 $\mu$m × 100 $\mu$m at a flow rate of 10 $\mu$l/min was 0.37 s, which is also the shortest reported closing time for an ice valve.

While using TECs has its advantages, they do have very high thermal mass, making them unsuitable for quick operation. Additionally, multi-stage TECs have an extremely large footprint compared to the size of the valve itself, making them unsuitable for integration in complex microfluidic devices, not to mention the large amount of power they consume for operation. To reduce the response time, Dourdeville [46] proposed a design which used microchannel in a small

metallic housing, which could be moved between a TEC and a heating unit in placed parallel to it, allowing it to cool down and heat up quickly due to low thermal mass. Efforts were made to improve the integrability of the TEC with the chip [28,29,47]. Neumann *et al.* [47] used a single TEC integrated with a chip and demonstrated 588 normally closed valves, which could be opened individually using 588 individual on-chip ohmic resisters with small thermal mass. Integrability could also be increased by using on-chip Peltier junctions [28,29], which reduce the thermal mass of the system and can generate a much smaller local cold spot compared to on-shelf TECs for faster operation; response times of 55 ms and 40−100 ms were obtained by Refs. [28] and [29], respectively. These times are much faster than large commercially available TEC but these platforms require sophisticated designs which increase the complexity of chip-to-world interface and add to the cost of fabrication [27].

Cryogenic refrigerants were used to create the first ice valves to control the flow of reagents in capillaries in for liquid chromatography applications. Bevan and Mutton [19] used a mixture of liquid-gas $CO_2$ to freeze the flowing medium in a thick-walled capillary (50 $\mu$m ID and 375 $\mu$m OD). Tan and Yeung [48] later used liquid nitrogen to freeze the capillary. Cold cryogens caused rapid freezing because of low thermal mass of the capillary. The method was simple and required no precision engineering; the control was non-invasive and resulted in zero dead-volume valves. The method, however, used excessive amount of cryogen. Gerhardt *et al.* [49] possess a patent for a design for a cooling mechanism which self-limits the cryogen use for ice valve formation in capillaries; an expansion chamber was fitted with an expansion nozzle and a porous hole. The cryogen entered the expansion chamber through the expansion nozzle and the hole and rapidly cooled down the capillaries passing through the chamber until freezing occurred. As the temperature of the chamber reduced, the cryogen expanded in the chamber and solidified, occluding the porous holes and stopping the cryogen flow. However, no experimental study was performed to analyze the performance of this device. Furthermore, the proposed mechanism was designed for macroscale components with individual capillaries running through the chamber, making it unsuitable for use microfluidic devices. Additionally, such low temperature liquids and macro-scale cooling mechanisms are hard to integrate at microscale with the existing design, and have some inherent concerns regarding safety, unwarranted frost formation, and very long thawing times. However, cryogenic refrigerants have multiple advantages over TECs in that they are

relatively inexpensive, have smaller footprint, and offer flexibility and simplicity in the designing. They have very low thermal mass, which makes the thermal manipulation of the valve relatively much quicker. Additionally, with a suitable cooler design, they can be used to control the location and size of ice valve and can be integrated with complex microfluidic devices.

Another method to reduce the response time of the ice valves is by reducing the amount of supercooling required for nucleation. As discussed in Section 2.1, liquid water does not necessarily freeze at its equilibrium freezing temperature (0 ℃). Water can continue to exist as liquid at a supercooled temperature in a metastable state, until it reaches a nucleation temperature at which the ice nuclei attain a critical radius and precipitate. In the flow channels, nucleation can also occur heterogeneously at the walls, where the surface roughness provides nucleation sites. But, since the microfluidic devices have low surface roughness, the supercooling requirement can be high. This requires usage of multi-stage TEC devices since each stage has a limited temperature range, making it difficult to integrate in high-complexity chip. To reduce the supercooling requirements, the fluid can be speckled with ice nucleating agents (INA), which trigger ice nucleation at warmer temperatures. Gaiteri *et al.* [27] and Ramsey *et al.* [50] demonstrated the use of ice-nucleating proteins (INPs), extracted from the P. Syringae bacteria, in combination with TEC to nucleate ice at temperatures as warm as -2 ℃. They observed that the closing time reduces to half on the presence of the INPs for a TEC operating temperature of -45 ℃ and to a fourth at TEC operating temperature of -20 ℃ due to reduction in required supercooling. While the nucleating agents reduce the power and heat pumping requirements, they also introduce external particles to the flow which raises contamination concerns. Each INA requires very specific working fluids and conditions to function in desired manner. Moreover, some of these agents can inhibit the biological processes or cause precipitation of the salts in biological buffers [50].

## 2.4 Valves for High-Pressure Microfluidics

Although most microfluidic chips are designed to function at moderate pressures, high pressure is utilized for certain microfluidic applications like chromatography, microreactors, and microextraction, where the high pressure improves quality of the process and is even imperative for functioning. As is true for microfluidics in general, high-pressure microfluidics rely on the reliable and leak-proof flow control mechanism for seamless operation, but high-performance

liquid chromatography (HPLC) and ultra-high-performance liquid chromatography (UHPLC) are the most impacted applications because of their high pervasiveness in the chemical and biological analysis systems. Since the pressures used in HPLC and UHPLC can go as high as 40 MPs and 100 MPa [51], respectively, it is crucial that these valves can operate at high pressures without leakage. Moreover, since the efficiency of the UHPLC process is highly subjective to the quality of the gradient between the reagents and the solvents upstream of the column, it is desirable to have zero dead-volume valves which do not promote gradient mixing in the flow path. Thus, in addition to having the characteristics of ideal valves for low-pressure microfluidics enlisted in the previous section, the HPLC valves are also required to have zero dead-volume and high-pressure operation. Ice valves have demonstrated the capacity to operate leak-free even at high pressures [22,25], and have zero-dead volume, but their successful commercialization is hindered due to the absence of a suitable control mechanism to form them.

Most commercial column-based HPLC systems use a multi-port valve for routing the flow in the system; they are most commonly used as injection valves but can also be used as switching valves between multiple columns and multiple dimensions [52]. An injection valve allows for the entry of the low-pressure sample into the high-pressure solvent flow path without interrupting the flow or causing pressure fluctuations. It can deliver variable volumes into the column at 0.2% error and can sustain pressures as high as 48.3 MPa. While they increase the repeatability of the results by automating the process and reducing the number of connections which could leak, they have a few major problems [53]. They are large and expensive; they have a complex design which consists of a stator, a rotor, loops and connections to other LC components. The stator is a stationary metallic component which has inlet and outlet ports for fluids, while the rotor is usually a plastic component with the paths to connect various stator ports and is connected to motor drive. The rotor and the stator need to be aligned and tightly sealed against each other perfectly to avoid leaks, which is done with the help of set and holding screws; this adds to the error and complexity of the design. Continuous operation of valve introduces scratches on this seal, which causes leaks and cross flow of the components. The seal between the rotor and the motor shaft wears out over time, causing leaking. The material of rotor is dependent on the pH value of the solvent; the sample gets absorbed by the seal, affecting the results. Additionally, the flow through multiple components over time causes contamination of the reagents and blockage in the flow path.

With the advancement of microfabrication technology, the entire column-based HPLC system can now be made on a single chip. Chip-LC has some obvious advantages over column-based LC; with the preprocessing of solvents to analysis happening on a single chip, they are fast, easier to operate [51,54–57], less prone to leakage, and are relatively cheaper than commercial systems (3k-4k USD vs 30k-40k USD [58]). Chip-LC uses very small volume of expensive reagents and generates low waste. Since there are no manual steps involves, it increases the repeatability and accuracy of the results, while making the process safer. Chip-LC introduces flexibility in the process and chip design, which are easier to fabricate on any suitable substrate [54]. Furthermore, the small size and low-cost of chip-LC makes it desirable for remote field and point-of-care applications [58]. All these factors have made chip-LC the standard of operation in analysis of biomolecules. Unsurprisingly, the greatest obstruction in the successful implementation of chip-based LC is the 'plumbing', where all the fluidic components need to be assembled with high-pressure tolerant, leak-proof, and zero dead-volume fittings to ensure maximum efficiency. Multiple studies have been done in the field to design a valve for high-pressure microfluidics, specifically for chip-LC, but each has its own drawbacks.

PDMS membrane-based mechanical microvalves for low-pressure microfluidics (< 1 MPa) provide great sealing and are easy to integrate into complex chip designs. However, they have shown to not hold pressure greater than 1 MPa [59], hence making them unsuitable for high-pressure applications. Hasselbrink *et al.* [60] developed an in-situ, movable micro-piston by selectively exposing a photo-sensitive, non-stick polymer formulation to a laser in a microchannel on the micro-chip. Multiple pistons could be used to selectively block the sample or the solvent path to the separation column, making an injection valve. The piston sealed against pressures greater than 30 MPa, with a leakage rate of 200 pl/s, and had an actuation time of 33 ms. Moreover, the polymer could shrink or swell by reacting with the reagent, thus affecting the results. Kirby and coworkers [59,61,62] improved the polymer to reduce swelling, and changed the design to create bi-directional pistons, with a reduced leakage rate of 0.2 pl/s at pressures as high as 7 MPa. However, these valves did not stop the flow completely and required very complex and precise fabrication process. Furthermore, the polymer could contaminate the reagents by leaching into them.

Hjort and coworkers [63,64] designed an active membrane valve that were actuated by paraffin. The valve consisted of a parylene-coated stainless-steel membrane with a channel cavity on one side and a paraffin wax reservoir on the other. The expansion of paraffin wax on melting pushed the membrane into the channel cavity which then blocked the flow path. In addition to holding high pressures up to 20 MPa, these valves had an actuation time of less than 1 s. Also, unlike their low-pressure counterparts, these valves avoided direct contact of paraffin with the reagents, reducing the contamination and increasing fluid compatibility. However, the multi-layer fabrication process for the membrane and valve increases the complexity and reduces the structural strength, especially at high pressures.

Luo *et al*. [14] demonstrated non-mechanical hydrogel valves made of temperature sensitive polymers, which could swell up at approximately 30 C to stop the flow and could hold pressures up to 18 MPa without noticeable dislocation, structural damage or leakage. The actuation times varies between 1-4 s depending on the type of polymer used. The positioning of hydrogel valve in the channel is, however, challenging; they have relatively long actuation times, in-situ fabrication adds complexity to the design, and only few hydrogels are compatible with organic solvents, making contamination a possible problem.

Yin *et al*. [56] and Yin and Killeen [57] designed a microscale counterpart of the macroscale multiport rotary valve for use in a nano-volume on-chip analytical system, which is commercially used as the Agilent HPLC-Chip. The chip consisted of an enrichment column, a chromatography column and an MS spray nozzle for analysis on a single platform, which reduced the need for fittings and connectors, thus, reducing the leakage and increasing the reliability of the system. The chip has ports for inlet and outlet for process fluids and the on-chip rotary valve acted as the link between those ports. The valve rotation can be controlled by placing the chip between a rotor and a stator, which requires that the chip be used with the macro HPLC system for functioning; the macro HPLC system also provides the pumping mechanism. The rotating part also functions as an enrichment column to concentrate the sample volume before pushing it into the LC column. While the chip has excellent performance compared to other state -of-art on-chip LC devices, the valving process involves precision engineering and complex fabrication process, and causes chip

wear and tear due to rotation, thus, needing replacement every few runs. Moreover, it is expensive and cannot function as a stand-alone chip without the macro-HPLC system.

Since the UHPLC systems operate at pressures in excess of 100 MPa where most commercial HPLC valves fail to operate properly, needle valves are used as check valves to prevent damage to the UHP pump while pressure amplifier generates the flow in the gradient loop. Thus, they undergo extreme pressure cycling during the process, which often results in failure [25,65]. Pinto *et al.* [65] used a Peltier stage while Moore [25] used a self-limiting cryogen cooling mechanism to freeze process fluids when the needle valves failed. But, as mentioned earlier, each method has its own drawbacks. Since the ice valves can withstand very high pressures, they could be used in commercial, macroscale UHPLC system in addition to the mechanical needle valves as a fail-safe mechanism.

In summary, the present valving mechanisms for micro and macro high-pressure fluidics run short of providing the ideal valving method; they lack the needed sophistication and control, that makes them unsuitable for integrated on-chip operation in complex microfluidic devices. Ice valves can control the flow without invading the flow path, and do not require precision engineering of the chip, they are free from contamination, and leakage. They satisfy almost all the requirements of an ideal valve but the present methods to form ice valve lack the needed sophistication and control, especially for the use in on-chip microfluidics.

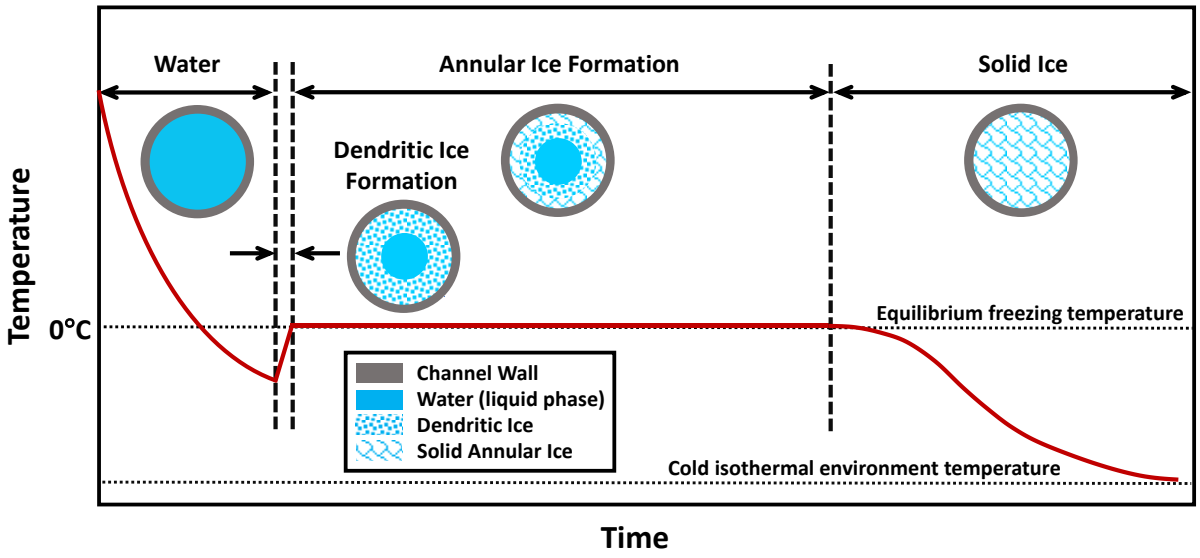


Figure 2.1. Schematic representation of the time evolution of water temperature and the corresponding ice formation modes during the freezing of *stagnant* water in a cooled cylindrical channel.

# CHAPTER 3. ICE FORMATION MODES DURING FLOW FREEZING IN A SMALL CYLINDRICAL CHANNEL

In this chapter, an experimental facility is developed and demonstrated to control the external cooling boundary conditions during visualization of the ice formation modes in a small channel (500 $\mu$m inner diameter). Flow visualizations are synchronized with measurements of the wall temperature and flow rate to analyze the freezing process for three *constant-pressure-driven* flow rates (0.5 ml/min, 1.0 ml/min and 2.0 ml/min). The different modes of ice formation observed during the freezing process are delineated and characterized. Additionally, a simplified volume-discretization-based model is developed to determine the factors that influence the annular ice growth. The model uses simple energy balances and a scaling analysis to predict the annular growth duration as a function of flow rate. The nomenclature for this chapter is presented after the chapter text, before the figures. The material presented in this chapter was published in the *International Journal of Heat and Mass Transfer* [66].

## 3.1 Experimental Setup and Procedures

### 3.1.1 Test Facility

The experimental facility consists of a pressure-driven open water flow loop and an open nitrogen ($N_2$) flow loop that are connected to a test cell (Figure 3.1). Water flows through a microchannel in the test cell while the cold $N_2$ gas flows over the outer channel surface to lower its temperature and initiate freezing of the water; the freezing process is captured by a high-speed camera. The entire experimental facility (except the cryogenic cylinder) is mounted on a vibration-isolated optical table (VH3648W-OPT, Newport).

The water flow is driven by the pressure difference between a pressurized reservoir and the ambient. This constant pressure-drop driven open flow loop allows water to enter the channel at precisely controlled, constant flow rates. The reservoir is pressurized with a compressed air source and the desired pressure is maintained using a high-precision servo-controlled pressure regulator (PRG200-25, Omega; ±0.031 kPa). The water pressure, $P_{water}$, is measured downstream of the reservoir using a pressure transducer (PX302-015GV, Omega; ±0.26 kPa). The water volumetric

flow rate is measured using a liquid flow meter (LC-5CCM-D, Alicat; ±0.1 ml/min). The corresponding mass flow rate is determined from the liquid density corresponding to the liquid temperature recorded at the channel inlet. The water flowing out of the test cell is collected in an open reservoir at ambient pressure.

In the nitrogen open-loop system, a constant-pressure cryogenic cylinder is used to deliver $N_2$ to the flow loop. To control the cylinder pressure, a pressure relief valve is used to vent $N_2$ that evaporates continuously inside the cylinder; a pressure gauge measures the cylinder pressure. The nitrogen flow rate is controlled using a ball valve mounted on the cylinder outlet. Downstream of the cylinder, the $N_2$ flows through an insulated (Cryogel-Z, Aspen) section of pipeline to a T-junction which divides the $N_2$ flow into two separate flow paths, each with an independently adjustable flow control valve. One path routes to the test cell and is regulated by the $N_2$ inlet valve; the other path vents to ambient through a vent valve (see Figure 3.1). As the nitrogen flows along the line to the test cell, it boils continuously due to the external heating of the line. This generates a large back pressure that can stall the nitrogen flow out of the cylinder. The venting valve is used to vent out some portion of the $N_2$ to allow for a continuous flow of $N_2$ out of the cylinder. A T-type thermocouple (TJ36-CPIN-116G-12, Omega; ±1.0°C) is installed downstream of the cryogenic cylinder and upstream of the T-junction to measure the $N_2$ temperature.

The temperature of the $N_2$ gas flowing into the test cell is controlled by a wire heater wrapped around the copper tubing just upstream of the test cell (see Figure 3.1). The electrical power to the heater is supplied by an adjustable direct current (DC) power supply (Sorensen, DCS40-25E). The nitrogen leaving the test cell is heated to the ambient temperature using a copper-finned heat exchanger and the flow rate is measured using a 1–5 L/min microturbine gas flow sensor (Cole Parmer, FF-00368-KV; ±0.2 L/min) before it vents to the ambient.

The test cell (Figure 3.2) is a custom component that is 3-D printed using a transparent photo curable material (VeroClear Fullcure810, Objet). The test cell consists of a hollow disk-shaped cavity (12 mm tall and 25 mm in diameter) with various ports for interfacing with the water flow, nitrogen flow, and measurement probes. The cavity is sealed shut with a 3.6 mm-thick transparent polycarbonate cover to enable visualization. The entire test cell sits inside a circular aluminum

enclosure (not shown in Figure 3.2), which prevents frost formation on the cell and has glass viewing windows on the top and bottom to permit visualization.

A borosilicate glass channel (Vitrocom, CV5070) of circular cross-section with a nominal inner diameter ($D$) of 500 $\mu$m and a wall thickness ($R_{wall,ext} - R_{wall,int}$) of 100 $\mu$m is mounted horizontally between two diagonally opposite inner ports in the cavity, as shown in Figure 3.2. The non-dimensional channel length exposed to the inside of the cavity $l/D$ is 40. The channel is sealed into the cell at both ends using miniature compression fittings and transparent adhesive silicone epoxy (Momentive, RTV118). The cavity also has two diagonally opposite inlet and outlet nitrogen ports for flow of the cold nitrogen gas over the channel. A perforated diffuser plate is placed in front of the $N_2$ inlet port to prevent direct impingement of the incoming cold $N_2$ gas on to the channel and to achieve uniform temperature surroundings inside the cavity. The nitrogen inlet temperature ($T_{N_2,in}$) is measured using a T-type thermocouple (5TC-TT-T-36-36, Omega; ±1.0°C) placed in front of the diffuser plate while the cavity temperature ($T_{cav}$) is measured using a RTD (WZP-100-1/16, Sifang; ±0.1°C) located close to the cavity center, approximately mid-way along the channel length. Both the thermocouple and the RTD are placed in the same horizontal plane as the channel. The channel external wall temperature is measured using two T-type thermocouples (5TC-TT-T-40-36, Omega; ±1.0°C) located at each end of the channel. The beads of the wall thermocouple junctions are attached to the channel by carefully placing the bead in contact with the channel wall and wrapping the unsheathed length of the wire (0.6 mm) around the channel. Subsequently, the channel is inspected under a microscope to ensure that there is proper contact between the bead and the wall as well as no other unwanted contacts between the unsheathed wires, except at the junction. Finally, the thermocouples are secured in place by using a thermally conductive epoxy (Duralco 120, Cotronics).

There are two port hubs in the test cell, one at the water inlet side and other on the water outlet side. Each hub contains three ports for the flow paths, water temperature measurements, and rod heater (only used at outlet hub). All the port connections are sealed using miniature compression fittings and epoxy (RTV118, Momentive/GE) to prevent water leakage.

As water flows through the externally cooled channel and its temperature decreases in the streamwise direction, freezing may initiate in the channel after it has entered into the outlet hub region, where the water temperature is lowest and where the freezing process cannot be visualized. To ensure that water is only cooled along the channel length that is exposed to the cavity (*i.e.*, the visible length), a custom 1/16" (1.59 mm) heater rod, powered using an adjustable DC power supply (XG 100-8.5, Sorenson), was inserted into the outlet hub port. This rod heater warms the outlet hub region, which ensures that the water temperature is lowest in the field-of-view (Figure 3.2). It has been experimentally verified that the heating of the outlet hub does not affect the trends in external wall temperature and the channel closing time.

The external wall temperature measurements are recorded at a sampling frequency of 39 Hz using a 20-port data acquisition unit (NetDAQ 2640A, Fluke) with a NetDAQ interface. All other sensor data are recorded at a frequency of 0.22 Hz using another data acquisition unit (34970A, Agilent) with a 20-channel multiplex module using a LabVIEW interface. The power supplied to the heaters is calculated by measuring the voltage drop across them and the current flow across their respective shunt resistors (HA 5 100, Empro).

### 3.1.2 Test Procedure

To begin a test, the water line is first completely dried by flushing with dry compressed air for ~30 min. Then the compressed air supply to the reservoir is turned on and the water flow rate is set to 5 ml/min (maximum measurement limit of the flow meter). The reservoir air pressure is then gradually reduced manually using the pressure regulator till the water flow rate decreases to a flow rate that is 0.5 ml/min higher than the desired flow rate.

The cryogenic cylinder pressure is set to a constant value of 77.6 kPa using the pressure control valve mounted on the cylinder. The $N_2$ flow is then initiated by first opening the $N_2$ inlet valve completely and then cracking open the vent valve to establish a continuous $N_2$ supply to the test cell at a constant flow rate of 2.00 L/min. Subsequently, the power to the $N_2$ heater is turned on and adjusted such that the cavity temperature reaches $T_{cav}$ = 10°C (with a standard deviation of ±2°C over all test runs). The water does not freeze in the channel during the process of setting the cavity temperature due to the elevated initial water flow rate mentioned above. Once the cavity

temperature has reached a steady-state condition (standard deviation in $T_{cav}$ over 10 min is less than 1°C), the compressed-air pressure to the reservoir is controlled to reduce the water flow rate to the desired set point. The corresponding constant water pressure ($P_{water}$) upstream of the test section (downstream of the reservoir) is recorded. It is noted that while the water is driven through the channel by this constant upstream pressure condition throughout the test, the flow rate only remains constant at the set-point until freezing initiates (an increase in the flow resistance of the channel after freezing causes a reduction in the flow rate).

Next, the power to the $N_2$ gas heater is reduced in a step-wise manner to reduce the cavity temperature and undercool the water until ice is observed to nucleate in the channel. The power steps are chosen such that the cavity temperature reduces by ~4–5°C at each step. At each power level, the system is allowed to attain a steady-state condition where the standard deviations in both $T_{cav}$ and $T_{wall,ext}$ reduce to less than 1°C and the temperature difference between them becomes constant. The outlet hub temperature is kept above freezing by powering the rod heater, for example, to a value of 1.5±0.5 W when $T_{cav}$ reaches to about –8°C.

This test procedure is repeated in a similar manner for multiple trials of each test case. The water flow rates, water pressures, and cavity temperatures at freezing corresponding to the three test cases A, B, and C, averaged over 8 trials for each case, are listed in Table 3.1.

The temporal variation of external channel wall temperature recorded at the channel inlet and the outlet is highly repeatable, with the inlet temperature data matching the outlet but shifted in time (see APPENDIX A.1). This is because the inlet thermocouple has a delayed registration of the temperature jump that occurs after ice nucleation. This delay corresponds approximately to the time taken by the initial dendritic ice to traverse the entire channel length (from outlet to inlet) following nucleation near the outlet. However, because the thermocouple bead at the outlet obstructs visualization, it was removed for the trials for which synchronous visualization was conducted, and only inlet temperature data are shown.

To ensure that the heating of the outlet hub has no influence on the freezing process, other than shifting the location of nucleation to be within the field of view upstream of the outlet, a separate

set of experiments were carried out (keeping the same inlet and boundary conditions) with the rod heater removed. Results from these experiments confirm that the trends in the variation of $T_{wall,ext}$ and the channel closing time remain the same with and without the heater.

### 3.1.3 Visualization

Ice formation modes during freezing of water flowing through the channel are visualized using a high-speed camera (VEO 710L, Phantom) fitted with a long-working-distance high-magnification zoom lens (VHZ50L, Keyence). For accurate positioning, the camera and the lens assembly is mounted on a three-axis traversing stage. This assembly was placed vertically above the optical window of the test cell enclosure, with the lens focused on the channel mid-plane in the field-of-view ($0.74 < z/l < 1$), as marked in Figure 3.2. The channel is uniformly backlit using an adjustable, high-intensity LED strip with an integrated high efficiency diffuser (BL138, Advanced Illumination).

The images are acquired at a frame rate of 5000 fps with an exposure time of 190 $\mu$s using the Phantom PCC software (version v2.8.761.0). An image size of 960×152 pixels is used to visualize the freezing process at a spatial resolution of 6 $\mu$m/pixel, which corresponds to an optical magnification of 3.3×. The camera is set in a looping mode to record continuously throughout the test. Once the freezing process is complete, an external end-trigger signal is sent to the camera using a pulse generator (Model 505-4C, Berkeley Nucleonics Corporation), which stops the recording and saves the most recent 17.38 s of recorded frames. The time history of the trigger signal is recorded by a data acquisition unit (NetDAQ 2640A, Fluke) using a NetDAQ interface at a sampling frequency of 39 Hz. This enables synchronization of the temperature and flow rate readings to the high-speed images, so that any change in these readings can be matched to corresponding visualizations of the freezing process inside the channel.

During annular ice growth, the thickness of the solid ice layer is measured using the images as it grows radially inwards from the inside channel wall. However, the actual physical position of the water-ice interface differs from its apparent position in the image due to the optical distortions caused by light refraction at the ice-glass and the glass-gas interfaces. To demonstrate the relationship between actual and apparent location of the annular ice front in the channel, the

schematic diagram in Figure 3.3(a) shows a quarter-section of the channel cross-section (*x*-*y* plane) alongside a sample image of the channel side view (*y*-*z* plane) obtained via the experimental visualizations, both aligned along the channel center-line. An accurate measurement of the annular ice thickness is obtained by accounting for these optical distortions in the images, using a refraction correction method reported by Kingston *et al.* [67], as is described in detail in APPENDIX A.2.

## 3.2 Results and Discussion

The results obtained from flow freezing of water at different flow rates are presented here. As described in Section 3.1.2, to initiate freezing, the channel external wall temperature is reduced gradually in steps. Freezing initiates suddenly at the water-wall interface at a certain point when the wall temperature is cold enough ($T_{wall,ext}$ = –6.5°C, –9°C and –12.75°C for test cases A, B and C, respectively). During the freezing process, the different modes by which ice forms are identified and their qualitative features are first discussed in Section 3.2.1 based on the visualization images. These modes are subsequently characterized based on the time history of the external channel wall temperature and the water flow rate, both synchronized with the visualization images. Finally, a simple model is developed to understand the effect of flow rate and channel wall temperature on the annular ice growth responsible for channel closure (Section 3.2.2).

### 3.2.1 Ice Formation Modes

Figure 3.4 and Figure 3.5 show selected images from the high-speed visualizations for test case A during the dendritic and annular modes of ice growth, respectively. These image sequences show the complete process of channel closure starting from dendritic ice nucleation at the channel inside surface to complete flow blockage resulting from inward growth of the annular ice. Similar behavior is observed for cases B and C. Note that air bubbles precipitated from the undegassed water during the freezing process in some tests.

In Figure 3.4, dendritic ice nucleation occurs at the water-wall interface near the channel outlet at $t$ = 0.021 s. As water flows through the channel, losing sensible heat along the streamwise direction, it is coldest at the outlet. The position of nucleation is slightly upstream of the outlet by design (as discussed previously in Section 3.1.1). Dendritic ice nucleation occurs adjacent to the

wall where the water temperature is lowest; the external wall temperature is supercooled as shown by measurements ($T_{wall,ext} = -6.5$°C), and since dendritic ice is formed only in supercooled water [35–40], we infer that the water adjacent to the internal channel wall is also supercooled. Following nucleation, the dendritic ice rapidly grows axially in both upstream and downstream directions from the nucleation point and covers the field of view ($0.74 < z/l < 1$) within $t = 0.21$ s.

Based on the current visualization, inward radial growth of the dendritic ice (*i.e.*, thickness of the dendritic ice layer) cannot be quantitatively characterized from the images. However, it can be inferred from our observations that the dendrites do not fill the entire cross-section. For the dendritic ice to grow radially inward to the center of the channel, the water should be supercooled across the channel cross-section [40]. However, the water temperature measurements at the channel outlet indicate that the bulk temperature is above the equilibrium freezing point ($T_{water,out}$ = 1.2°C), and therefore the water is not supercooled across the entire channel cross-section. In addition, if the dendritic ice filled the entire channel cross-section, it would be expected to cause a significant flow blockage; the flow rate does not reduce suddenly to zero during the period of dendritic ice growth (Figure 3.6). Furthermore, it is known from the literature [68–70] that in the presence of a surface, ice dendrites tend to grow along the surface as opposed to into the bulk supercooled water, because the higher thermal diffusivity surface (borosilicate glass in this case, compared to water) acts as a heat sink for the latent heat of fusion released during dendritic ice nucleation and growth.

The formation of dendritic ice is accompanied by a large latent heat release which leads to a rapid increase in the channel wall temperature and brings the ice-water interface temperature to the equilibrium freezing point ($T_i$ = 0°C). This is evident from Figure 3.6 which shows the time history of the external channel wall temperature and flow rate measured during the period of freezing and channel closure. Starting from an initial steady state ($T_{wall,ext}$ = –6.5°C), there is a sharp jump in the external wall temperature shortly following the dendritic ice nucleation. The short delay between nucleation and the temperature rise is due to the finite amount of time taken for the dendritic ice to traverse the channel length and reach the inlet where the temperature is measured (see APPENDIX A.1). Subsequently, $T_{wall,ext}$ continues to rise as the water adjacent to the channel inside surface converts to dendritic ice with a simultaneous release of latent heat of

fusion, until at $t \approx 1$ s when the dendritic ice front has covered the entire channel length ($0 < z/l < 1$). After this time, $T_{wall,ext}$ stabilizes at a constant value of –2°C. This dendritic ice growth period is indicated in the bar at the top in Figure 3.6. Note that the image sequence shown in Figure 3.4 corresponds to the initial 0.21 s of this period, during which only one-fourth of the channel length near the outlet ($0.74 < z/l < 1$) is covered by dendritic ice. As shown in Figure 3.5, a short time after dendritic ice covers the entire channel length, a thin layer of solid annular ice starts to appear at the channel circumference at $t$ = 1.06 s, close to the channel outlet. This solid ice annulus grows radially inwards until it fills the channel cross-section at the closure plane at time $t$ = 3.75 s.

Figure 3.6 shows that the external wall temperature is nearly constant at –2°C (with a standard deviation of ±0.5°C over all experimental runs) during the period of annular ice growth. It is reasonable to assume that the ice-water interface temperature remains constant at the equilibrium freezing temperature of $T_i = T_f$ = 0°C during the annular ice growth phase, such that the temperature difference between the external channel wall and ice-water interface is constant at $(T_i - T_{wall,ext})$ = 2±0.5°C. As the annular ice grows and becomes substantially thick such that the channel is nearing closure (at ~3.45 s in Figure 3.5 and Figure 3.6), the ice begins to lose sensible heat and the external wall temperature starts to drop.

It is evident from Figure 3.6 that there is a noticeable drop in the flow rate during dendritic ice growth, but it is still far above zero. In contrast, as the solid annulus grows and narrows the flow cross-section, there is a continuous reduction in the flow rate, which ultimately drops to zero when annular ice fills the channel at the closure plane. Thus, under the present test conditions, dendritic ice only partially blocks the flow (as it grows along channel surface) while radial inward growth of annular ice leads to the complete flow blockage. In this study, channel closing time is defined as the total duration from nucleation to closure of the annulus, which includes the periods of both dendritic and annular ice growth. Channel closing time is measured as the time between the frame when dendritic ice is first observed (Figure 3.4) and the frame where the top and bottom annular ice fronts merge (Figure 3.5). For case A, the total channel closing time is 3.75 s, out of which the duration of dendritic ice growth (~1 s) is smaller compared to the duration of annular ice growth (~2.7 s).

Figure 3.7 shows a comparison of the time history of external channel wall temperature $T_{wall,ext}$ during freezing for test cases A, B, and C. The data from each different case are aligned in time such that $t$ = 0 s corresponds to the instant of ice nucleation. In Figure 3.7, firstly, the external wall temperature at the time of ice nucleation decreases with an increase in flow rate, which indicates that water is supercooled to lower temperatures at higher flow rates before the nucleation begins. This is also indicated by the shorter period of dendritic growth at the highest flow rate (0.6 s for case C compared to 0.7 s and 1.1 s for cases B and A, respectively), because dendritic ice grows faster with an increase in the degree of supercooling [40]. Secondly, the annular ice growth duration decreases monotonically from case A to C (2.7 s, 1.9 s, and 0.8 s for cases A, B and C, respectively). Finally, the constant $T_{wall,ext}$ during annular ice growth decreases (*i.e.*, $\Delta T$ increases) with an increase in flow rate ($T_{wall,ext}$ = –2°C, –3.5°C and –7°C for cases A, B and C, respectively).

A comparison between the growth behaviors of the two ice formation modes shows that annular ice growth dictates the channel closure. Based on this observation, the next section presents a simplified model that provides an understanding of how the operating parameters influence the annular ice growth time.

### 3.2.2 Model Description

A simplified volume-discretization based model is developed to predict the growth of annular ice thickness during the transient freezing of water flowing inside a straight, cylindrical channel using a lumped system analysis. The following assumptions and simplifications are used in the model formulation:

1. The flow is axisymmetric, laminar, and incompressible.
2. The fluid has a well-defined, distinct freezing point and the phase properties are temperature independent.
3. The discretized elements are assumed to be lumped masses for heat transfer analysis, *i.e.*, the flow has a uniform velocity $\left(V = \dot{m}/\rho_l A\right)$ and temperature profile across the channel cross-section.

4. There is no conduction in the axial direction.
5. The annular ice layer is flat and parallel to the channel wall at each streamwise location.

The model considers annular ice growth from an initial condition at which a thin solid annular ice layer of initial thickness ($R_{wall,int} - R_0$) is already developed at $t$ = 0 s. This is to allow direct comparison to the experiments during which the thin layer of annular ice can only be observed above some minimum thickness. Also, as discussed previously in Section 3.2.1, the annular ice is observed to grow under an isothermal wall condition; hence, the external wall temperature is taken as a constant boundary condition that is lower than the equilibrium freezing point of water.

#### 3.2.2.1 Modeling approach

As shown in Figure 3.8, a channel with external and internal radii of $R_{wall,ext}$ and $R_{wall,int}$, respectively, is uniformly discretized into small control volumes (CV) of length $\Delta z$ in the axial direction, each encompassing the entire channel cross-section. The channel external wall temperature, $T_{wall,ext}$, is maintained at a uniform value lower than the freezing temperature, $T_f$, along the entire length. The water enters the channel at a constant inlet mass flow rate of $\dot{m}_0$ and a mean inlet temperature of $T_0$ $(> T_f)$. Time is discretized in steps of $\Delta t$.

Figure 3.8(b) illustrates a zoomed-in view of a single control volume $i$ at time step $j$. An annular ice layer with interface radius $R_i^{i,j}$ exists in the CV at this time. Water enters the CV at an inlet temperature, $T_{in}^{i,j}$, and a mass flow rate $\dot{m}_{in}^{i,j}$. A mass increment of water adjacent to the ice layer, $\dot{m}_f^{i,j}$, freezes and forms a solid ice layer of thickness $\Delta {R_i}^{i,j}$ over a time step of $\Delta t$. The remaining water flow, $\dot{m}_{out}^{i,j}$, exits the control volume at an outlet temperature, $T_{out}^{i,j}$. The water inside the CV is assumed to be at a uniform mean temperature during the heat transfer process, $T_m^{i,j}$.

The mass transfer equation for the above process in the CV can be written as:

$$\dot{m}_{in}^{i,j} - \dot{m}_{out}^{i,j} = \dot{m}_f^{i,j} = \rho_s 2\pi R_i^{i,j} \frac{\Delta {R_i}^{i,j}}{\Delta t} \Delta z \tag{3.1}$$

As water flows through the CV, it cools due to the convective heat loss, which can be written as:

$$\dot{Q}_{conv} = \dot{Q}_{water,in} - \dot{Q}_{water,out} \tag{3.2a}$$

Equation $(3.2a)$ can be expressed as:

$$\frac{Nu\ k_l}{2R_i^{i,j}} 2\pi R_i^{i,j} \Delta z \left(T_m^{i,j} - T_i\right) = \dot{m}_{in}^{i,j} c_{p,l} \left(T_{in}^{i,j} - T_f\right) - \dot{m}_{out}^{i,j} c_{p,l} \left(T_{out}^{i,j} - T_f\right) \tag{3.2b}$$

The mass of water freezing, $\dot{m}_f^{i,j}$, releases latent heat ($\dot{Q}_{lat}$) at the freezing temperature, $T_f$; this newly formed ice must cool down further to the temperature of the pre-existing ice layer, $T_i$, by releasing sensible energy ($\dot{Q}_{ice,sens}$). Therefore, the total energy released in the formation of the ice layer can be written as:

$$\dot{Q}_{rel} = \dot{Q}_{lat} + \dot{Q}_{ice,sens} = \dot{m}_f^{i,j} \left[L + c_{p,s}\left(T_f - T_i\right)\right] \tag{3.3}$$

Since $T_{wall,ext} < T_i$, the CV cools via radial conduction through the channel wall:

$$\dot{Q}_{cond} = 2\pi \Delta z \frac{\left(T_i - T_{wall,ext}\right)}{\frac{\ln\left(R_{wall,int}/R_i^{i,j}\right)}{k_s} + \frac{\ln\left(R_{wall,ext}/R_{wall,int}\right)}{k_{bs}}} \tag{3.4}$$

For energy conservation in the CV, the sum of energy convected from the water (sensible), released by ice formation (latent), and removed from the ice layer that is formed (sensible) must be equal to the energy conducted radially through the channel wall

$$\dot{Q}_{conv} + \dot{Q}_{rel} = \dot{Q}_{cond} \tag{3.5a}$$

On substituting Equations $(3.2b)$, (3.3) and (3.4), Equation $(3.5a)$ becomes:

$$\dot{m}_{in}^{i,j} c_{p,l}\left(T_{in}^{i,j} - T_f\right) - \left(\dot{m}_{in}^{i,j} - \dot{m}_f^{i,j}\right) c_{p,l}\left(T_{out}^{i,j} - T_f\right) + \dot{m}_f^{i,j}\left[L + c_{p,s}\left(T_f - T_i\right)\right]$$
$$= -2\pi\Delta z \frac{\left(T_i - T_{wall,ext}\right)}{\frac{\ln\left(R_{wall,int}/R_i^{i,j}\right)}{k_s} + \frac{\ln\left(R_{wall,ext}/R_{wall,int}\right)}{k_{bs}}} \qquad (3.5b)$$

The boundary conditions can be written as:

$$T_{wall,ext} = \text{constant at } r = R_{wall,ext}$$
$$T_{in}^{1,j} = T_0$$
$$\dot{m}_{in}^{1,j} = \dot{m}_0$$

The model is evaluated with an initial radius of the annular ice front:

$$R_i^{i,1} = R_0$$

#### 3.2.2.2 Model simplification

An order-of-magnitude scaling analysis is performed to simplify the overall energy balance given in Equation $(3.5b)$. Values for the variables based on the experimental conditions are substituted into the equation to determine the dominant terms. See APPENDIX A.3 for details of this scaling analysis.

The scaling analysis identifies that the latent heat, $\dot{Q}_{lat}$**,** dominates over the convected energy, $\dot{Q}_{conv}$, and the sensible cooling of ice, $\dot{Q}_{ice,sens}$. Therefore, Equation $(3.5b)$ can be simplified to:

$$\rho_s 2\pi R_i^{i,j} \frac{\Delta {R_i}^{i,j}}{\Delta t} \Delta z L \approx -2\pi\Delta z \frac{\left(T_i - T_{wall,ext}\right)}{\frac{\ln\left(R_{wall,int}/R_i^{i,j}\right)}{k_s} + \frac{\ln\left(R_{wall,ext}/R_{wall,int}\right)}{k_{bs}}} \qquad (3.5c)$$

This implies that the radial conduction through the ice layer and the channel wall is the dominant mode that drives the annular ice growth in small channels at small flow rates.

An expression for the annular ice growth period ($t_{ann}$) can be obtained by integrating Equation $(3.5c)$ with respect to $R_i$ from $R_i = R_{wall,int}$ $(\text{at } t = 0)$ to $R_i = 0$ $(\text{at } t = t_{ann})$. It should be noted that although the model is evaluated from an initial radius $R_i = R_0$ at $t = 0$ for comparison to experiments, the lower limit for integration is set to $R_i = R_{wall,int}$ here to obtain an expression for $t_{ann}$ that captures the annular ice growth starting from the channel inside radius.

$$t_{ann} \approx \frac{\rho_s L}{\left(T_i - T_{wall,ext}\right)} \frac{R_{wall,int}^2}{2} \left( \frac{1}{2k_s} + \frac{\ln\left(R_{wall,ext}/R_{wall,int}\right)}{k_{bs}} \right) \tag{3.6}$$

This equation indicates that $t_{ann}$ varies directly with the channel size and inversely with the temperature difference between the ice-water interface and the channel wall (as well thermophysical properties of water and channel material). Therefore, a small channel diameter and a large temperature difference would facilitate a faster closure through annular ice. Myers and Low [45] adopted a different modeling approach where they used lubrication theory to approximate the period of annular ice growth in microchannels and arrived at the same conclusion.

#### 3.2.2.3 Solution algorithm

The above system of Equations $(3.1)$, $(3.2b)$, and $(3.5b)$ is solved for the three unknown variables, $\dot{m}_{in}^{i,j}$, $T_{out}^{i,j}$, and $\Delta {R_i}^{i,j}$ using a numerical procedure implemented in MATLAB. A Nusselt number was derived via a scaling comparison of the convective heat transfer that would cause a sensible temperature change to the heat conduction across the ice-water interface, $h\left(T_m^{i,j} - T_i\right) = k_l \left(\frac{dT}{dr}\right)_{r=R_i}$, such that $Nu = 2\left(\frac{dT}{dr}\right)_{r=R_i} / \left(\frac{T_m^{i,j} - T_i}{R_i}\right)$. Assuming a uniform velocity and temperature profile in a cylindrical channel, $\left(\frac{dT}{dr}\right)_{r=R_i}$ scales as $\left(\frac{T_m^{i,j} - T_i}{R_i}\right)$, and therefore $Nu \approx 2$. On substituting $Nu$ in Equation $(3.2b)$, the equations can be solved for all control volumes, at a given time, by marching axially along the channel in the direction of flow. The initial value of $T_{out}^{i,j}$ is unknown; an initial guess value of $T_{out}^{i,j} = T_{in}^{i,j}$ is taken and the equations are solved sequentially for all the unknown variables. The mean temperature, $T_m^{i,j}$, is calculated as the mean of $T_{in}^{i,j}$ and $T_{out}^{i,j}$. The solution is then iterated by replacing the guess value with the solution of $T_{out}^{i,j}$ from the previous iteration until the error between calculated value converges to within a

threshold of $10^{-5}$°C. After all the variables are solved at a given time, the solution then marches in time by updating the position of the ice-water interface within each control volume:

$$R_i^{i,j+1} = R_i^{i,j} - \Delta R_i{}^{i,j} \Delta t \tag{3.7}$$

### 3.2.3 Comparison with the Model

In order to compare the model-predicted annular ice growth and channel closing time against the experiments, the external wall temperature during annular ice formation and the water inlet temperature are input to the model based on the experimental conditions. The mass flow rate at the inlet is taken as a constant at all time steps, at a value before freezing begins in the experiments. Even though the flow rate reduces during freezing in the experiments, this constant input mass flow rate to the model has a negligible effect on the predictions because the convection term is negligible in the energy conservation equation (APPENDIX A.3). These boundary conditions are summarized for all of the test cases in Table 3.2. The channel is divided into 2000 CVs of equal length, $\Delta z = 10^{-5}$ m, resulting in total length of 0.2 m that is equal to the cooled length of the channel in the test cell. Each time step ($\Delta t$) is $10^{-3}$ s. The interface temperature, $T_i$, is assumed to be equal to the equilibrium freezing temperature of $T_f = 0$°C.

Figure 3.9 shows a comparison between the predicted and measured values of the annular ice front position (normalized as $R_{open}/R_{wall,int}$) versus time at distance of $z/L$ = 0.95 from the channel inlet for each of the test cases. $R_{open}$ is calculated as the average of radii of the upper and the lower annular ice fronts, obtained from the images in the experiment using the refraction correction procedure described in APPENDIX A.2.

The initial time $t$ = 0 s is set as the instant when $R_{open}/R_{wall,int}$ = 0.8, *i.e.*, the annular ice layer thickness ($R_{wall,int} - R_i$) = 50 $\mu$m. The experimental values of $R_{open}$ are extracted from the high-speed images at an interval of 0.2 s for each trial. The experimental curves show the average of 8 repeated trials for each of the cases. The error bars represent the standard deviation in data for these repeated trials. The trends of the model predictions and the experimental observations are in reasonably good agreement with each other; some deviations from the experimental values are expected due to the differences between the experimental conditions and modeling

assumptions/inputs. For example, the model assumes a constant temperature difference $\Delta T = (T_i - T_{wall,ext})$, entered as an input; however, in the experiments, $T_{wall,ext}$ reduces slightly (or $\Delta T$ increases) when the annular ice is thick and loses sensible heat. The model assumes uniform velocity and temperature across the channel cross-section for a CV, while in the experiments, they have radially varying profiles. Also, the thermal conductivity of borosilicate glass is assumed to be $k_{bs} = 1.08$ W/m-K at 25°C but would be lower at the temperatures encountered in experiments, thereby resulting in slower annular growth than predicted.

As was described in Section 3.2.2.2, conduction from the outer wall is the dominant heat transfer mode governing the annular ice growth. The expression for annular ice growth time (Equation (3.6)) shows that the temperature difference $\Delta T = (T_i - T_{wall,ext})$ is the key factor driving conduction and the annular growth rate. Therefore, it is expected that the channel would close sooner at higher flow rates for which the channel wall is cooler during freezing. This is evident from the model prediction shown in Figure 3.9, which matches the experimental trend of decreasing closure times with decreasing external wall temperatures, from case A to case C. It is important to mention here that the water flow rate has no direct influence on the annular ice growth because the convective terms are negligible compared to the conduction terms (see APPENDIX A.3). However, the flow rate does play an indirect role in setting the degree of supercooling before nucleation which ultimately determines $T_{wall,ext}$ and hence the temperature difference ($\Delta T = T_i - T_{wall,ext}$) driving annular ice growth.

## 3.3 Conclusions

The freezing of water flowing through a glass channel of small diameter ($D$ = 500 $\mu$m) is visualized and characterized with a focus on understanding the factors that affect the closing times in small channels, for potential microfluidic ice valve applications. The water is supercooled by exposing the channel external wall to cold $N_2$ gas, and the freezing process is captured using high-speed imaging until closure occurs in the channel. Freezing is visualized to occur through a mixed mode of ice formation: a thin, sheet-like layer of dendritic ice appears for a brief duration after nucleation, which is followed by slower inward radial growth of a thick, solid ice annulus. The characteristics of each mode are studied using the temperature and flow rate measurements

synchronized with the high-speed visualization. Three different water flow rates (0.5, 1, and 2 ml/min) are used to analyze the effect of flow rate on the freezing temperatures and the channel closing times. A simple finite-volume based model is developed that successfully predicts the annular ice growth duration. The following key conclusions are drawn from the present study:

- Freezing in the channel only starts at a supercooled temperature with the formation of dendritic ice. The latent heat released upon nucleation increases the ice-water interface temperature to the saturation freezing point, $T_f$, and a constant external channel wall temperature to $T_{wall,ext}$ that depends on the flow rate.
- Following ice nucleation in supercooled water, ice dendrites form a thin layer adjacent to the wall. This layer rapidly propagates along the channel in both streamwise directions from the point of nucleation and covers the entire channel inside surface.
- The dendritic ice formation is followed by the growth of a thick, solid ice annulus which appears at the channel inside circumference along the entire channel length. This ice annulus grows radially inward, at a nearly isothermal wall temperature ($T_{wall,ext,annular}$), and eventually closes the channel.
- The dendritic ice causes some obstruction in the flow path (as indicated by an immediate drop in the water flow rate following dendritic ice appearance) but complete flow blockage and channel closure is ultimately caused by the annular ice for the conditions in this study.
- The annular ice growth is governed by the radial conduction of the released latent heat; convection plays a negligible role, and hence, the flow rate does not have a direct influence on the annular ice growth rate. The flow rate does, however, dictate the degree of supercooling required for nucleation, which determines the temperature difference driving the annular ice growth. In particular, at higher water flow rates, a high degree of supercooling is required to initiate freezing which results in a large temperature difference and a faster annular ice growth (shorter closing time) compared to lower flow rates. Therefore, the flow rate indirectly affects the channel closing time.

It is also concluded that the latent heat accounts for a large portion of the released energy that needs to be removed to attain channel closure. Therefore, transferring this energy released out of the channel during freezing in the shortest possible time is key to accelerating annular ice growth

and increase the closing speed. In practice, the driving temperature difference and the resistance to heat conduction are important parameters that must be considered in the design of high-speed-response ice valves for microfluidic platforms.

**Nomenclature**

| | |
|---|---|
| $A$ | channel cross-sectional area |
| $c_p$ | specific heat at constant pressure |
| $D$ | channel inner diameter ($D = 2R$) |
| $h$ | convective heat transfer coefficient |
| $k$ | thermal conductivity |
| $l$ | channel length |
| $L$ | latent heat of fusion |
| $\dot{m}$ | mass flow rate |
| $n$ | refractive index |
| $Nu$ | Nusselt number ($Nu = \frac{hD}{k}$) |
| $P$ | pressure |
| $\dot{Q}$ | heat transfer rate |
| $r$ | radial coordinate |
| $R$ | channel inner radius |
| $\Delta R$ | change in radius during single time step |
| $Re$ | Reynolds number ($Re = \frac{\dot{m}D}{\mu A}$) |
| $t$ | time |
| $\Delta t$ | time step |
| $T$ | temperature |
| $\Delta T$ | temperature difference between ice-water interface and the external channel wall ($\Delta T = T_i - T_{wall,ext}$) |
| $W$ | water flow rate ($W = \dot{m}/\rho_l$) |
| $x$ | transverse position relative to channel centerline (Figure 3.3) |
| $y$ | vertical position relative to channel centerline (Figure 3.3) |
| $z$ | axial or streamwise position along the channel centerline (Figure 3.3) |
| $\Delta z$ | length of a unit control volume in the axial direction |

### *Greek symbols*

| | |
|---|---|
| $\mu$ | dynamic viscosity |
| $\rho$ | density |
| $\theta$ | angle between the normal and incident/refracted light rays |

### *Subscripts*

| | |
|---|---|
| $ann$ | annular region |
| $bs$ | borosilicate glass |
| $cav$ | test cell cavity |
| $cond$ | conducted heat energy |
| $conv$ | convected heat energy |
| $ext$ | external |
| $f$ | freezing |
| $i$ | ice-water interface |
| $ice$ | ice |
| $in$ | inlet |
| $int$ | internal |
| $l$ | liquid phase (water) |
| $lat$ | latent heat |
| $m$ | mean |
| $n$ | nucleation |
| $o$ | initial |
| $out$ | outlet |
| $open$ | open area of channel |
| $rel$ | released (energy) |
| $s$ | solid phase (ice) |
| $sens$ | sensible (energy) |
| $wall$ | channel wall |
| $water$ | water |

### *Superscript*

| | |
|---|---|
| $i$ | index for a unit control volume |
| $j$ | index for time step |

Table 3.1. Test cases and their corresponding water flow rates, upstream water pressure, and the steady state cavity temperatures at freezing. Digits in brackets denote standard deviation in measurements over 8 experimental trials each.

| Case | Water flow rate, $W = \frac{\dot{m}}{\rho_l}$ (ml/min) | Upstream water pressure, $P_{water}$ (kPa; absolute) | Water inlet temperature, $T_{in}$ (°C) | Cavity temperature, $T_{cav}$ (°C) |
|---|---|---|---|---|
| A | 0.5 | 9.03 | 8 (±2) | –27.5 (±9.2) |
| B | 1 | 22.03 | 8 (±2) | –33.9 (±4.6) |
| C | 2 | 39.48 | 8 (±2) | –56.2 (±5.5) |

Table 3.2. Test cases and their corresponding boundary conditions input to the model.

| Case | Water inlet temperature, $T_0$ (°C) | Wall temperature, $T_{wall,ext}$ (°C) | Inlet mass flow rate, $\dot{m}_0$ ($\times 10^{-6}$ kg/s) |
|---|---|---|---|
| A | 8 | –2 | 8.33 |
| B | 8 | –3.5 | 16.7 |
| C | 8 | –7 | 33.3 |

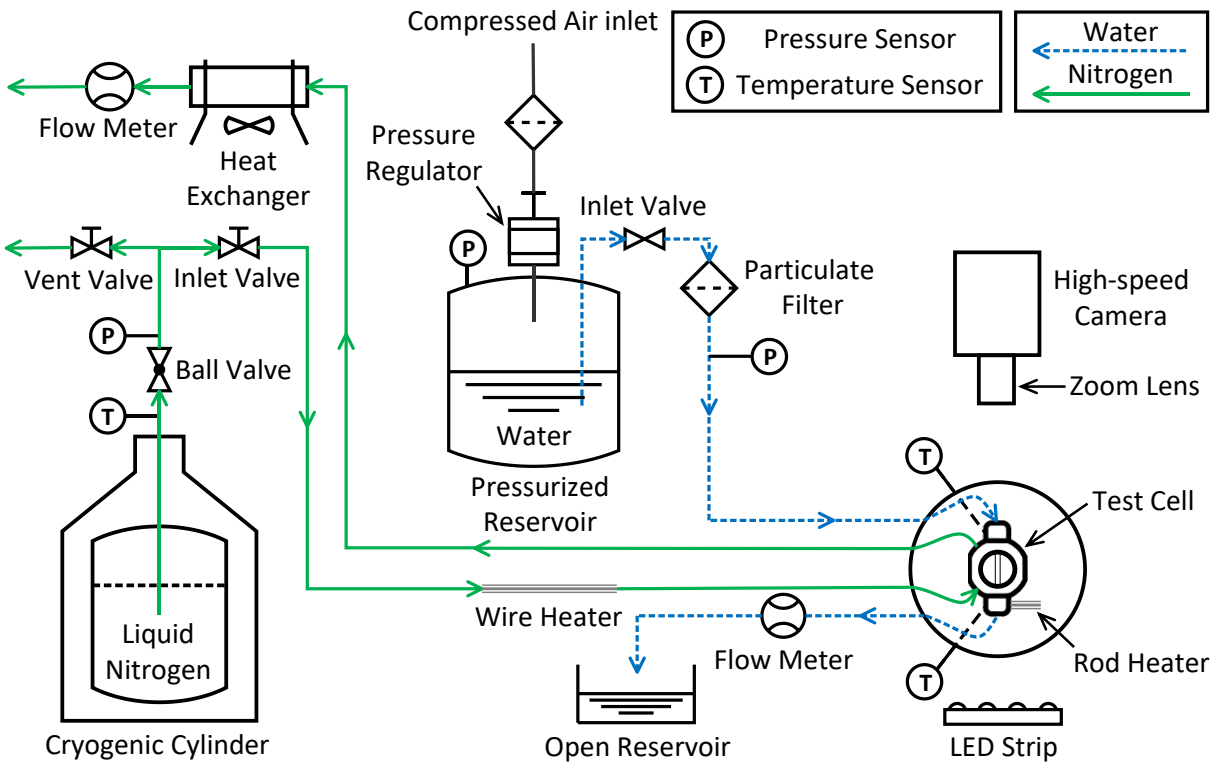


Figure 3.1. Schematic diagram of the experimental test facility.

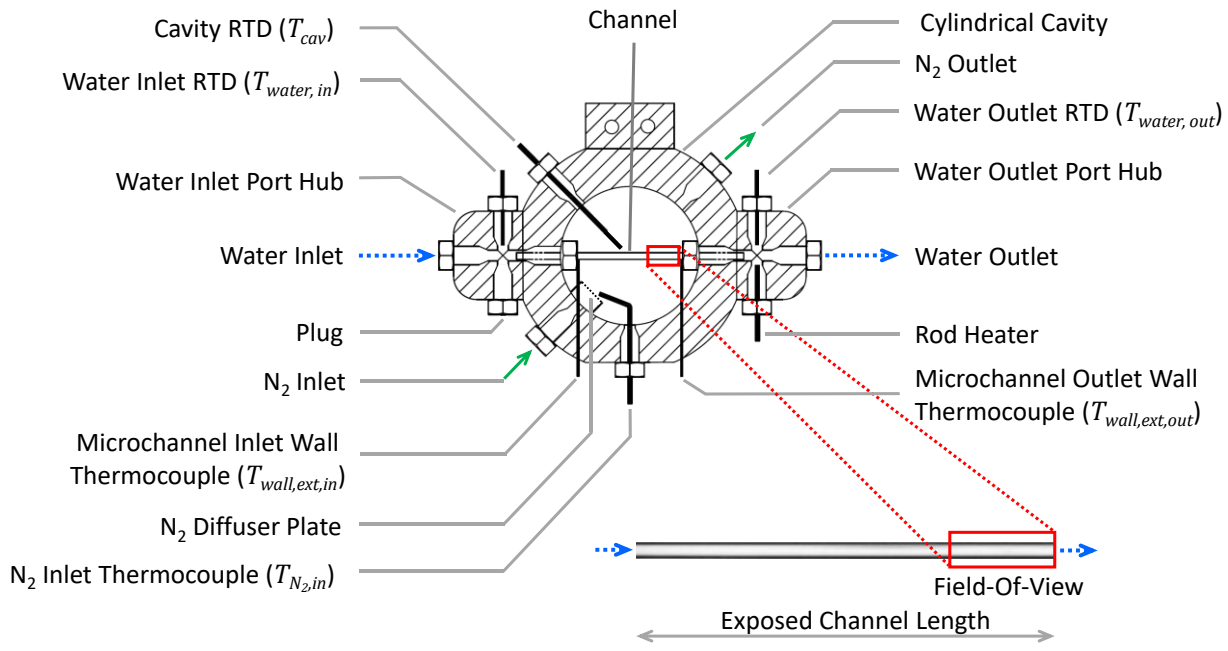


Figure 3.2. Sectional view of the test cell (along the horizontal mid-plane) and the measurement instrumentation. Inset shows the exposed channel length and the field-of-view.

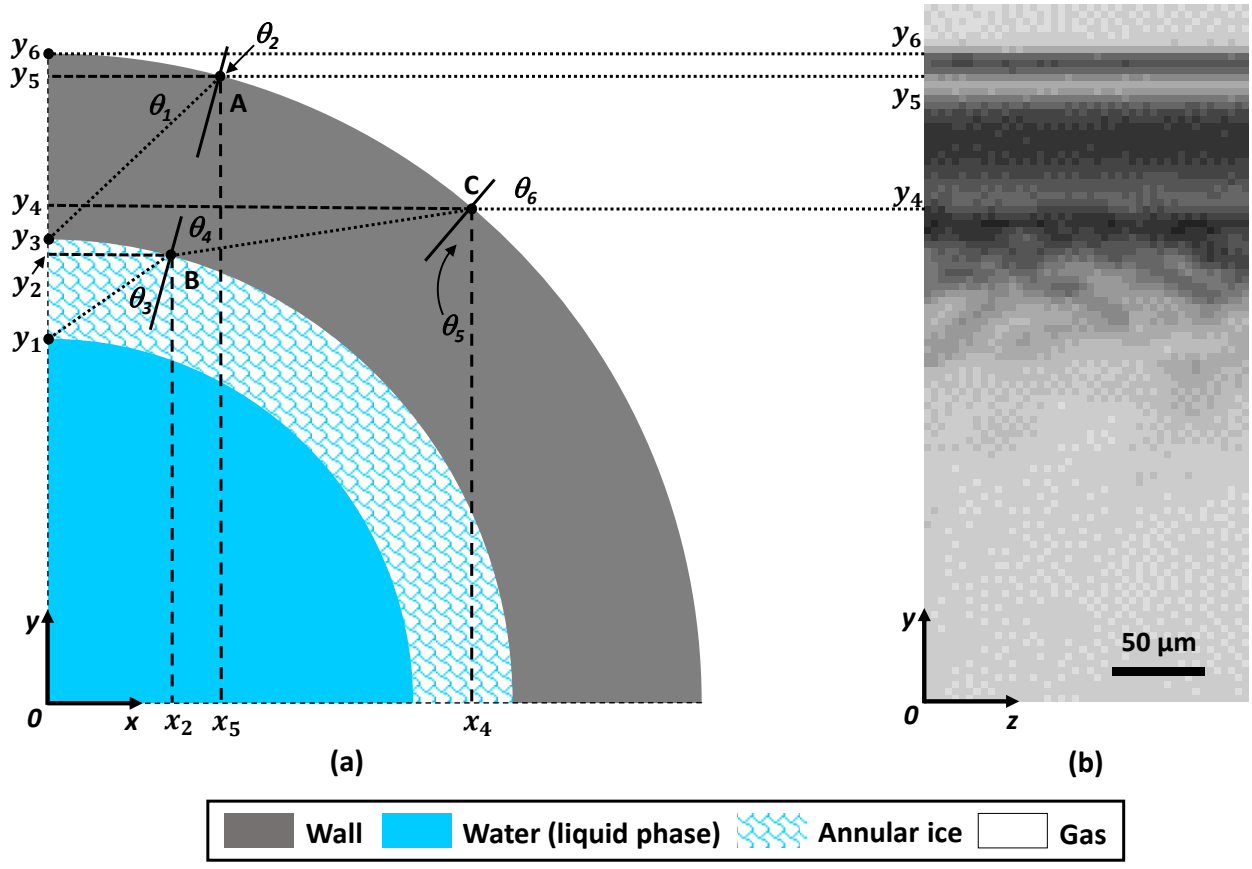


Figure 3.3. (a) Schematic diagram illustrating light refraction through ice-glass and glass-gas interfaces and (b) the corresponding high-magnification image captured by the camera. Actual locations of the key points on the interfaces are marked by dots; dotted lines show pathlines traced by light from these points of interest in the *x*-*y* plane that are collected by the camera in the *y*-*z* plane. Dashed lines mark the *x*-*y* position of the points where light is refracted along the pathlines and solid lines indicate the outward normal to the interfaces at the points of refraction.

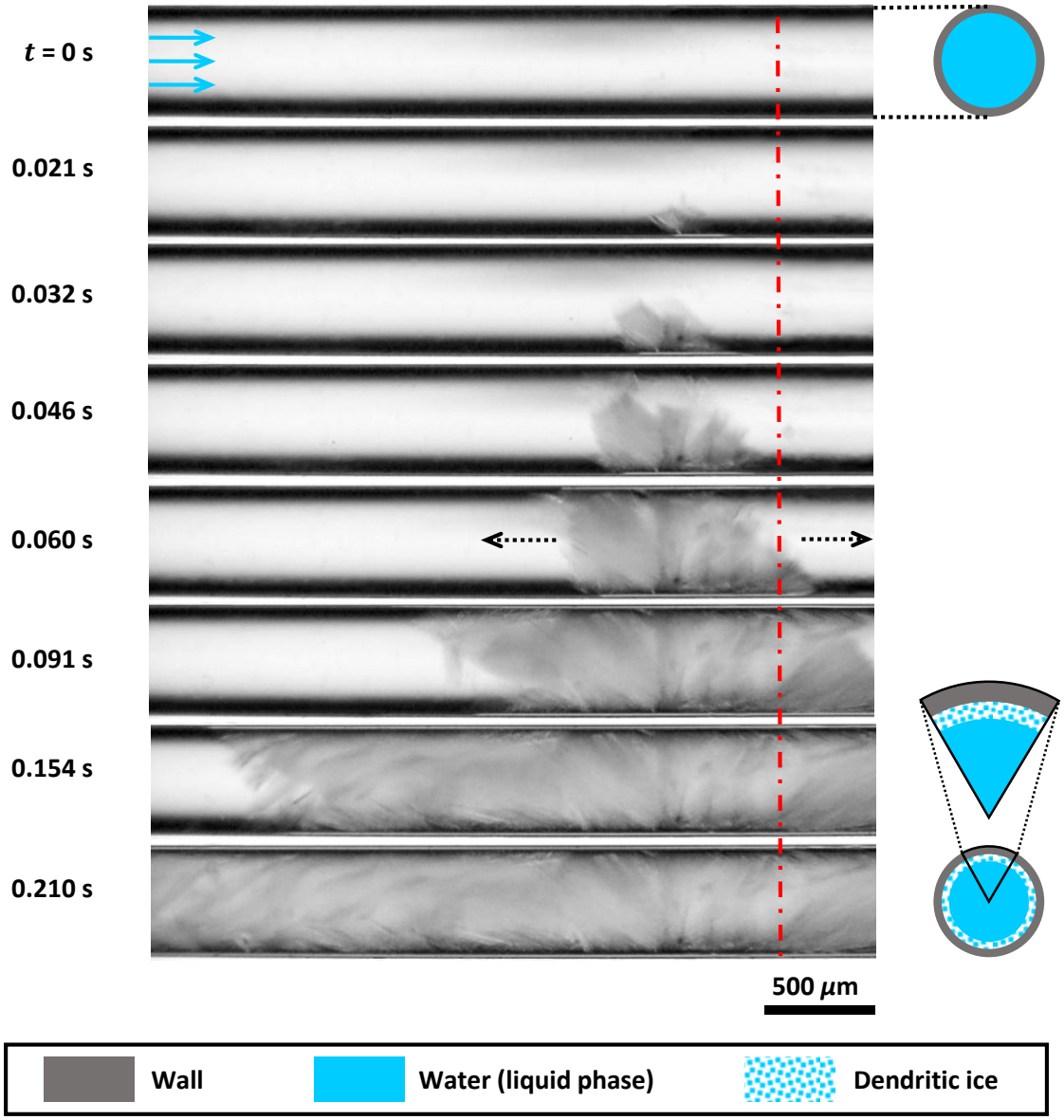


Figure 3.4. Time sequence of images showing dendritic ice formation and growth as the freezing initiates in the channel for case A. The schematic diagrams on the right show the channel cross-section at the closure plane (dash-dot red line). The wall, water, and dendritic ice regions are shaded as indicated in the legend. Flow direction is from left to right.

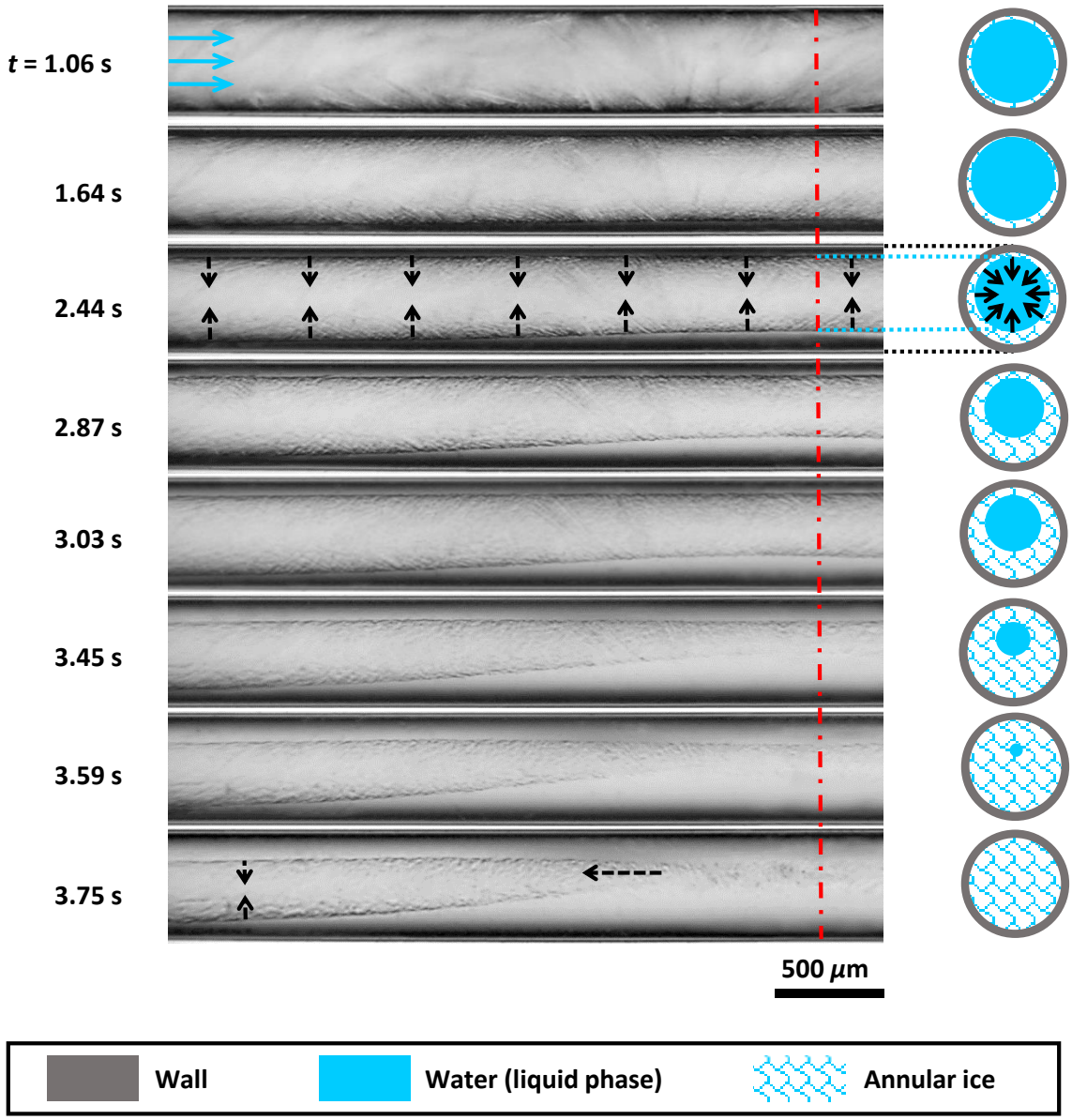


Figure 3.5. Time sequence of images showing annular ice growth and closure in the channel for case A. The schematic diagrams on the right show the channel cross-sections at the closure plane (dash-dot red line) with the wall, water, and ice regions shaded as indicated in the legend. Flow direction is from left to right. The black dashed arrows indicate the direction of annular ice growth.

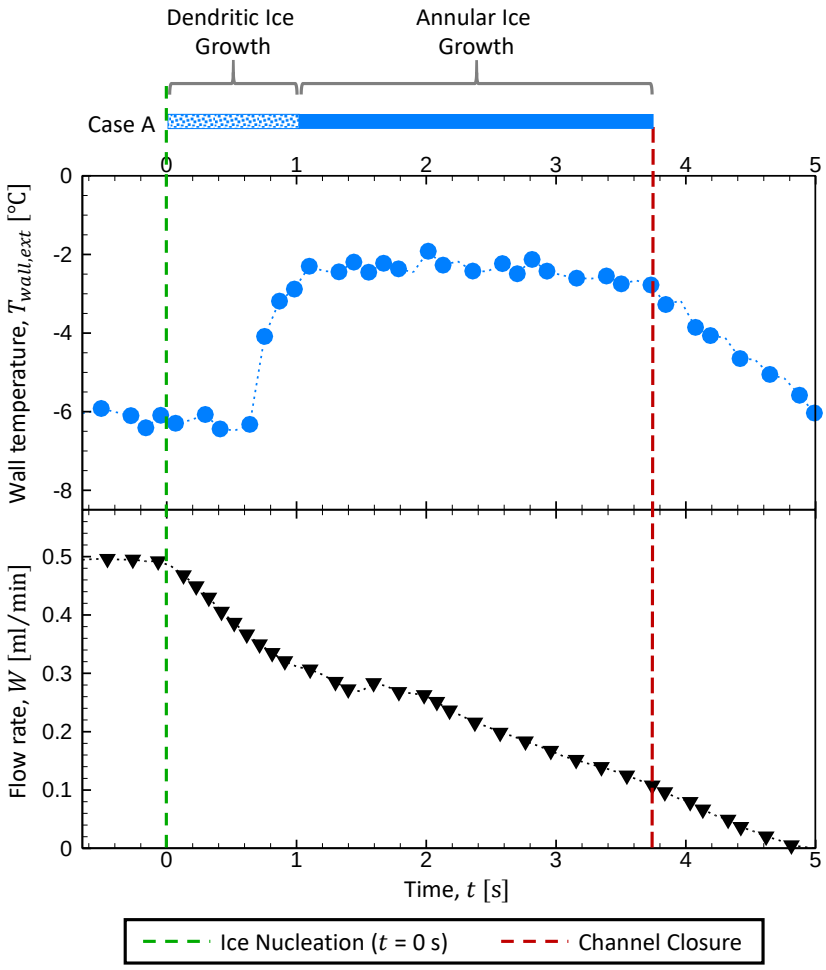


Figure 3.6. Synchronized temporal variations of the wall temperature and the water flow rate as freezing occurs for test case A. The durations of dendritic and annular ice growth are indicated in the bar on the top. The water inlet temperature is maintained constant at 8 (±2)°C.

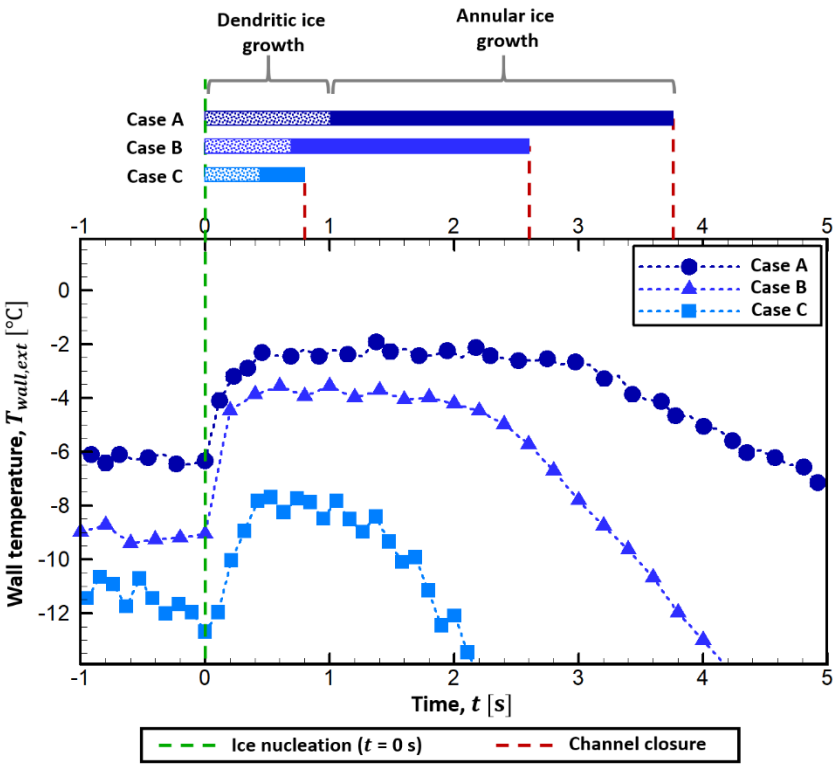


Figure 3.7. A comparison of temporal variation of the wall temperature for the three test cases. The bar on top shows a comparison of the periods of dendritic and annular ice growth.

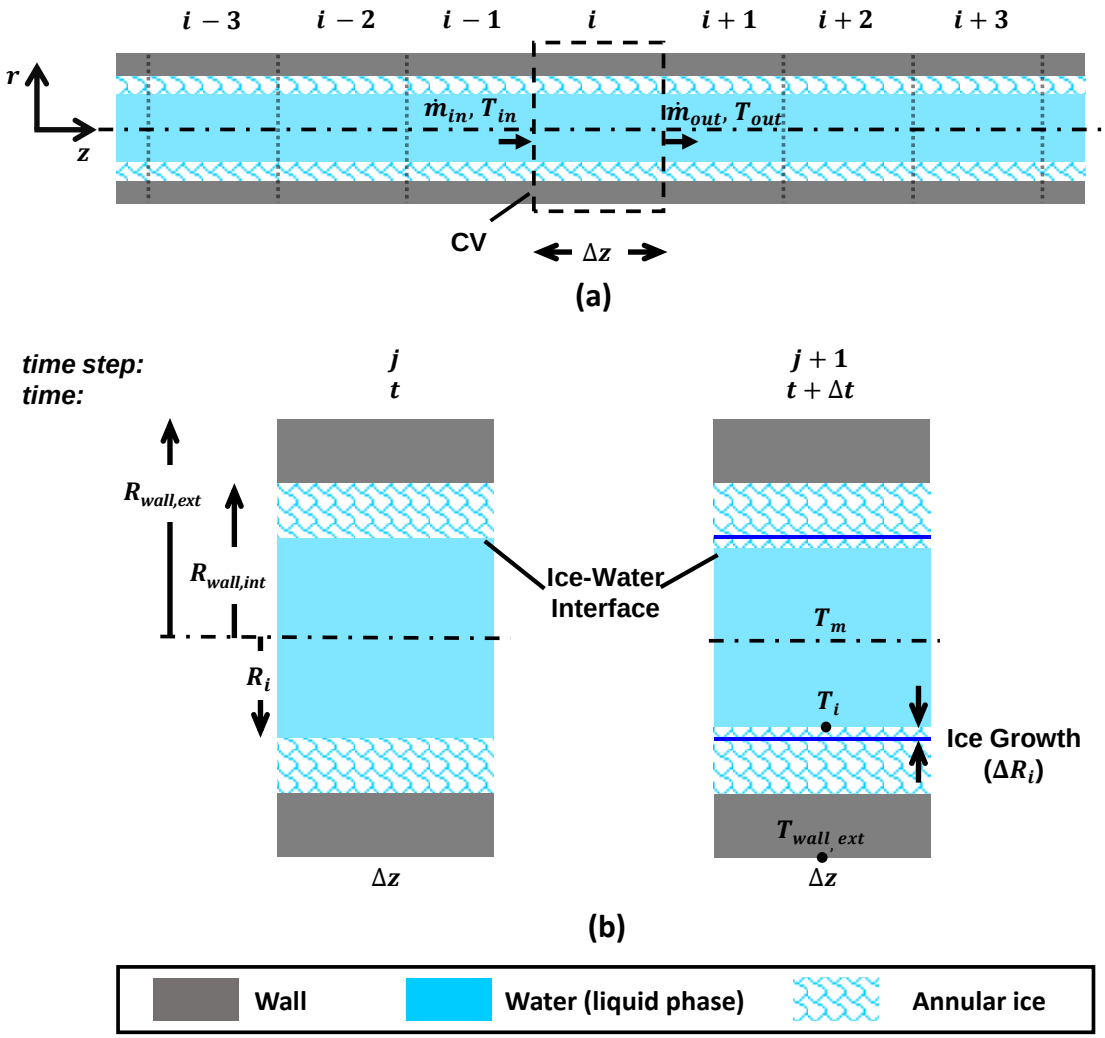


Figure 3.8. Schematic diagrams illustrating (a) the control volumes in the channel and (b) the $i^{th}$ control volume at times $t$ and $t + \Delta t$.

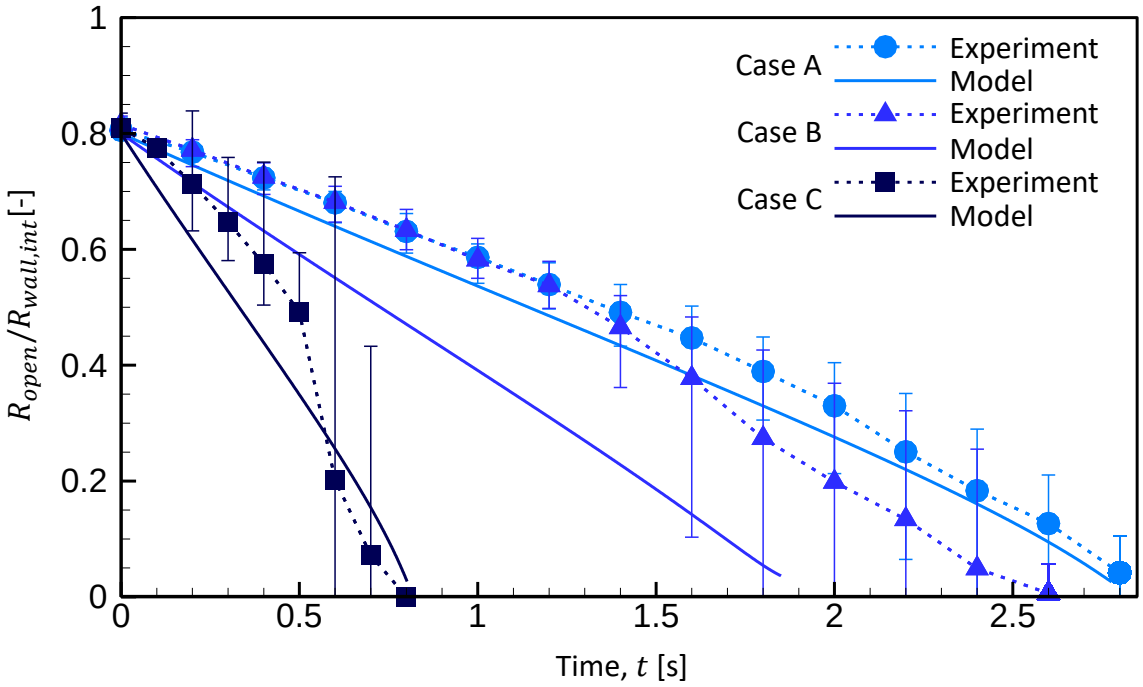


Figure 3.9. Comparison of the model-predicted and measured annular growth and closure rates for cases A, B, and C.

# CHAPTER 4. THE EFFECT OF CHANNEL DIAMETER ON FLOW FREEZING IN MICROCHANNELS

This chapter aims to experimentally demonstrate that reducing the channel diameter is a promising approach to achieving fast channel closure using ice valves in microfluidic platforms. The effect of channel diameter on the channel closing time is characterized by investigating the flow freezing process using high-speed visualization synchronized with the external channel wall thermocouple readings for three channel inner diameters ($D = 100$ μm, 300 μm, and 500 μm, respectively) at a constant-pressure-driven water flow rate of 0.3 ml/min. The channel closing times are determined visually from the high-magnification images. Based on a simplified annular ice growth model [66], the factors affecting the closing time are identified and the critical role of channel diameter is examined. The nomenclature for this chapter is presented after the chapter text, before the figures. The material presented in this chapter is under review for possible publication in the *International Journal of Heat and Mass Transfer* [71].

## 4.1 Experimental Setup and Procedures

The experimental set-up used in this study is identical to that used in CHAPTER 3 except for the additional channel diameters investigated. Key details are summarized here. Figure 4.1 (a) shows a schematic diagram of the test facility. The facility consists of an open water-flow loop, an open nitrogen-flow loop, and the test cell. Water flow through the channel is driven by the pressure difference between a pressurized reservoir and the ambient. A constant-pressure cryogenic cylinder is used to deliver cold $N_2$ gas to the test cell via the nitrogen open-loop system. A vent valve is placed in the flow path downstream of the cylinder to vent some portion of the $N_2$ that boils off as it exits the cylinder; this reduces the back pressure and allows a continuous flow of gas from the cylinder to the test cell. The gas temperature entering the test cell is controlled locally by a wire heater that is wrapped around the tubing just upstream of the test cell (see Figure 4.1(a)).

The test cell (see Figure 4.1(b)) is a 3-D printed component (VeroClear Fullcure810, Objet) that consists of a hollow cylindrical cavity (25 mm in diameter) with various ports to support the water flow, nitrogen flow, and measurement probes. A cylindrical borosilicate glass microchannel is

mounted horizontally between two diagonally located ports in the cavity and sealed in place using miniature compression fittings and epoxy, as shown in Figure 4.1(b). The channel is cooled by the cold $N_2$ gas flowing through the cavity. In this study, three different channel sizes are used with nominal inner diameters ($D$) of 500 μm, 300 μm, and 100 μm. These channels have a wall thickness ($R_{wall,ext} - R_{wall,int}$) of 100 μm, 50 μm, and 20 μm, respectively. The channel length exposed to the cold gas inside the cavity, $l$, is 20 mm (see Figure 4.1(b)). A T-type thermocouple (5TC-TT-T-40-36, Omega; ±1.0°C) is carefully placed in contact with the channel external wall near the inlet ($z/l = 0.1$) using thermally conductive epoxy (Duralco 120, Cotronics). The cavity is sealed shut with a 3.6 mm-thick transparent polycarbonate cover on the top and bottom to contain the gas flow within the cavity and to enable visualization.

There is a port hub on either side of the test cell that contains three ports: for the flow paths, water temperature measurements, and rod heater (only used at the outlet hub). The rod heater is used to warm the outlet hub, which ensures that water temperature is lowest in the field-of-view and therefore the ice nucleation and the freezing process are easily visualized. All the port connections are sealed using miniature compression fittings and epoxy to prevent leakage.

The ice formation process inside the channel is visualized using a high-speed camera (VEO 710L, Phantom) fitted with a high-magnification zoom lens (VHZ50L, Keyence). Different levels of magnification are needed for each channel size. The corresponding field of view, as marked in Figure 4.1(b), is $0.6 < z/l < 1$ for $D = 500$ μm, $0.774 < z/l < 1$ for $D = 300$ μm, and $0.9 < z/l < 1$ for $D = 100$ μm. Flow visualization is synchronized with the temperature readings using a pulse generator (Model 505-4C, Berkeley Nucleonics Corporation). The channel is uniformly backlit using a high-intensity LED strip with an integrated diffuser (BL138, Advanced Illumination). The images are acquired at 10,000 fps with an exposure time of 95 μs and a visualization window of 960×112 pixels. This window size corresponds to an optical resolution of 8.8 μm/pixel (optical zoom of 2.3×), 4.8 μm/pixel (4.2×), and 2.1 μm/pixel (9.7×) for channel diameters $D = 500$ μm, 300 μm, and 100 μm, respectively. The external wall thermocouple readings are recorded at a sampling frequency of 100 Hz using the data acquisition unit (cDAQ-9178, National Instruments). The cavity temperature is recorded at a frequency of 0.22 Hz using another data acquisition unit (34970A, Agilent) with a 20-channel multiplex module using a

LabVIEW interface.

To start a test, the flow is established in the water line by pressurizing the reservoir. Depending on the channel diameter, the reservoir is pressurized to a set value to generate a constant-pressure driven flow of 0.3 ml/min. The $N_2$ flow to the test cell is then initiated by controlling the supply and vent valves. Subsequently, the power to the inline $N_2$ heater is turned on to control the cavity temperature and is adjusted such that the cavity temperature reaches $T_{cav}$ = 10°C (with a standard deviation of ±2°C across all the test runs). At this point, the compressed-air pressure to the water reservoir is controlled to reduce the water flow rate to the desired setting. Next, the power to the $N_2$ gas heater is reduced in a step-wise manner to reduce the cavity temperature and supercool the water until ice nucleation is observed in the channel. The power levels are chosen such that the cavity temperature reduces by ~4–5°C at each step. At each power level, the system is allowed to attain a steady-state condition, where the standard deviation in both $T_{cav}$ and $T_{wall,ext}$ reduces to less than 1°C over a 10 min interval and the temperature difference between them becomes constant. The water inlet temperature for all test cases is approximately 10°C when nucleation occurs. Multiple trials are performed for each channel diameter by repeating this same test procedure. Data are acquired for 8 repeated runs for each channel diameter.

## 4.2 Results and Discussion

### 4.2.1 Effect of channel diameter on the ice formation modes and channel closing time

The flow freezing of water in microchannels of different diameters is presented here, including the measured temperature readings and visualizations of the freezing process after ice nucleates at the water-wall interface. The different ice formation modes are identified, and the channel closing time is measured for different channel diameters.

Figure 4.2(a) and (b) show a time sequence of high-magnification images of the ice formation process for channel diameters of $D = 500$ μm and 100 μm, respectively. These images show the process starting from the dendritic ice nucleation at the channel inside surface to complete closure of the channel by inward growth of annular ice. This process of dendritic ice growth followed by annular ice closure is observed in all three channel diameters;

APPENDIX B includes a time sequence of images for the intermediate diameter, $D = 300$ μm.

Dendritic ice nucleation occurs at the water-wall interface near the channel outlet. Following nucleation ($t = 0$ s), the dendritic ice grows rapidly along the channel wall in the axial upstream direction and covers the entire field-of-view within $t = 0.08$ s and 0.006 s for $D = 500$ μm and 100 μm, respectively. Because dendritic ice is formed only in supercooled water [35–40,68,72], we infer that the water adjacent to the internal channel wall is supercooled.

As shown in Figure 4.2(a) at $t = 0.04$ s, the dendritic ice growth along the inner front surface (i.e., in front of the focal plane) and the along the inner back surface (i.e., behind the focal plane) appears as two distinct layers. In addition, these distinct ice layers are not connected by any matrix of dendrites. Based on these visualizations, it can be inferred that the dendritic ice grows only as a thin layer adjacent to the wall and does not fill the entire channel cross-section. This behavior is consistent with many previous studies [68–70,72] on the growth of dendrites in supercooled water, which have shown that the dendritic ice tends to grow along a wall rather than into the bulk. This occurs because the channel wall has higher thermal diffusivity and acts as a heat sink for the latent heat released during ice formation. In Figure 4.2(b), a higher magnification (9.7× for $D = 100$ μm compared to 2.3× for $D = 500$ μm) is used due to the smaller channel size.

The dendritic ice nucleates when the wall temperature is below the equilibrium freezing point. Formation of dendritic ice is accompanied by latent heat release, which rapidly increases the wall temperature and brings the ice-water interface to the equilibrium freezing temperature. Figure 4.3 shows a comparison of the time history of external channel wall thermocouple readings, $T_{wall,TC}$, during the freezing process for all 3 channel diameters. The data from each case are aligned in time such that $t = 0$ s corresponds to the instant of ice nucleation. The short delay observed between the ice nucleation and the rise in temperature readings is due to the finite amount of time taken by the dendritic ice to traverse the channel length and reach the inlet where the temperature is measured. As the dendritic ice grows on the wall, latent heat is released continuously, and the temperature begins to climb until it stabilizes at an almost constant value (e.g., approximately $-1.79$°C at $t = 0.65$ s for $D = 500$ μm) when the entire channel length is covered with dendritic ice. The annular ice layer then becomes visible and grows radially inward (see Figure 4.2 (a)). As the annular ice grows and becomes substantially thicker such that the channel is nearing closure (e.g., at $\sim 3$ s in Figure 4.3 for $D = 500$ μm), the ice begins to lose sensible heat and the

temperature reading starts to drop. The annular ice then continues to grow radially inwards until it fills the entire cross-section at the closure plane. Closure occurs at $t = 3.48$ s for $D = 500$ μm and much sooner at $t = 0.25$ s for $D = 100$ μm. In Figure 4.3, it should be noted that the temperatures measured by the thermocouples, $T_{wall,TC}$, are expected to be lower than the actual external wall temperature during the annular ice growth periods, especially for $D = 300$ μm and 100 μm, as is further discussed in Section 4.2.2.

Figure 4.4 shows a comparison of the channel closing times for all 3 channel diameters. The closing time is measured directly from the high-speed videos, starting from the frame which shows the dendritic ice nucleation to the frame where the annular ice fronts meet and block the channel. For each case, the observed variation in closing time is reported over the 8 repeated experimental trials. The median value of closing time ($t_{cl}$) decreases monotonically with channel diameter, viz., from 3.48 s for $D = 500$ μm to 1.38 s for $D = 300$ μm to 0.25 s for $D = 100$ μm. The minimum closing time is shorter than previously reported values in the literature of 18 s [7] and 4.1 s [22] using a single-stage thermoelectric (TE) module and 2.27 s [20] using a two-stage TE cooling module. The only comparable closing time of 0.37 s was obtained using a large-footprint, multi-stage TE cooling module at a much lower water flow rate of 10 μl/min [23]. This shortest reported closing time of 0.25 s obtained in the smallest 100 μm inner diameter channel is a critical demonstration showing that reducing the channel diameter is a viable and effective method of reducing the channel closing time. For ice valve applications, this approach may be a simpler alternative to introducing new cooling mechanisms or nucleating agents [27,50] to reduce the closing time.

### 4.2.2 Model-Based Analysis of the Role of Channel Diameter on the Annular Ice Growth Time

A simplified flow freezing model was developed in CHAPTER 3 [66] that described the transient annular ice growth process and identified the key factors governing annular ice growth, and therefore, the channel closing time. Utilizing the model, this section analyzes the role of channel diameter in affecting the channel closing time.

In the model described in detail in CHAPTER 3, a channel with an external and an internal radius of $R_{wall,ext}$ and $R_{wall,int}$, respectively, is axially discretized into small control volumes of length $\Delta z$, each encompassing the entire cross-section. Within this control volume, the region occupied by the water is assumed to behave as a lumped mass. The channel external wall temperature, $T_{wall,ext}$, is at a uniform value lower than the equilibrium freezing temperature, $T_f$, along the entire length. Time is discretized in steps of $\Delta t$. An annular ice layer with the interface at $R_i^{i,j}$ (annular layer thickness $= R_{wall,int} - R_i^{i,j}$) and interface temperature $T_i$ exists in a single control volume $i$ at time step $j$. A small mass of water adjacent to the interface freezes and forms a solid ice layer of thickness $\Delta {R_i}^{i,j}$ over a time step $\Delta t$.

For each control volume, the model accounts for mass conservation (between the inlet mass flow, the outlet mass flow, and the mass of water frozen) as well as the energy conservation (between the energy advected along with the water flow, the latent heat released by the freezing mass, and the energy conducted radially outward from the channel) to calculate the location of the annular ice front at each time step. An order-of-magnitude comparison between the different energy terms shows that the annular ice growth is governed by the radial conduction of the released latent heat while the advection term has negligible effect on the freezing process (see APPENDIX A.3)

The details of the modeling assumptions, simplification of the governing equations, and the solution algorithm can be found in Ref. [66]. The resultant expression for annular ice growth in the control volume *i* at time step *j* is given by:

$$\rho_s 2\pi R_i^{i,j} \frac{\Delta {R_i}^{i,j}}{\Delta t} \Delta z L_f \approx -2\pi \Delta z \frac{\left(T_i - T_{wall,ext}\right)}{\frac{\ln\left(R_{wall,int}/R_i^{i,j}\right)}{k_s} + \frac{\ln\left(R_{wall,ext}/R_{wall,int}\right)}{k_{bs}}} \tag{4.1}$$

Equation (3.1) indicates that the growth rate of annular ice is determined by how fast the latent heat released during the freezing process can be conducted radially outward from the channel. An expression for the annular ice growth time ($t_{ann}$) can be obtained by integrating Equation (3.1) with respect to $R_i$ from $R_i = R_{wall,int}$ (at $t = 0$) to $R_i = 0$ (at $t = t_{ann}$).

$$t_{ann} \approx \frac{1}{\left(T_i - T_{wall,ext}\right)} \rho_s 2\pi \Delta z \frac{R_{wall,int}^2}{2} L_f \left(\frac{1}{2k_s} + \frac{\ln\left(R_{wall,ext}/R_{wall,int}\right)}{k_{bs}}\right) \frac{1}{2\pi \Delta z} \tag{4.2}$$

Equation.(4.2) shows that the annular ice growth time is a function of three factors: (1) the driving temperature difference ($T_i - T_{wall,ext}$); (2) the total latent heat released by the freezing mass of water $\left(\rho_s \pi \Delta z R_{wall,int}^2 L_f\right)$; and (3) the effective thermal resistance to radial flow of the released latent heat $\left(\left\{(1/2k_s) + \left[\ln\left(R_{wall,ext}/R_{wall,int}\right)/k_{bs}\right]\right\}/2\pi\Delta z\right)$.

The total latent heat released depends on the total mass of the water to be frozen ($\rho_s \pi \Delta z R_{wall,int}^2$) to attain channel closure, which in turn depends on the square of the channel diameter. The effective radial thermal resistance is a function of the ratio of external to internal diameters of the channel and the thermal conductivities of ice and borosilicate glass. Finally, given the ice-water interface temperature to be at the equilibrium freezing temperature ($T_i = T_f = 0$°C), the radial temperature difference driving heat conduction is then set by the external wall temperature during the annular ice formation. Table 4.1 shows the values of these factors for all 3 channel diameters.

Taking $T_i = 0$°C and substituting $T_{wall,ext}$ with the experimentally measured value $T_{wall,TC}$ in Equation (4.2) would lead to shorter closing times compared to the experimental observations from the high-speed images. As mentioned in Section 4.2.1, the temperature recorded by the thermocouple is expected to be lower than the actual external wall temperature driving the annular closure (i.e., an overestimate of the driving temperature difference). The thermocouple, which is not located directly at the point of initial ice nucleation or closure, reads lower than the actual external wall temperature primarily due to the delayed thermal response. This is particularly true for channels with $D = 300$ μm and 100 μm, which have faster annular ice growth rates and smaller thermal masses, such that a thick annulus of ice forms and the channel begins to lose sensible heat before any change in the thermocouple temperature is recorded. This is exemplified by a very small rise (0.2°C) in the wall thermocouple reading followed by a quick drop for $D = 100$ μm, as shown in Figure 4.3.

To obtain an estimate of the actual external wall temperature driving the annular ice growth from the model, Equation (4.2) can be rearranged as:

$$T_{wall,ext,calc} \approx T_i - \frac{1}{t_{ann}} \rho_s 2\pi\Delta z \frac{R_{wall,int}^2}{2} L_f \left(\frac{1}{2k_s} + \frac{\ln\left(R_{wall,ext}/R_{wall,int}\right)}{k_{bs}}\right) \frac{1}{2\pi\Delta z} \qquad (4.3)$$

On substituting the values of constants and annular ice growth time ($t_{ann}$) from the experiments (see Table 4.1) in Equation (3.3), the external channel wall temperature is calculated as $T_{wall,ext,calc} = -1.69$℃ for $D = 500$ μm, which is close to the experimentally measured external wall thermocouple reading ($T_{wall,TC} = -1.79$℃). For $D = 300$ μm and 100 μm, $T_{wall,ext,calc}$ is calculated to be $-1.57$℃ and $-1.23$ ℃, respectively. Based on these values, the driving temperature difference for $D = 500$ μm is 1.37 times that for $D = 100$ μm, and the thermal resistance to the radial heat flow is the same for both these channel diameters. However, the total latent heat released for $D = 500$ μm is 25 times more than that for $D = 100$ μm, due to the difference in the quantity of water that needs to be frozen to attain channel closure. This implies that for a given flow rate, the total latent heat released, and hence the channel diameter, is indeed the dominating factor that governs the annular closing time.

## 4.3 Conclusions

The freezing of water flowing through glass microchannels ($D = 500$ μm, 300 μm, and 100 μm) is experimentally characterized to understand the effect of the channel diameter on the channel closing times, for potential microfluidic ice valve applications. The following key conclusions are drawn from the present study:

- Flow freezing occurs via the formation and growth of both dendritic and annular modes of ice formation that are observed with all three channel diameters (500 μm, 300 μm, and 100 μm). Freezing initiates as dendritic ice that grows along the channel wall, followed by the formation and growth of annular ice that causes complete flow blockage and ultimate channel closure.
- The closing time is observed to decrease monotonically with a decrease in the channel diameter. An extremely short closing time of only 0.25 s is observed for the 100 μm channel at a flow rate of 0.3 ml/min.
- For a given water flow rate, the annular ice growth rate, and hence the channel closing time, is (1) directly proportional to the amount of total latent heat released during the freezing process (which varies as the square of the channel diameter) and (2) the thermal resistance to the radial conduction of this latent heat, while it is (3) inversely proportional to the temperature difference between the external wall temperature and the ice-water interface which drives the radial conduction of the released latent heat.

- For the investigated channel diameters, a comparison of the magnitudes of all the parameters shows that the total latent heat released by the freezing mass in the channel is the dominant term, which directly controls the annular closing time. The mass of freezing water varies as the square of the channel diameter and, hence, the closing time reduces significantly as the channel diameter is decreased.

The design of ice valves for microfluidic platforms must consider the channel size, the driving temperature difference, and the thermal resistance to heat flow. In CHAPTER 3, it was shown that for a given channel size a faster closure can be achieved by increasing the flow rate, which indirectly increases the driving temperature difference. The current chapter demonstrates that fast closure can also be achieved by reducing the channel diameter, which may offer a simpler approach, especially for microfluidic applications where using high flow rates or operating at very low temperatures to initiate freezing may not be feasible.

**Nomenclature**

| | |
|---|---|
| $D$ | channel inner diameter ($D = 2R$) |
| $k$ | thermal conductivity |
| $l$ | channel length |
| $L$ | latent heat |
| $m$ | mass of water in the channel |
| $R$ | channel inner radius |
| $\Delta R$ | change in radius over a time step |
| $t$ | time |
| $\Delta t$ | time step |
| $T$ | temperature |
| $\Delta T$ | temperature difference |
| $z$ | axial or streamwise position along the channel centerline |
| $\Delta z$ | length of a unit control volume in the axial direction |

## *Greek symbols*

| | |
|---|---|
| $\rho$ | density |

## *Subscripts*

| | |
|---|---|
| $ann$ | annular ice region |
| $bs$ | borosilicate glass |
| $cav$ | test cell cavity |
| $calc$ | calculated |
| $cl$ | closing |
| $den$ | dendritic |
| $exp$ | experimental |
| $ext$ | external |
| $f$ | freezing |
| $i$ | ice-water interface |

$int$ internal

$s$ solid phase (ice)

$TC$ thermocouple reading

*wall* channel wall

## *Superscript*

$i$ index for a unit control volume

$j$ index for time step

Table 4.1. Comparison of the factors affecting the channel closing time for all channel diameters.

| **Parameters** | **Magnitudes** | | |
|---|---|---|---|
| Internal channel radius, $\boldsymbol{R_{wall,int}}$ (μm) | 250 | 150 | 50 |
| External channel radius, $\boldsymbol{R_{wall,ext}}$ (μm) | 350 | 200 | 70 |
| Released latent heat, $\boldsymbol{\rho_s \pi \Delta z R_{wall,int}^2 L_f}$ (J) | $6.01 \times 10^{-4}$ | $2.16 \times 10^{-4}$ | $0.24 \times 10^{-4}$ |
| Thermal resistance, $\left(\frac{1}{2k_s} + \frac{\ln(R_{wall,ext}/R_{wall,int})}{k_{bs}}\right)\frac{1}{2\pi\Delta z}$ (K/W) | $0.85 \times 10^4$ | $0.78 \times 10^4$ | $0.85 \times 10^4$ |
| Experimental annular ice growth time, $\boldsymbol{t_{ann}}$ $(= \boldsymbol{t_{cl} - t_{den}})$ (s) | 3.03 | 1.08 | 0.17 |
| Calculated driving temperature difference, $\boldsymbol{T_i - T_{wall,ext,calc}}$ (℃) | 1.69 | 1.57 | 1.23 |

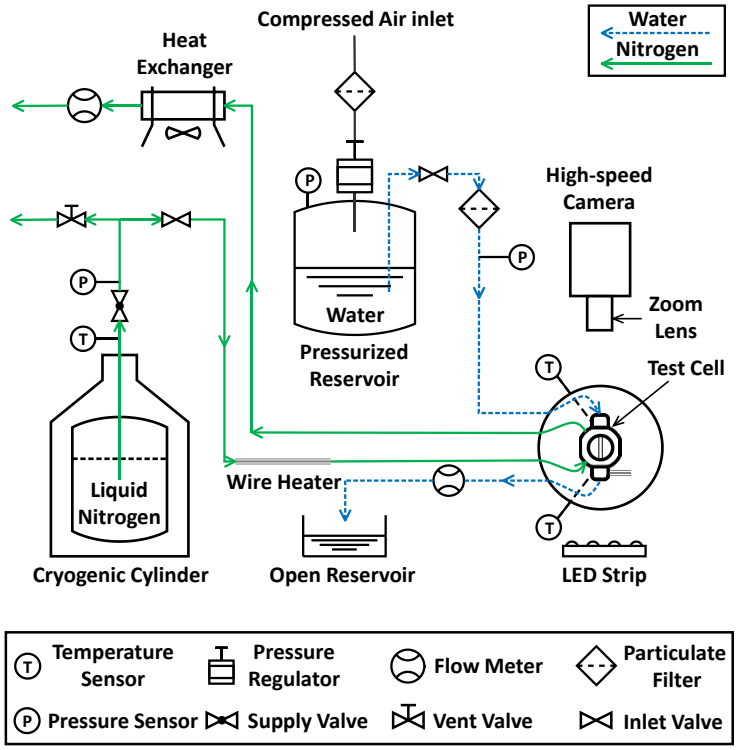


(a)

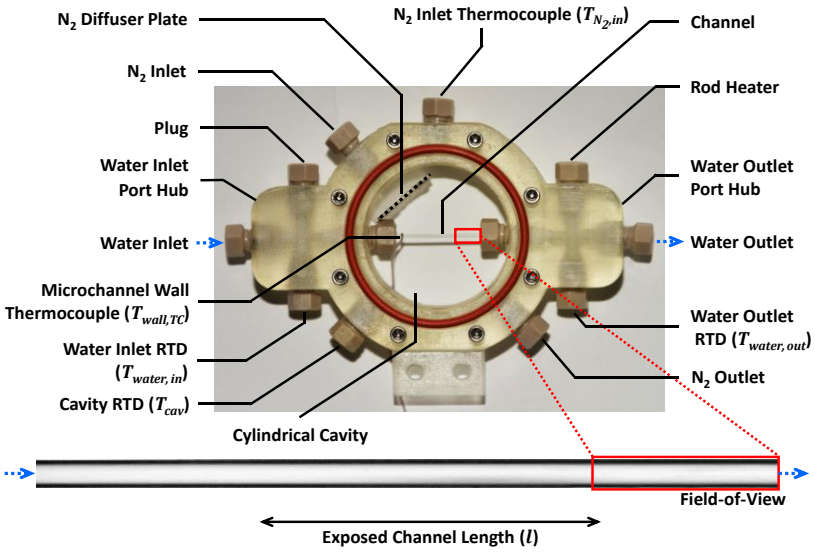


(b)

Figure 4.1. (a) Schematic diagram of the experimental test facility [66], and (b) photograph of the test cell showing the microchannel and ports for measurement instrumentation. Inset shows the exposed channel length and the field-of-view selected for flow visualization.

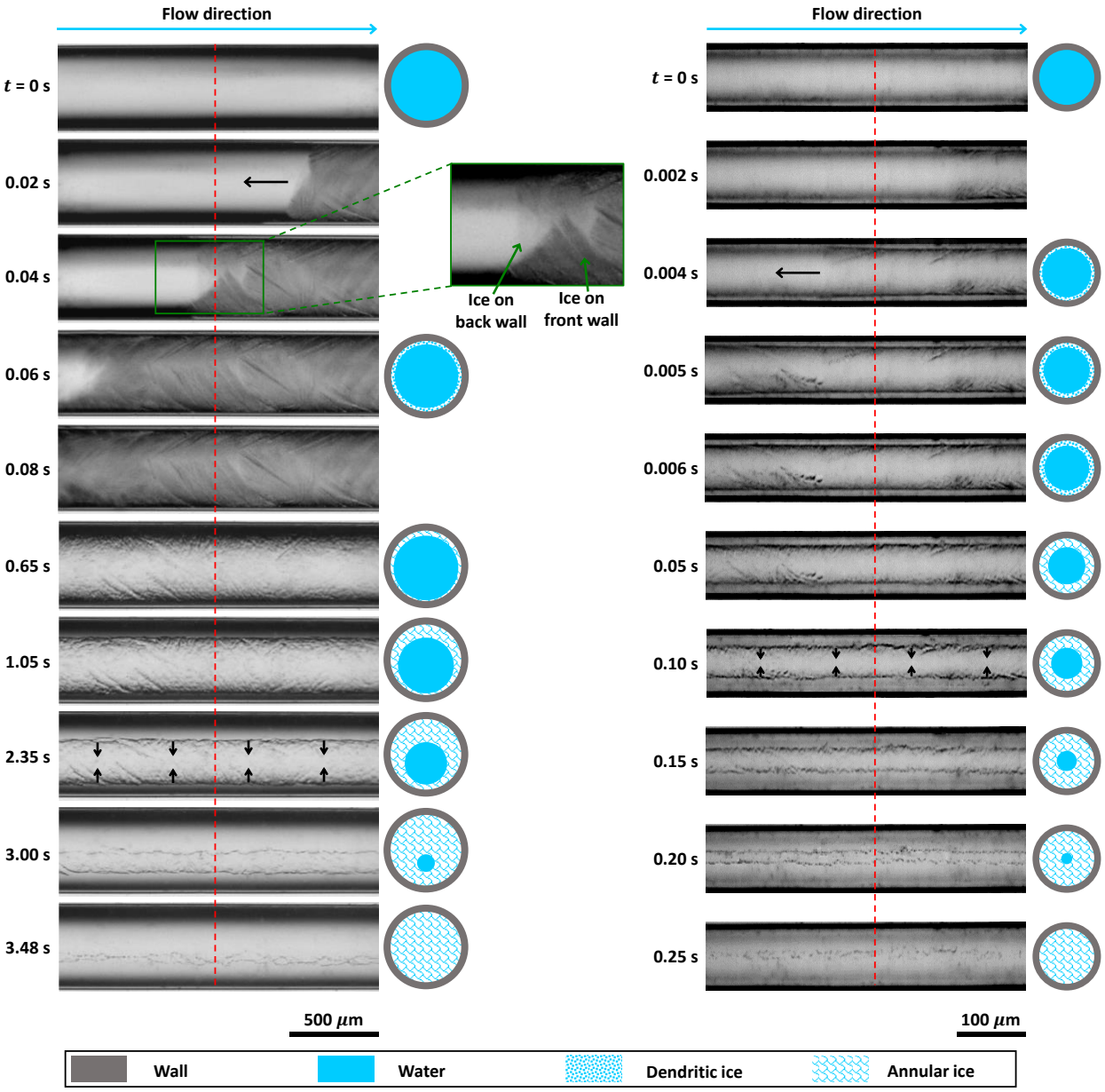


(a) (b)

Figure 4.2. Time sequence of images showing ice formation modes during flow freezing in a microchannel for (a) $D = 500$ μm and (b) $D = 100$ μm. The schematic diagrams to the right of the channels show the channel cross-section at the closure plane (dashed red line). The channel wall, water, dendritic ice, and annular ice regions are shaded as indicated in the legend. Flow direction is from left to right. The black arrows indicate the direction of ice growth. The scale bar for each channel diameter is indicated at the bottom.

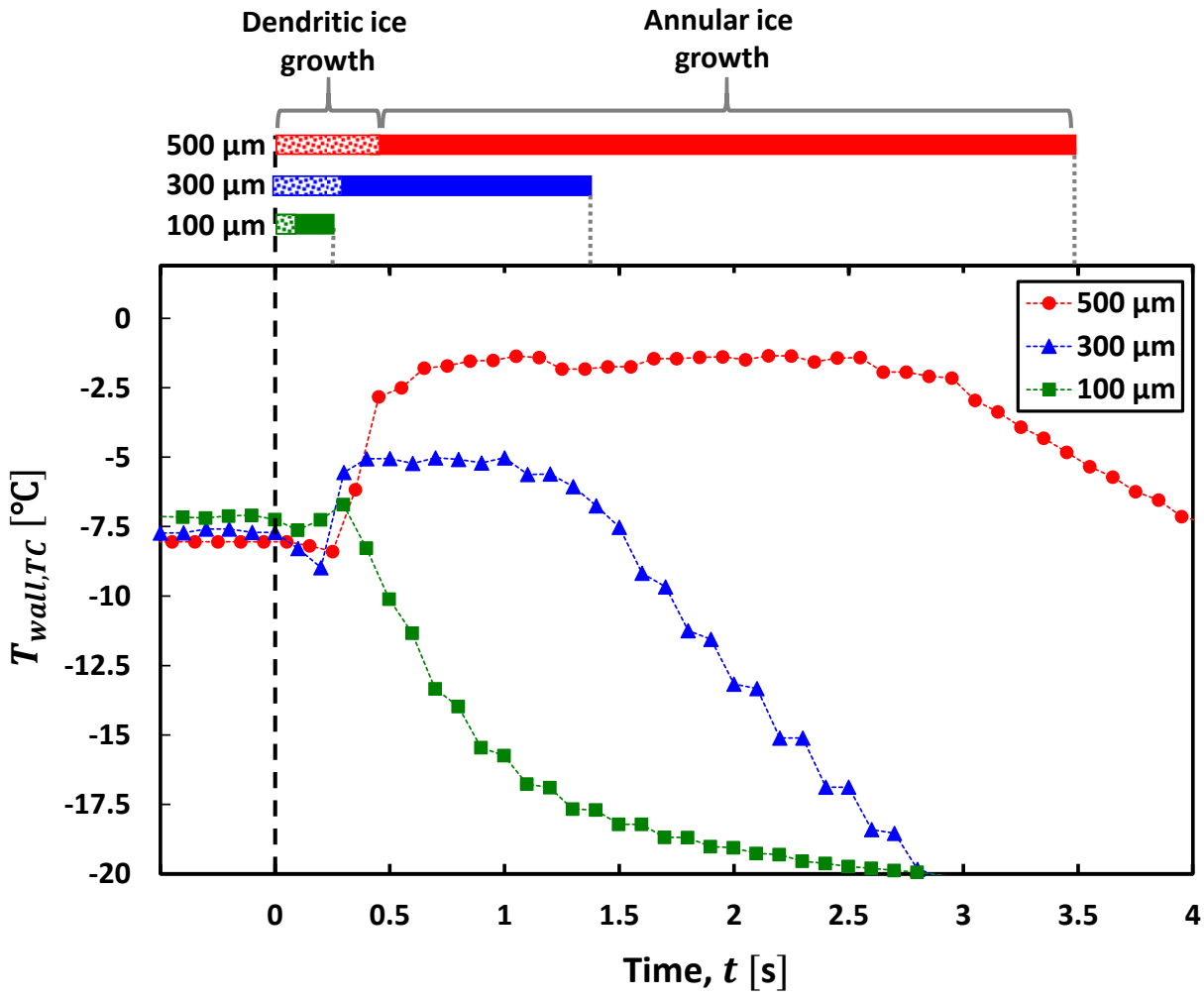


Figure 4.3. Temporal variation of the external channel wall thermocouple readings during the freezing process and beyond for all three channel diameters. The dashed black line represents the appearance of dendritic ice in the visualizations, marking the time of nucleation ($t = 0$ s). The bars on top show a comparison of the growth time of dendritic and annular ice obtained from flow visualization for each case. The dotted lines at the end of each bar represent channel closure.

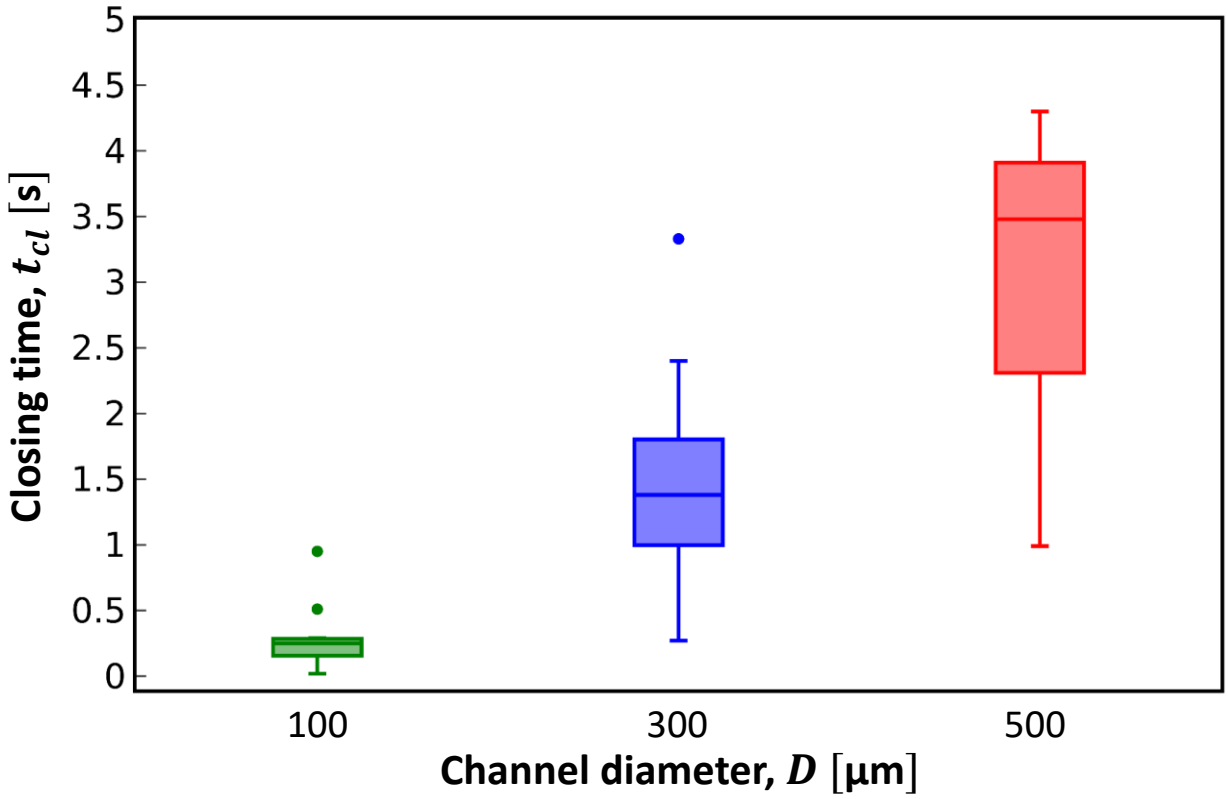


Figure 4.4. Variation of the channel closing time as a function of the channel inner diameter, with variations shown over 8 repeated trials. The boxes span the first to third quartiles, while the horizontal lines inside the box represent the medians. The dots represent statistical outliers.

# CHAPTER 5. ICE VALVE FORMATION MECHANISM FOR MICROFLUIDIC DEVICES

This chapter aims to design and demonstrate a liquid $CO_2$ based ice-valve cooler which is compact enough to be interfaced with complex microfluidic devices and can precisely control the location of ice valve formation in a water flow in a microfluidic channel. The cooler is designed to self-limit the flow of cryogen, reducing wastage. The effect of the flow rate, the channel size, and the chip material on the response time of the ice valve is investigated using high-speed visualization of the freezing process, synchronized with the cooler base temperature and the instant of cooler contact, in four constant-pressure-driven water flow rates ($Q$ =10 µl, 20 µl, 30 µl, and 40 µl) in square cross-section channels of three sizes ($x_{channel}$ = 50 µm, 100 µm, and 200 µm) fabricated on PMMA and glass ($x_{channel}$ = 100 µm only) chips. The pressure tolerance of the formed ice valve is also tested. To develop chip design guidelines, the cooling process of the chip using the proposed cooler design is modeled using both 3-D numerical and simplified 1-D analytical models. The temperature distribution in the chip is used to estimate the values of response times of the ice valve and of the pitch for a multi-channel chip. The nomenclature for this chapter is presented after the chapter text, before the figures.

## 5.1 Experimental Setup and Procedure

### 5.1.1 Test Facility

The experimental setup consists of an open water flow loop and an open carbon dioxide ($CO_2$) flow loop which are connected to a test chip and the cooler, respectively (see Figure 5.1(a)). To briefly summarize the primary functions of the test facility, the cooler is cooled down by the cold $CO_2$ gas and is placed in contact with the test chip. As water flows through a channel fabricated on the test chip, it gets cooled down to the nucleation temperature and the freezing initiates; the freezing process is captured using a high-speed camera placed vertically below the chip. The entire setup, except the cryogenic cylinder, is mounted on a vibration-isolated optical table (VH3648W-OPT, Newport).

A pressurized reservoir is employed to generate the flow in the water loop (dashed blue line in Figure 5.1(a)); the flow is driven by the pressure difference between the reservoir and the ambient. A compressed air source is used to pressurize the reservoir and the pressure is precisely controlled to obtain the desired flow rate using a high-precision servo-controlled pressure regulator (PRG200-25, Omega). An inlet valve is placed downstream of the reservoir to switch the flow on or off. The water pressure is measured downstream of the reservoir using a pressure transducer (PX302-015GV, Omega). The flow rate of the water is measured using a liquid flow meter (LC-5CCM-D, Alicat) downstream of the test chip. Four constant-pressure-driven water flow rates ($Q$ =10 µl, 20 µl, 30 µl, and 40 µl) are tested. Water flowing out of the test chip is collected in an open reservoir.

The $CO_2$ is delivered to the open-loop system (solid green line in Figure 5.1(a)) using a constant-pressure cryogenic cylinder. A pressure gauge is installed to measure the cylinder pressure. The flow is turned on or off using the inlet valve. A supply valve is used to control the flow rate and the downstream pressure of the $CO_2$. Pressure and temperature of the flowing $CO_2$ are measured both upstream and downstream of the supply valve using pressure transducers (0-4000 kPa; 4000K222, McMaster-Carr Supply Co.) and thermocouples (TJ36-CPIN-11G-12, Omega; ± 1°C), respectively. A relief valve (PR-600, Ratermann) is installed between the inlet and the switch valves to prevent over-pressurization of the cylinder.

The test chip (Figure 5.2) is a pre-fabricated, transparent microfluidic chip that consists of two halves fused together. The square cross-section microchannel is fabricated on the lower half or the base and the inlet and the outlet ports are machined on the top half or the cover. The chip is mounted horizontally on a holder specially designed with a gap in the center to enable visualization and a clamp on each end to hold the chip in place, as shown in Figure 5.1(b). The inlet and outlet ports are connected to the flow loop using flexible tubing (ID 0.76 mm; 29-0610-0000-08, microfluidic ChipShop GmbH) and high-pressure leak-proof luer fittings to prevent water leakage. Absolute pressure transducers are installed right upstream (0 – 207 kPa; Transmitter S-10, Wika) and downstream (0 – 69 kPa; Transmitter S-10, Wika) of the chip (not shown in the figure).

This study uses chips made of two materials with different thermal diffusivities, Polymethyl methacrylate (PMMA) and fused silica glass. Three channel widths, $x_{channel}$, of 200, 100, and 50 μm on the PMMA chip (02-0752-0201-01, 02-0756-0166-01, and 02-0773-0394-01, respectively, microfluidic ChipShop GmbH) and a single channel of width, $x_{channel}$, 100 μm on the glass chip (SC-BU-100100-L,Translume Inc.) are tested in this study. The details of the chip and channel dimensions for each chip type is provided in the Table 5.1.

The freezing process is captured using a high-speed camera (VEO 710L, Phantom) fitted with a long-working-distance high-magnification zoom lens (VHZ100L, Keyence). The channel is front-lit using a high-intensity Xenon lamp (Titan X300, Sunoptics Technologies). The camera and the lens assembly is mounted on a three-axis traversing stage, placed vertically below the test section in-line with the cooler. Different levels of magnification are needed for each channel size. The lens is focused on the bottom of the channel and corresponding field-of-view, as marked in Figure 5.1(c), is chosen upstream of the cooler (4 mm from the center of the cooler contact region) to avoid hinderances in visualization due to frost formation on the chip's bottom surface directly underneath the cooler and on the channel downstream of the cooler (due to cold water). The images are acquired at 5,000 fps with an exposure time of 200 μs and a visualization window of 1280×200 pixels. This window size corresponds to an optical resolution of 3.8 μm/pixel (optical zoom of 5.36×), 1.9 μm/pixel (10.72×), and 0.9 μm/pixel (22.63×) for channel widths, $x_{channel} =$ 200 μm, 100 μm, and 50 μm, respectively. The camera is synchronized with the other readings using a pulse generator (Model 565-8C-H, Berkeley Nucleonics Corporation). All the data is recorded at a sampling frequency of 100 Hz using a high-frequency data acquisition system (cDAQ-9178, National Instruments) through a LabVIEW interface.

### 5.1.2 Cooler Design

The cooler is a custom-designed component which functions as an expansion device for the inflowing liquid $CO_2$, as shown in Figure 5.3. The liquid $CO_2$ enters the cooler through a copper tube (OD = 3.175 mm and ID = 1.67 mm) soldered at the top. The cooler body is made of brass cylinder (OD $= 2r_c =$ 7.94 mm) with a copper plug is soldered at the bottom of the expansion chamber to serve as conductive contact between the cooler and the test chip. Directly above the copper plug, 10 identical exit holes (ID = 0.7 mm) are drilled on the cooler wall for $CO_2$ exit. A

36-gauge T-type thermocouple (5TC-TT-T-36-36, Omega; ± 1°C), that is fit into the hole drilled in the copper base, is used to measure the cooler temperature. A custom designed plastic sheath (not shown in the figure) is fit around the cooler, leaving the base open for contact, to ensure that all the $CO_2$ is vented up and not on the chip. The cooler is mounted on a vertical stage that can be moved to place the cooler in contact with the chip.

The inlet diameter is so chosen that the inlet allows for enough mass flow rate of $CO_2$ for complete cooling of the largest channel ($x_{channel} = 200$ μm) with highest water flow rate (40 μl/min) from ambient temperature to the nucleation temperature ($T_{nuc}$). The diameter of the expansion chamber is calculated such that the pressure of $CO_2$ after expansion, and taking expansion pressure losses into account, is equal to the triple point pressure of $CO_2$ (526.89 kPa). Additionally, since the $CO_2$ exits the cooler at ambient pressure, the diameter of the exit holes are chosen so that the net throttling and compression pressure loss across it is equal to the difference between the triple point pressure of $CO_2$ and the ambient pressure (101.325 kPa).

### 5.1.3 Test Procedure

To start the test, the flow is started in the water flow loop by pressurizing the reservoir; the reservoir pressure is adjusted to generate a constant pressure driven flow based on the channel width and the desired flow rate. The camera and lens assembly is moved such that the channel base is in focus. The $CO_2$ flow to the cooler is then initiated by turning on the inlet valve. The $CO_2$ then enters the supply valve as a subcooled liquid. As it passes through the valve, it undergoes an isenthalpic expansion process. This process reduces the pressure and the temperature of the $CO_2$ and causes it to partially evaporate. The supply valve is adjusted such that the downstream $CO_2$ pressure transducer reads 100 psi (698.5 kPa). The cold liquid-gas mixture from the valve is allowed to flow through the expansion chamber, where it undergoes free expansion followed by throttling as it exits through the exit holes to the ambient, until dry ice (solidified $CO_2$) forms and blocks the $CO_2$ flow through of the cooler.

Once the dry ice blocks the cooler, the cooler is moved vertically downward gently, using the vertical stage, until it contacts the chip. The image of the channel is monitored to ensure that cooler only touches the chip without pressing on or bending it. A binary switch is turned on

manually on the LabVIEW interface to mark the instant of cooler contact. The cooler is kept in contact with the chip until the nucleation is observed in the channel. The freezing process is captured using the high-speed camera and the zoom lens. Multiple trials are performed for each channel size and chip material by repeating the same test procedure. Data are acquired for 6 repeated runs for each case.

## 5.2 Results and Discussion

The results from the cooler design tests are presented in this section; a novel design for a stand-alone cooler is tested to verify that the cooler functions as designed, and its working is demonstrated. The ice valve formation in the test chips for various flow rates, channel sizes, and chip materials is also presented, including their effect on the channel base temperature and the observed response times. The flow freezing process of water in the microchannel is visualized and the response times of the channel at different flow rates and channel widths are measured. The pressure tolerance of the formed ice-valves in the microchannel is also tested. Furthermore, with an objective of developing the chip design guidelines for use with the proposed cooler design, the cooling of the chip is modeled using a 3-D numerical and simplified 1-D conduction-based models. The models estimate the response time of the valve and the pitch of the channels, based on the temporal and spatial temperature distribution in the chip, for a microfluidic chip design.

### 5.2.1 Cooler Design Tests

To ensure that the throttling process works as expected to make the cooler design feasible, experiments are performed only with the $CO_2$ flow loop. In addition to the cooler base temperature sensor, a temperature sensor (5TC-TT-T-36-36, Omega; ± 1°C) is installed through one of cooler holes to measure the chamber temperature. Figure 5.4 shows the values of pressure and enthalpy at locations upstream of the cooler, inside the expansion chamber and outside the holes on the $CO_2$ pressure-enthalpy diagram, before and after the dry ice forms for 7 repeated trials.

As the inlet valve at the cryogenic cylinder is opened, the $CO_2$ starts flowing into the expansion chamber of the cooler as a liquid-gas mixture; it absorbs heat from the cooler body while undergoing free expansion to completely gaseous state. The gaseous $CO_2$ then undergoes throttling as it exits through the exit holes to the ambient (see solid circles on Figure 5.4). Once

the cooler body cools down and reaches a temperature of ~ −56.4°C, the cooler cannot provide enough heat to evaporate the liquid-gas $CO_2$ mixture completely before it exits the cooler. Thus, at the low temperatures, as this liquid-gas mixture undergoes throttling process at the exit holes, the mixture cools down below the sublimation temperature and sublimates into dry ice, blocking the exit holes (solid triangles on Figure 5.4). This blockage prevents further inflow of $CO_2$ into the cooler. At this point, the cooler base temperature goes below the triple point of $CO_2$ (−56.4°C at 517.8 kPa) and remains constant throughout the test. The $CO_2$ flow can be restarted by letting the dry ice thaw. This verification test provides the proof of concept for the design of the cooler that can self-limit the $CO_2$ flow when cooling is not required. The key benefit of this design is that this process reduces the waste of cryogen while also ensuring an isothermal cooler base temperature, $T_{coolerbase}$, of ~ −74°C during the tests.

### 5.2.2 Visualization of the Freezing Process

The visualization tests are performed according to test procedure described in Section 5.1.3. As the cold cooler is brought in contact with the chip ($t = 0$), the chip and the water flowing in the channel start to lose heat. Freezing initiates in the cooler at the time when the temperature at the channel wall reaches the nucleation temperature. The freezing process is captured using a high-speed camera placed vertically below the chip. Response time ($t_{res}$) is defined as the time between the instant at which the chip cooling is started and the instant at which dendritic ice is observed in the field-of-view.

Figure 5.5 shows a time sequence of the images from the high-speed visualization as freezing initiates and progresses for a representative case of PMMA chip with 200 μm channel size and water flow rate of 20 μl/min. The images show that the freezing process initiates with dendritic ice formation on the channel wall which quickly covers the entire visible channel length ($t - t_{res} = 28$ ms), followed by slow inward growth of the annular ice which leads to complete channel closure ($t_{cl,observed} = t - t_{res} = 364$ ms). Similar behavior is observed for all flow rates, channel sizes and chip material. This behavior is also consistent with the freezing process observed in CHAPTER 3 and CHAPTER 4 [66,71,73] for cylindrical borosilicate microchannels (ID = 100 μm to 500 μm).

The annular closure front observed in the high-speed visualization serves as confirmation of the ice-valve formation. However, it should be noted here that since the frost formation hinders visualization, the field-of-view is located 4 mm upstream from the center of cooler contact region (as mentioned in Section 5.1.1). But, since the annular front must close first where the channel is coldest, i.e., on the top wall of the channel in the center of the cooler contact region , the upstream field-of-view does not capture the annular closure front as forms at the actual point of closure. Therefore, it is difficult to calculate the actual closing time ($t_{cl,actual}$) of the channel.

### 5.2.3 Effect of Water Flow Rate, Channel Size, and Chip Material on Cooler Base Temperature and Response Time

Figure 5.6 shows the cooler base temperature ($T_{coolerbase}$) at the instant at which dendritic ice is observed in the field-of-view for all tested flow rates, channel sizes, and chip materials, repeated over 6 trials for each case. As is consistent with the design of the cooler, the cooler base temperature remains at a constant average value of ~−74°Cand does not vary with the water flow rate, the channel size or the chip material.

As mentioned in Section 5.2.3, response time ($t_{res}$) is defined as the time between the instant at which the cooler is placed in contact with the chip ($t = 0$) and the instant at which dendritic ice is observed in the field-of-view. Because the dendritic ice front moves at much faster speed compared to the annular closure front, the effect of the location of the field-of-view on the response time calculations can assumed to be negligible. Thus, the response time can also be defined as the time taken for any point on the channel to reach the nucleation temperature ($T_{nuc}$) from the instant of cooler contact.

Figure 5.7 shows the response time ($t_{res}$) for all tested flow rates, channel sizes and chip materials. The response times for a given chip material are independent of the water flow rate or the channel size. Since the cooling of the chip underneath the cooler is conduction driven, the heat transfer across the chip can be modeled using 1-D thermal resistance network, as discussed in APPENDIX C. The analysis shows that, as the cooled area of the channel ($2r_c x_{channel}$) is much smaller compared to the area of the cooled region of the chip ($\pi r_c^2 - 2r_c x_{channel}$), the resistance of the chip is negligible compared to the channel; most of the heat flows through the chip and the effect

of the channel is, therefore, negligible. Furthermore, the rate of conduction of heat in the given chip for same cooler base ($T_{coolerbase}$) and ambient ($T_\infty$) temperatures is dependent only on the thermal conductivity of the chip material. Therefore, the time taken for the channel top to reach the nucleation temperature ($T_{nuc}$), i.e., $t_{res}$, should reduce with increase in the material's conductivity as seen in Figure 5.7. The average response time for the PMMA chips ($k_{chip} = 0.15$ W/mK) is 39.25 s, compared to 7.5 s for the glass chip ($k_{chip} = 1$ W/mK).

It should also be noted at this point that the average response time ($t_{res} = 7.5$ s and 39.25 s) is at least an order of magnitude longer than the observed closing time ($t_{cl,observed} = 364$ s) of the channel and, hence, is the limiting time in the process. Therefore, it is crucial to estimate the response time for proper design of an ice valve. Consequently, one of the objectives of the models to analyze the chip cooling process is to develop the chip design guidelines by estimating the response time, as would be described in Section 5.2.5.

### 5.2.4 Pressure Tolerance of the Ice Valve

To test the pressure tolerance of the formed valve, the air pressure in the water reservoir is carefully increased in steps of 2.5 psi (17.24 kPa) from a starting pressure of 5 psi −12 psi (34.47 kPa− 82.74 kPa) (depending on the channel size and the flow rate) using the pressure regulator while waiting at each step for 120 s, until the valve or the test setup can tolerate the pressure.

The process is performed with the cooler both in contact and out of contact with the chip for multiple times. It is observed that in either case, the ice valve and the test setup can tolerate a maximum pressure of 25 psi (172.37 kPa). Beyond this pressure, the fittings start to leak but the valve remains intact. Additionally, when the cooler is not in contact, it is observed in some cases that the ice plug melts away rather than dislodges if kept for a longer duration, irrespective of the pressure below 25 psi (172.37 kPa). Therefore, for a leak-free functioning of the ice valve, thawing could be a greater concern than the high pressure.

It should also be noted here that although the maximum tolerated pressures by the ice valve and test setup are much lower than those required for high-pressure applications, like HPLC (up to 40 mPa; see Section 2.4), the points of leakage are the connectors and not the ice valve for these tests.

In a practical system, the connectors and the entire flow loop would be much more integrated and have higher pressure rating, and, therefore, the system would be less susceptible to leaks.

### 5.2.5 Model for the Chip Cooling Process

As can be concluded from the experimental observations in the Sections 5.2.2 and 5.2.3, the response time is the rate limiting parameter in functioning of the ice valve. To provide guidelines for chip design where the proposed cooling mechanism can be used to form ice valves, it is crucial to be able to predict the response time of the ice valve. Additionally, for designing multi-channel chips, it is important to know the minimum channel to channel distance (pitch) to use with this channel design for proper functioning of the device. Therefore, in this section, two models - 3-D numerical and 1-D analytical - are developed to analyze the cooling process of the chip by the proposed cooler design. The temporal and spatial temperature distributions in the chip predicted by the models are used to calculate of the response time of the ice valve formation and of the pitch of channels for a multi-channel chip. The models account for the conduction in the chip as well as the convection in the channel and in the ambient. The numerical and analytical models are solved using ANSYS Fluent and Python, respectively.

#### 5.2.5.1 Numerical model

The computational domain for numerical model is shown in Figure 5.8 along with the boundary conditions. The chip dimensions are same as the PMMA test chip (see Table 5.1) and are marked in the figure. The cooler contact region is assumed at a constant uniform temperature, $T_s$, throughout the test. The lateral walls and uncooled region of chip top are insulated. The chip base is subjected to a convective boundary condition at the ambient temperature, $T_\infty$ with a constant convective heat transfer coefficient, $h$. $T_s$ and $h$ are estimated using a 1-D thermal resistance network analysis such that the experimental data match the model predictions, as discussed in APPENDIX C.

Since the response time depends on the rate of heat conduction, the location of the channel (and the cover thickness, $x_{cover}$) would affect the calculations. For the analysis of effect of cover thickness, three values of cover thicknesses, $x_{cover}$ = 100 µm, 175 µm, and 250 µm, are used in the model, while the total chip thickness is kept the same. To study the effect of chip material,

three different materials, PMMA, glass and Silicon are used in the models. Table 5.2 enlists the values of the properties of these materials used in the model.

The following assumptions and simplifications are used in the model formulation:

- The fluid has a well-defined, constant nucleation temperature, which is independent of chip material, flow rate, and surface roughness.
- The model does simulate the freezing process; for calculation purposed, freezing is assumed to initiate at the nucleation temperature
- The contact resistance between the cooler and the chip is only dependent on the chip material and is determined semi-empirically; thus, all the cases are run with same values of heat transfer coefficient ($h = 9.7$ W/mK) and cooler contact region temperature ($T_s = -31$°C).
- The channel size and the flow rate effects can be neglected in the calculations, for reasons discussed in APPENDIX C.
- Same chip dimensions are used for all the test cases.

The cooling process is simulated using the in-built transient energy transfer model on the ANSYS Fluent, for the given boundary conditions until a steady state is reached. The numerical model is validated against the experiments as discussed in APPENDIX C. The response time and the pitch calculations are discussed in the Sections 5.2.5.3 and 5.2.5.4, along with the analytical results.

#### 5.2.5.2 Analytical model

While numerical model can be solely used to analyze the cooling process of the chip, the purpose of analytical model is to provide a simple analytical alternative to the numerical model for calculation of the response time and the pitch for more accessible chip design guidelines. The computational domain for numerical model is shown in Figure 5.9 along with the boundary conditions. The chip dimensions and materials are same as those used for the numerical model.

The analytical model is separated into a simple 1-D model each for the response time and the pitch calculations, depending on the dominant or significant direction of heat transfer for the time scales at which those parameters are calculated, as discussed in the next two sections. Consequently, the model geometry is simplified to limit the calculations to the independent regions of interest

specific to the response time and the pitch calculations, respectively (see Figure 5.9(a) and (b)). For further simplicity, for the reasons described in APPENDIX C, the channel is neglected in the geometry.

*5.2.5.2.1 Analytical response time model*

Since the response time calculations are governed by axial conduction across the cover thickness, along the center of the cooler contact region, the region of interest is limited to the central axis of the chip ($x = 0\ to\ H, y = 0, z = 0$) for response time calculations (Figure 5.9(b)). Furthermore, the time constant of the axial heat transfer is much shorter than that for the radial heat transfer ($\frac{H^2}{\alpha} \ll \frac{W^2}{4\alpha}$). Therefore, the lateral conduction from the cold spot can be neglected for the short, transient time scales at which the response time is calculated.

The transient 1-D conduction heat transfer equation along the central axis of the chip can be written as:

$$\frac{d^2T(x,t)}{dx^2} = \frac{1}{\alpha}\frac{dT}{dt} \tag{5.1}$$

with the following boundary conditions:

At $x = 0$

$$T(0,t) = T_s \tag{5.2}$$

At $x = H$

$$\frac{dT(x=H,t)}{dt} = -\frac{h}{k}(T(x=H,t) - T_\infty) \tag{5.3}$$

And the initial condition at $t = 0$:

$$T(x, t=0) = T_i \tag{5.4}$$

where $\alpha$ is the thermal diffusivity and $k$ is the thermal conductivity of the chip material. $h$ is the convective heat transfer coefficient and $T_s$ is temperature of the cooler contact region estimated by process described in APPENDIX C. Solving Equation $(5.1)$ for the given conditions using separation of variables gives the solution as:

$$T(x,t) = T_s - \frac{(T_s - T_\infty)\frac{h}{k}}{\left(1 + \frac{hH}{k}\right)}x + \sum_{n=1}^{\infty} C_n \sin(\lambda_n x)\exp(-\lambda_n^2 \alpha t) \tag{5.5}$$

where

$$C_n = \frac{\int_{x=0}^{H}\left[T_i - T_s + \frac{(T_s - T_\infty)h}{\left(1+\frac{hH}{k}\right)k}x\right]\sin(\lambda_n x)dx}{\int_{x=0}^{H}\sin^2(\lambda_n x)dx} \tag{5.6}$$

and $\lambda_n H$ is the n[th] root of the transcendental equation:

$$\lambda_n H cot(\lambda_n H) = -\frac{hH}{k} \tag{5.7}$$

*5.2.5.2.2 Analytical pitch model*

For simplification of the geometry, the region of interest for the pitch calculations is limited to the annular region around the cooler up to a radial distance of $r_{W/2}(= W/2)$ (Figure 5.9(c)). Furthermore, since the axial Biot number, $Bi_x$ $(= hH/k_{PMMA} = 0.1)$, is much smaller compared to the radial Biot number, $Bi_r$ $(= hW/2k_{PMMA} = 0.5)$, of the chip, the temperature variation in the axial direction can be ignored at steady-state using semi-lumped body assumption. Thus, the temperature distribution is solved for assuming the region of interest to be annular fin around a cylindrical core of radius $r_c$ and constant temperature $T_s$, with convection on the lateral surfaces with a convection heat transfer coefficient, $h$. All the calculations are done at steady state.

The steady-state, 1-D conduction heat transfer equation in for the annular fin with convection on the lateral surface can be written as:

$$\frac{d^2T(r)}{dr^2} + \frac{1}{r}\frac{dT(r)}{dr} - \frac{2h}{kH}(T(r) - T_\infty) = 0 \tag{5.8}$$

for $r_c \leq r \leq r_{W/2}$. The boundary conditions can be written as:

At $r = r_c$

$$T(r = r_c) = T_s \tag{5.9}$$

At $r = r_{W/2}$

$$\frac{dT\left(r = r_{W/2}\right)}{dr} = 0 \tag{5.10}$$

Solving Equation (5.8) with Equations (5.9) and (5.10) gives the radial temperature distribution in the region of interest at steady state:

$$T(r,\ t \to \infty) = \frac{(T_s - T_\infty)}{I_0(mr_c) + \frac{K_0(mr_c)}{A}} I_0(mr) + \frac{(T_s - T_\infty)}{AI_0(mr_c) + K_0(mr_c)} K_0(mr) \tag{5.11}$$

where

$$A = \frac{K_1(mr_{W/2})}{I_1(mr_{W/2})} \tag{5.12}$$

and

$$m^2 = \frac{2h}{kH} \tag{5.13}$$

$I_0$ and $K_0$ are the modified Bessel functions of first and second kind, respectively, and $I_1$ and $K_1$ are their first order derivatives.

#### 5.2.5.3 Response time calculations

In the numerical model, the response time ($t_{res}$) is defined as the time taken for the bottom of the cover, at the center of cooler contact region, to reach the nucleation temperature, i.e., $T(x = x_{cover}, y = 0, t = t_{res}) = T_{nuc}$. While in the analytical model, the response time is calculated such that $T(x = x_{cover}, t = t_{res}) = T_{nuc}$ in the solution of Equation $(5.5)$ for $x = x_{cover}$. Since the nucleation temperature in a freezing process can be highly stochastic and was not possible to measure experimentally in the presented test facility without affecting the nucleation, a value of –28°C is assumed to be the nucleation temperature for the model calculations for response time as well as pitch for all the cases. This value is chosen, firstly, because it is reasonable for heterogeneous nucleation temperature for very small volume of water (0.079 µl — 0.317 µl under the cooled region) in channels fabricated on hydrophobic materials, both of which conditions can substantially suppress nucleation at lower degree of supercooling [74–76]. Furthermore, heterogenous nucleation is observed to occur quite commonly at temperatures lower than –28°C even for non-hydrophobic substrates and larger volumes of water [77]. Secondly, the choice of this value of nucleation temperature results in the calculated response times which are a good match with the experimental observations.

Table 5.3 lists the response times for all cover thickness and chip materials calculated by the numerical and analytical models, as well as the median response time for each chip from the experiments for $T_{nuc} = –28$°C; the values are in good agreement with each other and with the

experimental results. Since the temperature at the base of cover plate and, hence, the response time are governed by the conduction of heat across the cover plate, reducing the thermal resistance to the heat flow across the cover plate reduces the response time. Thus, it reduces with increasing the conductivity of the material (see Table 5.2) as well as with reducing the thickness of the cover plate from 250 μm to 100 μm. These results show that the response time of the valve for any chip material and dimensions can be simply calculated using 1-D conduction model with good accuracy; this is a crucial step in determining the efficiency of a chip design. Further, to reduce the response time of the chip, a thinner cover plate fabricated with higher thermal conductivity material should be used.

#### 5.2.5.4 Pitch calculations

In the numerical model, the pitch of the channels is defined as the minimum normal distance from the cooled channel axis at which other channel can be placed such that it remains unfrozen at the steady state, i.e., $T\left(x = x_{cover}, y = y_{pitch}, t \to \infty\right) = T_{nuc}$. In the analytical model, to calculate the pitch, Equation (5.11) is solved and the value of pitch is obtained graphically, such that, $T\left(r_{pitch}\right) = T_{nuc}$. Figure 5.10 shows the variation of temperature along the normal distance from the cooled channel axis for all chip materials, calculated using the numerical (for $x_{cover} = 175$ μm) and the analytical models. Table 5.4 lists the pitches for all cover thickness and chip materials calculated by both the analytical and the numerical models for $T_{nuc} = -28$°C. The analytical model overpredicts the pitch compared to the numerical model. From a practical point of view, it is safer to overpredict the pitch for chip design if the intention is to prevent unintentional freezing in adjacent channels. Thus, the 1-D model can be used to get a conservative estimate of the pitch for a given chip material and thickness.

Since the temperature distribution on the base of cover plate and the pitch are governed by the conduction of heat across as well as along the cover plate, reducing the thermal resistance to the heat flow across the cover plate increases the pitch. Thus, while it increases with increasing the conductivity of the material for a given value of $x_{cover}$, reducing the value of cover plate thickness (i.e., reducing the area for heat transfer from the cooler contact region to the lateral pitch distance) reduces the pitch. Therefore, to increase the channel density for multichannel devices, a low conductivity substrate with a thinner cover plate should be used. Since low conductivity of the

substrate could also increase the response time, the chip designer would need to use an optimum conductivity material. Additionally, in addition to the chip material, the temperature distribution and, hence, the pitch is largely dependent on the size of the cooler used (Equation 5.11); using smaller the cooler footprint would allow for higher channel density on a chip.

#### 5.2.5.5 Experimental verification of pitch calculations

To verify the pitch calculations, a new set of experiments is performed with a PMMA chip (01-0172-0156-01, microfluidic ChipShop GmbH) with four parallel channels of square cross-section, size of 200 μm, and a pitch of 4.5 mm (see Figure 5.11(a)). The experiments are performed using only the middle two channels; other channels are sealed using mini-luer plugs. The water flow path to the chip is split into two for separate channel inlets. The cooler is allowed to cool down until dry ice shuts off the holes. Flow is then initiated in the two channels at a total flow rate of 20 μl/min. The cooler is then brought into contact with the chip such that only one middle channel passes under it (see Figure 5.11(b)). The field-of-view is first set 4 mm upstream of the cooled channel from the center of the cooler contact region to verify the occurrence of freezing. The field-of-view is then set at center of the channel parallel to the cooled channel, as shown in the Figure 5.11(b), using optical stages and observation is made till steady state.

Figure 5.12 shows time sequence of images from high-speed visualizations of both the channels at same time intervals from the instant of cooler contact. The pressure drop data across both the channels is used to verify that cooled channel freezes. It is observed that the uncooled channel, which is located at a pitch distance greater than estimated pitch distance from either model, does not freeze even at the steady state. Thus, this test verifies the pitch calculations using both numerical and analytical pitch models. Additionally, this test also demonstrates that the cooler is capable of creating localized cold spots.

In summary, the analytical models, the numerical model, and the experiments could all be used to get estimates of the response time and the pitch calculations depending on the stage of chip design. For the preliminary design phase, the analytical models provide a simple and more accessible alternative to numerical model; those parameters can be estimated using mathematical equations

without having to simulate the entire chip geometry, with reasonable accuracy. For the intermediate design stage, the numerical model would provide more accurate estimations, because of the use of less restrictive approximations in simulations, but the complexity and cost of solution would increase. Finally, at the prototype stage of the design, an experiment could be designed, and the response times and the pitch could be measured for exact values.

While analytical models are the easiest option to implement, it should be noted that the they use certain assumptions which need to be met to simplify the geometry for calculations: chip thickness ($H$) $<<$ chip half width ($W/2$), for the axial time constant to be lower than lateral time constant for response time calculations as well as for the axial Biot number to be smaller than lateral Biot number for pitch calculations. Additionally, a suitable material (thermal conductivity $k$) and chip thickness needs to be chosen such that the axial Biot number, $Bi_x$ $(hH/k) < 0.1$ for using semi-lumped body analysis.

Additionally, to get an estimate of the response time and the pitch for a given cooler radius ($r_c$) and chip material and chip thickness, Equations 5.5 and 5.11 need to be calculated by substituting the parameters from boundary and initial conditions, i.e., cold spot temperature ($T_s$), convective heat transfer coefficient ($h$) and ambient temperature ($T_\infty$). For this study, these parameters where measured and calculated based on experimental observations. To make the calculations easier for the end user, following recommendations can be made for the acceptable range of these parameters: the value of $h$ can be assumed to be in the suitable range for natural convection (5 W/m$^2$K – 30 W/m$^2$K), $T_\infty$ can be assumed to be in the range of 22°C – 25°C and $T_s$ can be assumed to be between -25°C – -35°C. $T_s$ can also be calculated using the resistance network analysis (APPENDIX C) if the contact resistance value between the cooler base and the chip substrate is known, for a better estimate.

## 5.3 Conclusions

A novel design for a cryogen-based cooling mechanism, suitable for microfluidic applications, is proposed and demonstrated. Valve formation is studied in square microchannels of various water flow rate, channel sizes, and chip materials, including their effect on the response time of the ice valve. Furthermore, the cooling of the chip is modeled using a 3-D numerical and simplified 1-D

conduction-based models. The models estimate the response time of the valve and the pitch of the channels, based on the temporal and spatial temperature distribution in the chip, for a microfluidic chip design. The following are the key conclusions from the study:

- The design of cooling mechanism helps limit the cryogen usage, due to blockage of the exit holes by dry ice which forms as result of expansion of liquid-gas $CO_2$ mixture in the expansion chamber.
- The cooler is capable of forming ice valve by creating localized, constant temperature cold spots, which can be interfaced with multi-channel chips without causing unintentional freezing.
- Response time is the rate limiting time for the valve operation; it is governed by the 1-D conduction of heat in the cooler contact region from the channel top to the cooler and does not show any trend with the channel size or the flow rate. However, it reduces with increasing the conductivity of the chip material.
- The ice valve has a stand-off pressure larger than 25 psi (172.37 kPa), which is relatively much higher than required for most microfluidic applications and shows promise for the use of ice valves for high-pressure microfluidic applications.
- Simple conduction-based 1-D models provide a means for chip design guidelines by estimating the response time of the valve and the pitch of channels for a multichannel chip of any given material and dimensions to be used with the proposed cooling mechanism design.

The cooler design has offers great advantage over some of the existing cooling methods: firstly, it is compact and has a very small foot-print compared to thermoelectric stages; as demonstrated in Section 5.2.5.5, the small size of cooler base ensures creation of localized cold zones. The small size of the device also ensures that it is portable and can be moved around to use over multiple locations on a substrate and that multiple coolers can be used on a single substrate for simultaneous valving needs. Secondly, this design is relatively inexpensive and simple to fabricate compared to on-chip Peltier junctions. Thirdly, use of cryogen for cooling provides a readily available cooling source and also reduces the thermal mass of the system and ensures quick operation; the controlled expansion of the cryogen in the expansion chamber avoids direct contact between the chip and the cryogen which prevents undesirable freezing on the chip and also ensures safety of the user. However, while these advantages make this cooling mechanism a lucrative choice for ice valve formation, there are a few shortcomings of this method that need to be overcome for wider

application: firstly, the response times of valves formed using this mechanism are still of the order of a few seconds compared to a few milliseconds for conventional mechanical valves. Secondly, the complete integration of the cooling mechanism with the microfluidic chip design could not be achieved used this design; while the cooler body itself is portable and can move, the cooling method requires cryogen and, therefore, the cryogenic cylinder to be readily available which may be difficult to transport or arrange.

**Nomenclature**

| | |
|---|---|
| $Bi$ | Biot number |
| $H$ | chip thickness ($= x_{cover} + x_{channel} + x_{base}$) |
| $h$ | thermal heat transfer coefficient |
| $k$ | thermal conductivity |
| $L$ | length of the chip |
| $Q$ | volumetric flow rate |
| $q$ | heat transfer across the chip |
| $R$ | resistance |
| $r$ | radial position from the axis of center of the chip (Figure 5.9) |
| $T$ | temperature |
| $t$ | time |
| $W$ | width of the chip |
| $x$ | axial position from the chip top (Figure 5.8) |
| $y$ | lateral position from the axis of center of the chip, direction parallel to width (Figure 5.8) |
| $z$ | lateral position from the axis of center of the chip, direction parallel to length (Figure 5.8) |

***Greek symbols***

| | |
|---|---|
| $\alpha$ | hermal diffusivity |

***Subscripts***

| | |
|---|---|
| $\|\|$ | parallel |
| $actual$ | actual closure |
| $base$ | chip base |
| $c$ | cooler |

| | |
|---|---|
| $channel$ | channel |
| $chip$ | chip |
| $chipbase$ | base plane on the chip |
| $cl$ | closing |
| $contact$ | contact between the cooler and the chip |
| $convection$ | convection |
| $cover$ | chip cover |
| $eff$ | effective |
| $fluid$ | fluid (water) |
| $nuc$ | nucleation |
| $observed$ | visually observed in the field-of-view |
| $pitch$ | pitch distance normal from existing channel |
| $res$ | response |
| $s$ | cooler contact region |
| $W/2$ | half-width of the chip |

Table 5.1. List of the chip and channel dimensions used in the study.

| **Parameter** | **Value** | | | |
|---|---|---|---|---|
| Chip material | PMMA | | | Glass |
| Channel length ($\boldsymbol{L}$) [mm] | 87 | | | 38 |
| Chip width ($\boldsymbol{W}$) [mm] | 16.32 | | | 25.4 |
| Cover plate thickness ($\boldsymbol{x_{cover}}$) [µm] | 175 | | | 1000 |
| Base plate thickness ($\boldsymbol{x_{base}}$) [µm] | 1325 | | | 170 |
| Channel size ($\boldsymbol{x_{channel}}$) [µm] | 200 | 100 | 50 | 100 |

Table 5.2. Properties of the materials used in the model.

| **Property** | **Value** | | |
|---|---|---|---|
| Material | PMMA | Glass | Silicon |
| Density [kg/m$^3$] | 1200 | 3300 | 2329 |
| Specific heat [J/kgK] | 1500 | 890 | 710 |
| Conductivity, $\boldsymbol{k_{chip}}$ [W/mK] | 0.15 | 1 | 149 |

Table 5.3. Response times for all the test cases from the experiment, the numerical model and the analytical model.

| | | **Response time, $t_{res}$ [s]** | | | | | | |
|---|---|---|---|---|---|---|---|---|
| | | **Experiment** | **Numerical model** | | | **Analytical model** | | |
| **Cover thickness [µm]** | | **175** | **100** | **175** | **250** | **100** | **175** | **250** |
| **Chip Material** | PMMA | 39.25 | 16.6 | 25.5 | 34.0 | 10.6 | 19.0 | 24.8 |
| | Glass | 7.5 | 2.6 | 4.6 | 7.1 | 2.6 | 4.5 | 5.8 |
| | Silicon | - | 3.1 $\times 10^{-2}$ | 3.4 $\times 10^{-2}$ | 3.6 $\times 10^{-2}$ | 1.1 $\times 10^{-2}$ | 1.9 $\times 10^{-2}$ | 2.5 $\times 10^{-2}$ |

Table 5.4. Pitches calculated using the numerical and the analytical models for all the test cases.

| | | **Pitch [mm]** | | | |
|---|---|---|---|---|---|
| | | **Numerical model** | | | **Analytical model** |
| **Cover thickness [µm]** | | **100** | **175** | **250** | **-** |
| **Chip Material** | PMMA | 3.34 | 3.01 | 2.56 | 4.17 |
| | Glass | 3.71 | 3.63 | 3.54 | 6.39 |
| | Silicon | 13.56 | 13.55 | 13.34 | 35.71 |

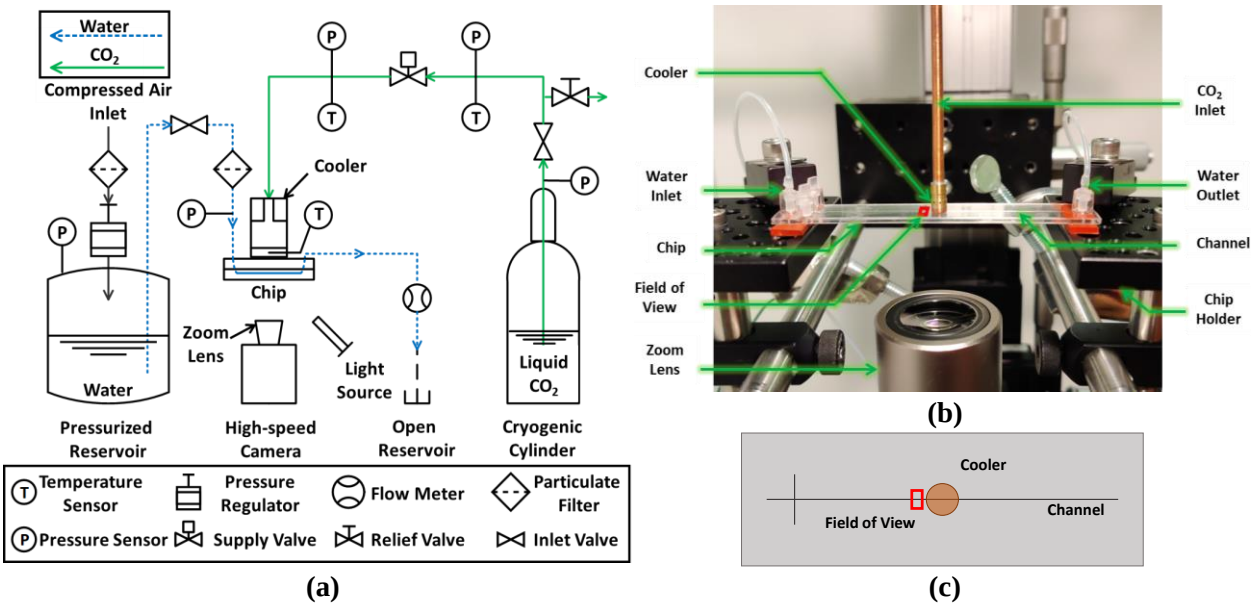


Figure 5.1. (a) Schematic diagram of the experimental test facility, (b) an image of the test setup showing the cooler in contact with the PMMA chip, and (c) schematic diagram of the chip showing relative locations of the cooler and the field-of-view of the high-speed camera.

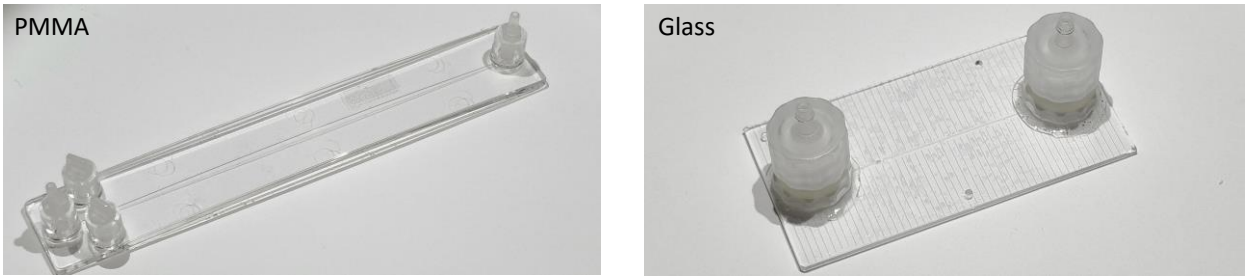


Figure 5.2. Photographs of the microfluidic chips used in the test: (a) PMMA and (b) Fused silica glass. Two of the three holes at the exit of PMMA channel are blocked using mini-luer plugs.

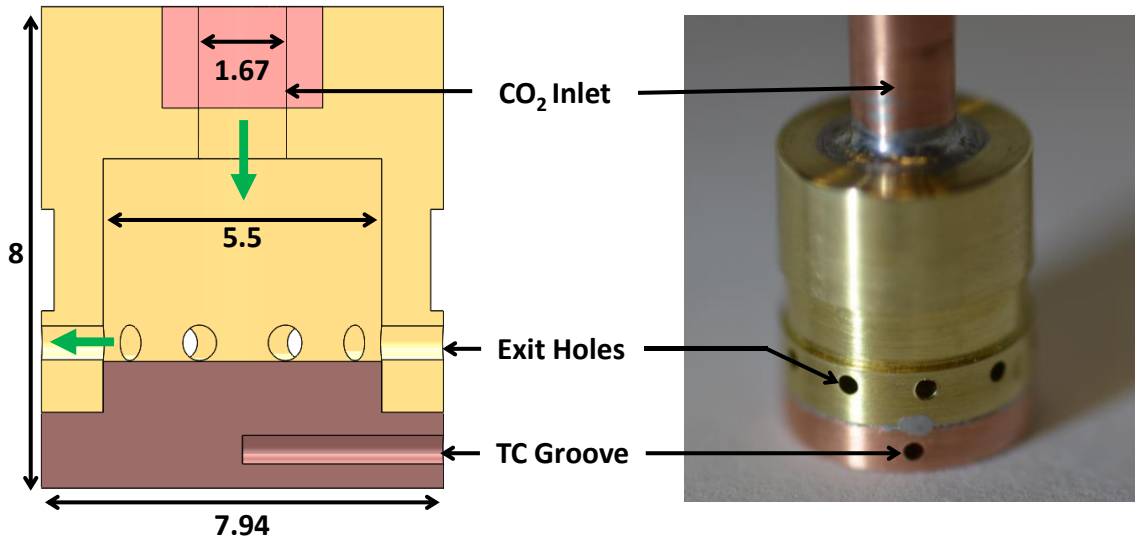


(a) (b)

Figure 5.3. (a) A cross-sectional drawing of the cooler design showing the expansion chamber and the holes and (b) an image of the cooler. Green arrows show the direction of flow of $CO_2$ through the cooler.

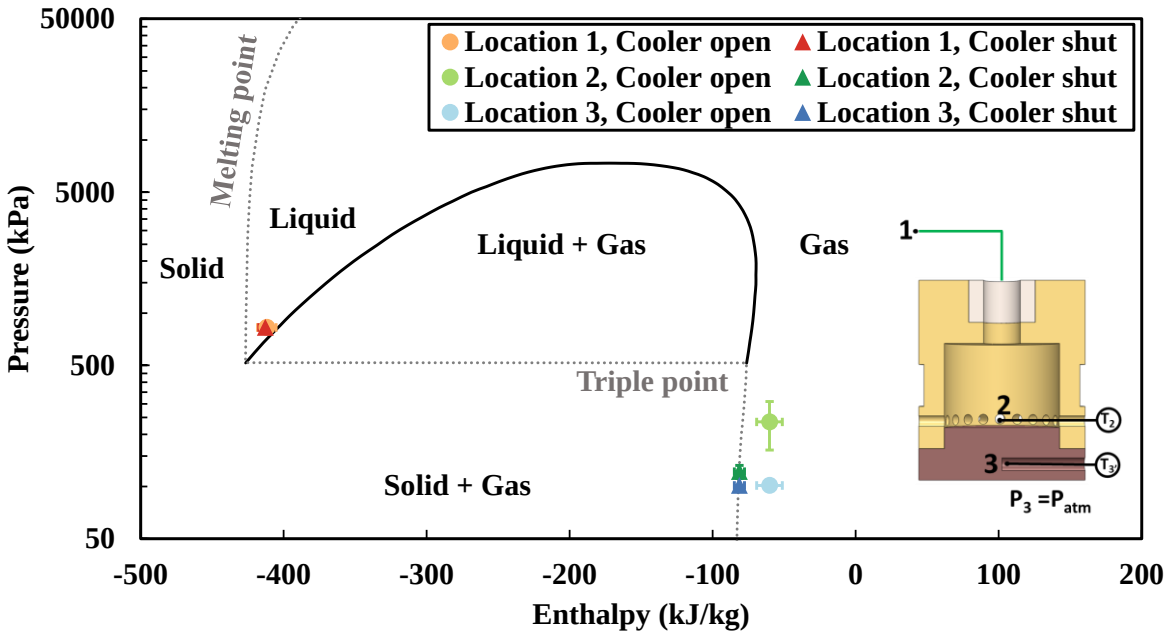


Figure 5.4. Pressure-enthalpy curve for $CO_2$ showing the values before and after the cooler is blocked by the dry ice, at the three locations shown in the inset.

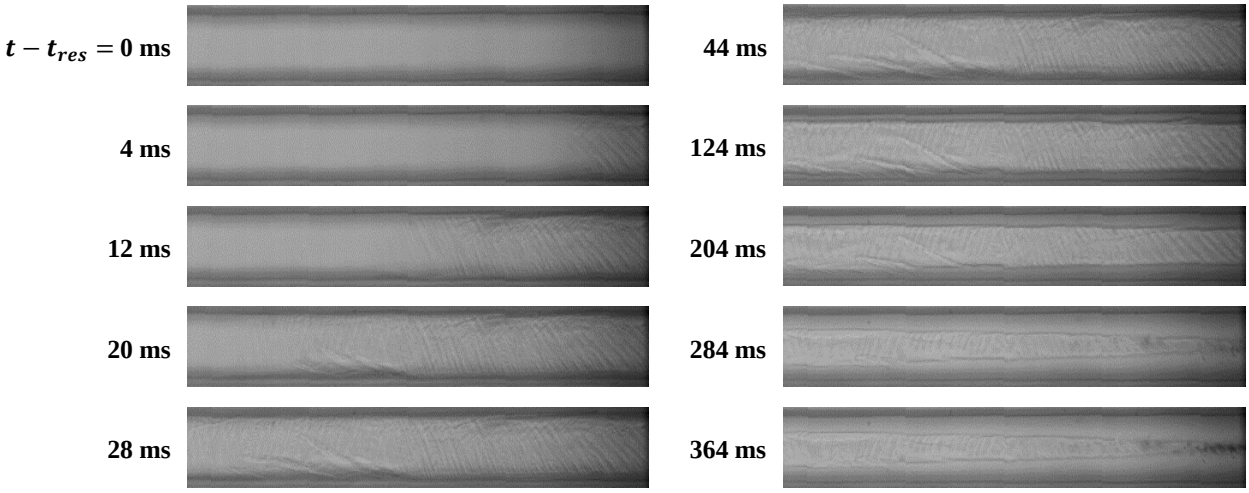


Figure 5.5. Time sequence of images showing the dendritic and annular modes of ice formation as the freezing occurs in the 200 μm channel on PMMA chip. The flow direction is from left to right. The cooler (not shown) is placed downstream of the field-of-view.

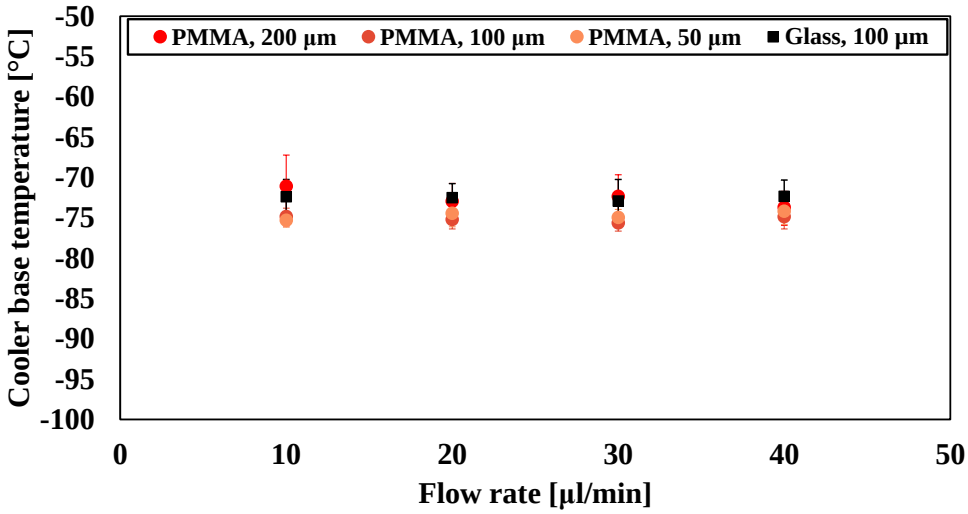


Figure 5.6. Median cooler base temperatures for the test cases at the instant of dendritic ice observation in the field-of-view over 6 repeated trials for each test case. The vertical bars show the statistical limits of the observed data for a given test case.

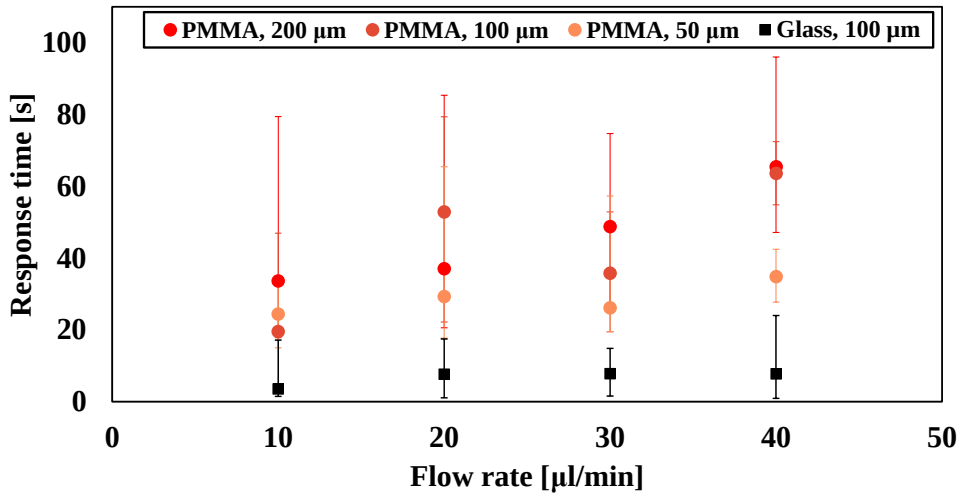


Figure 5.7. Median response times for the test over 6 repeated trials for each test case. The vertical bars show the statistical limits of the observed data for a given test case.

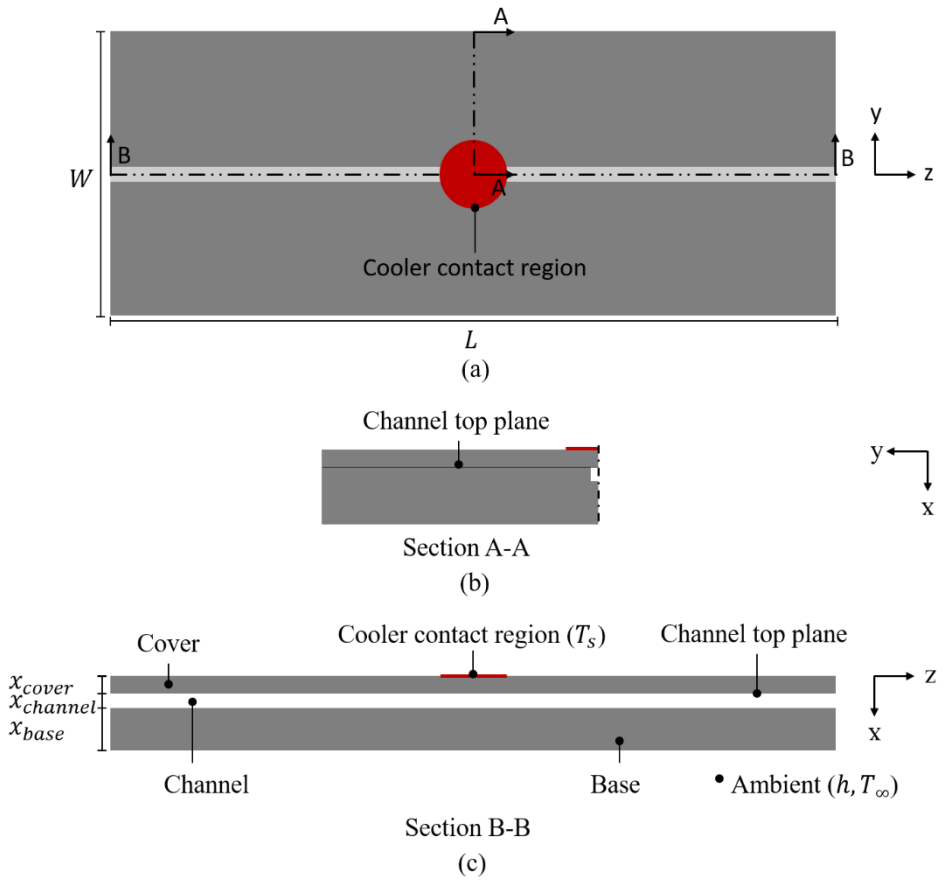


Figure 5.8. Schematic diagram illustrating (a) top view, (b) half-section in the x-y plane, and (c) cross-section in the x-z plane of the computational domain for the numerical model.

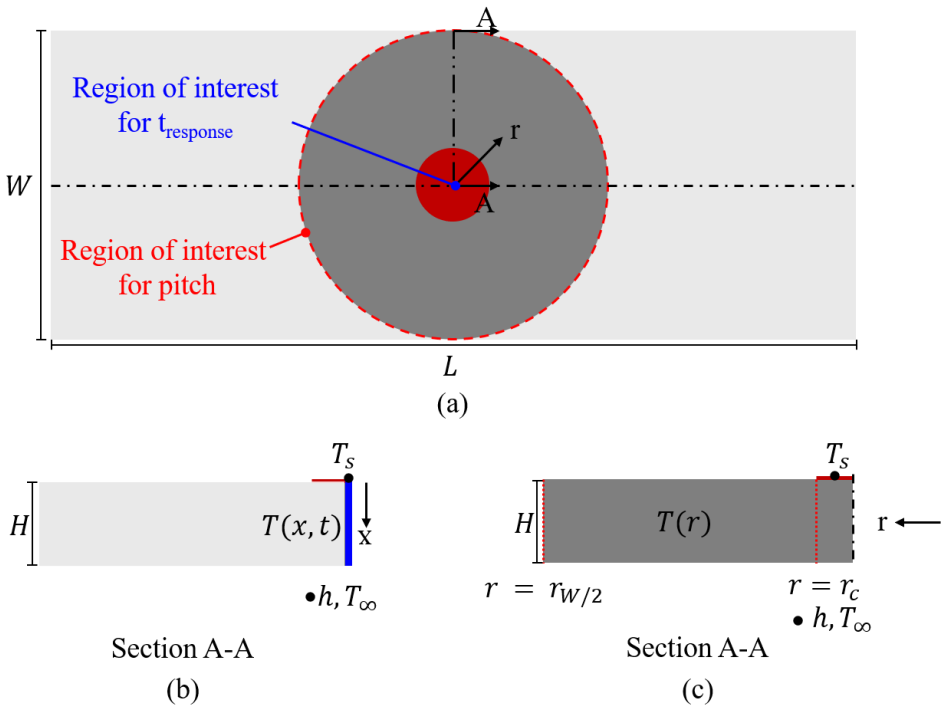


Figure 5.9. Schematic diagram illustrating (a) the regions of interest for the response time (marked in blue) and the pitch (marked in red dashed-line) calculations using analytical model, (b) region of interest and boundary conditions for response time model on half-section on x-r plane, and (c) region of interest and boundary conditions for pitch model on the half-section on x-r plane.

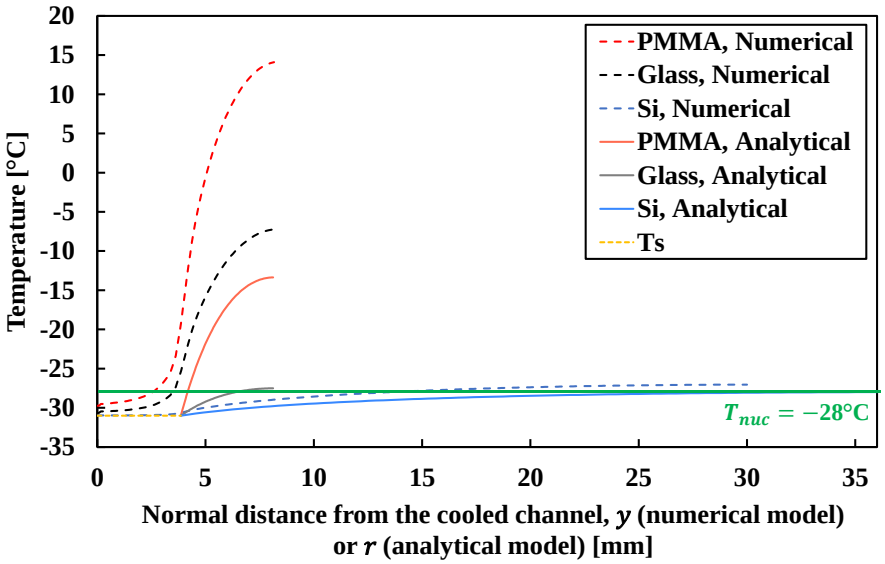


Figure 5.10. Variation in the temperature along the normal distance from the center of the cooled channel for all chip materials calculated using numerical (for $x_{cover} = 175$ μm) and analytical models. The green line marks the nucleation temperature used for calculation of pitch.

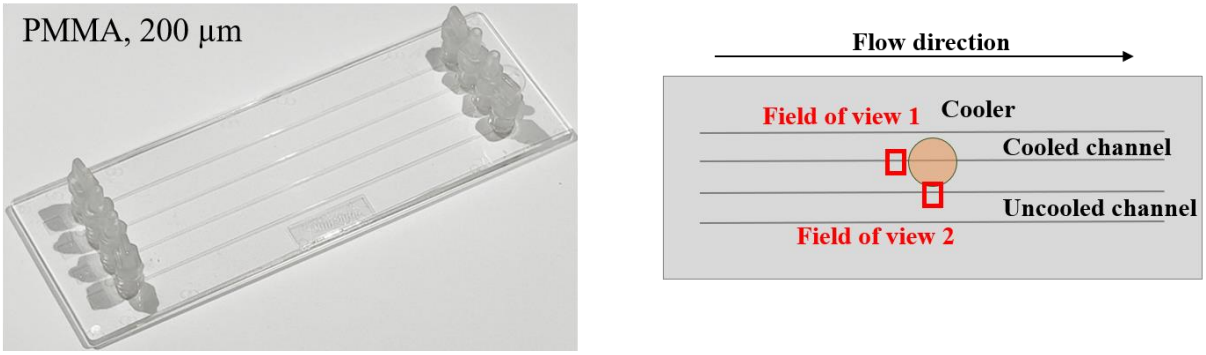


(a) (b)

Figure 5.11. (a) Image of the PMMA chip with four parallel channels and (b) schematic diagram showing the location of the fields-of-view with respect to the cooler contact region.

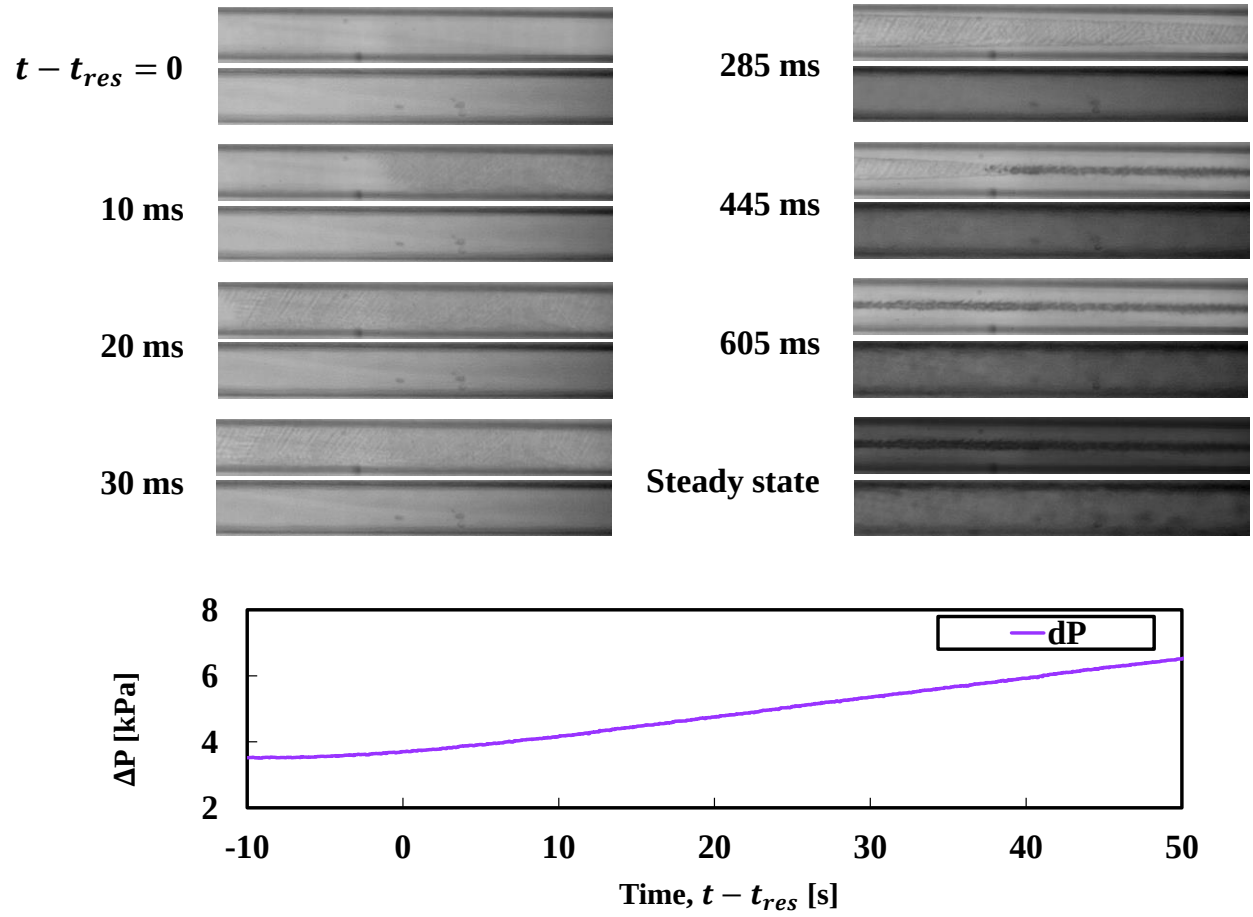


Figure 5.12. Time sequence of images showing cooled (top) and uncooled (bottom) channels as freezing occurs in the cooled channel. The bottom graph shows temporal variation in total pressure drop across both the channels as freezing occurs, which is used to verify the occurrence of closure in the cooled channel when field-of-view is on the uncooled channel.

# CHAPTER 6. SUMMARY AND FUTURE WORK

The goal of this dissertation was to develop a complete understanding of the flow freezing process occurring in microchannels, as a step towards arriving at techniques to efficiently form an ice valve for microfluidic applications. The high-speed visualization of the freezing process, in synchronization with the wall temperature and the flow rate data, allowed for observation, quantitative differentiation and characterization of different modes of ice formed during flow freezing in a glass microchannel: dendritic and annular. A simple conduction-based model was developed to understand the effect of flow rate and channel size on the growth rate of annular ice responsible for channel closure; it identified the conduction of released latent heat of fusion as the heat transfer mode governing the rate of ice formation and closure time. With an objective of developing efficient ice valve formation techniques, a novel cooling mechanism for ice valve formation in microfluidic devices was designed and its working demonstrated. It was compact enough to be interfaced with multichannel devices and was capable of precisely controlling the location of cold spot. To obtain an estimate of the response time and the channel pitch that could help develop guidelines for incorporation of the proposed cooling mechanism into chip design, the cooling process of the chip was modeled using both 3-D numerical and simplified 1-D analytical models; the 1-D model was proved to be the simpler and more accessible option to calculate the response time and the pitch for a chip design. Summarily, this study has built a strong foundation for the application of flow freezing in microchannels as a flow control mechanism in for microfluidic applications, including those with complex functionality and for high-pressure applications.

The next steps from this study should be directed towards better understanding of the fundamental flow freeing process in microchannels and developing better designs for more efficient and faster ice valve formation. A few potential next steps are presented below:

1. Measurement of the actual ice nucleation temperature is a crucial step to understand the fundamental flow freezing phenomenon. However, due to the design of the experiments presented in the study, it was difficult to measure the temperature at the inner wall of the channel, where nucleation occurred. Furthermore, any probe placed inside the channel could serve as a nucleation point itself. Thus, it is important to develop methods and experimental

facilities to obtain the nucleation temperature measurement without presenting any unwarranted effect on the nucleation process itself.

2. To completely understand the extent of the effect of flow rate on the freezing phenomenon, it is crucial to understand its effect on the nucleation temperature itself. This knowledge would specially be useful to control the supercooling and, hence, the response time, of ice valve and could present as a more efficient and sustainable way of doing so, as compared to using complex, bulky cooling methods or introducing foreign particles (INPs) to the system.
3. Although the cooling mechanism proposed in CHAPTER 5 is compact and can be interfaced with multichannel devices without causing unintentional freezing, the calculated channel-to-channel pitch is of the order of a few millimeters, which could hinder further minimization of the complex, multi-channel chips. Furthermore, the response time of the valve formation is still an order of magnitude higher than the conventional mechanical valves. Development of even more compact cooler design, with metallic cooling elements directly integrated into the chip, could possibly solve these issues without affecting the quality of the reactions or reusability of the substrate or the reagents.
4. For an active switching operation using ice valve, in addition to freezing, the valve also needs to be thawed. While thawing requires a less complex mechanism than freezing, the thawing time can be significantly higher compared to freezing time in the absence of proper heating mechanism. As the reactions on a lot of the microfluidic devices could be sensitive to heat, it is imperative that the heating mechanism does not overheat the substrate or cause unintentional heating of the chip. Thus, a proper heating mechanism needs to be developed for proper functioning of ice valve switch. Additionally, the factors affecting the thawing process also need to be studied to control and reduce the thawing times of ice valves.

# APPENDIX A. ICE FORMATION MODES DURING FLOW FREEZING IN A SMALL CYLINDRICAL CHANNEL

## A.1 Temporal Variation in the Inlet and Outlet External Channel Wall Temperatures during Freezing

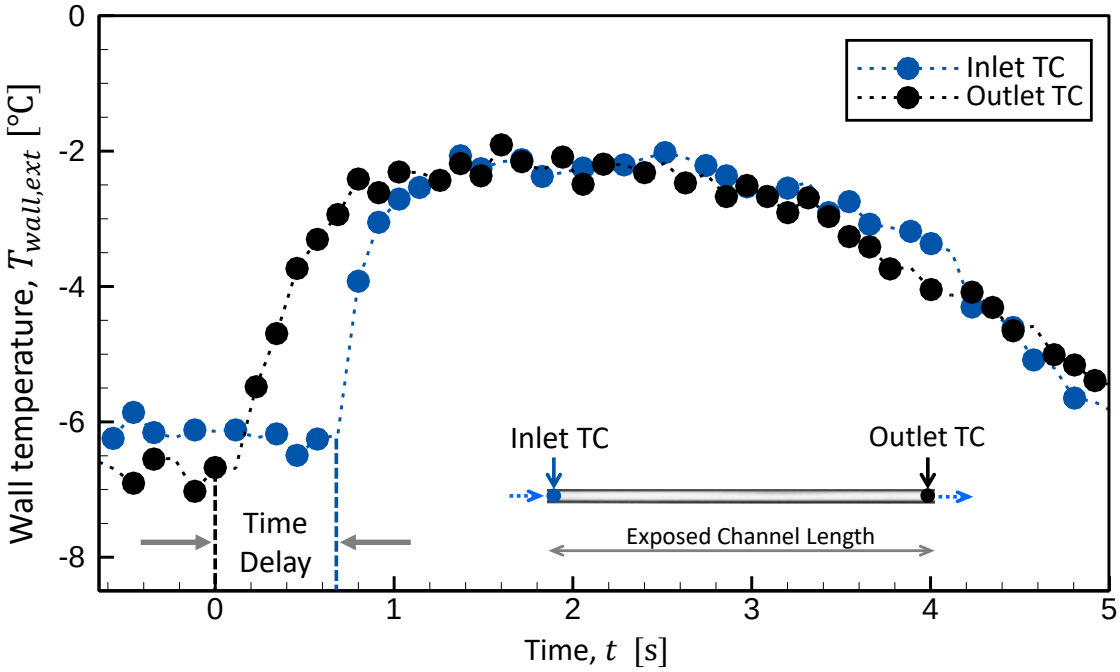


Figure A.1. Temporal variation in the channel wall temperatures positioned at the inlet and outlet, as the freezing occurs. The dendritic ice initiation is observed at $t = 0$ s. The blue and black vertical dashed lines mark the instances when temperature jump is registered by the inlet and the outlet wall thermocouples (TCs), respectively. The time difference between these instances corresponds approximately to the time taken by the dendritic ice front to move from outlet TC to inlet TC.

## A.2 Refraction Correction

A ray-tracing algorithm for the refraction correction in the high-speed images of a circular microchannel is used to transform the *y*-coordinates of the channel inside diameter ($y_5$) and the water-ice interface ($y_4$) observed in the image to their actual physical locations ($y_3$ and $y_1$, respectively), as shown in Figure 3.3(a) in the main manuscript. The channel inner wall diameter intersects with the *y*-*z* plane (mid-plane of the channel) at the top of the bright white band in the experimental image (Figure 3.3(b) in the main manuscript). The bright region can be attributed to the refraction of light rays through the channel wall. The water-ice interface intersects the *y*-*z* plane at the top of the uneven dark band in the image. The unevenness at this interface is a result of optical distortion due to the presence of dendritic ice on the inner channel wall. The dark region observed immediately below the water-ice interface is a result of total internal reflection of the light by the water-ice interfaces in the background and the foreground of the focal plane. The relation between the angle of incidence and the angle of refraction for a light ray traversing through the ice-glass and glass-gas interfaces is given by Snell's law, $n_1 sin\theta_1 = n_2 sin\theta_2$, where $n$ is the refractive index of the medium and $\theta$ is the angle between the direction normal to the interface and the incident/refracted light ray, in the respective medium. The refractive indices of ice, borosilicate glass, and nitrogen gas are 1.31, 1.47 and 1.00, respectively.

## A.3 Model Scaling Analysis

As described in the Section 3.2.2, a simple control volume-based model is used to predict the transient location of the annular interface during freezing as well as the total annulus growth duration in the channel. For the initial time step $\Delta t$, the overall energy balance equation for a single CV of axial length $\Delta z$ = $10^{-5}$ m is given by Equation $(3.5b)$ which can be recast without spatial- and time-discretization indices as:

$$\dot{m}_{in} c_{p,l}(T_{in} - T_{out}) - \dot{m}_f c_{p,l}(T_{in} - T_{out}) + \dot{m}_f c_{p,l}\left(T_{in} - T_f\right) + \dot{m}_f L + \dot{m}_f c_{p,s}\left(T_f - T_i\right) = -2\pi\Delta z \frac{\left(T_i - T_{wall,ext}\right)}{\frac{\ln\left(R_{wall,int}/R_i\right)}{k_s} + \frac{\ln\left(R_{wall,ext}/R_{wall,int}\right)}{k_{bs}}} \quad (A.1)$$

On the left-hand side, the sum of the two terms represents the sensible heat lost by the portion of water entering the CV that exits without freezing ($\dot{m}_{out}$). The third term represents the sensible energy lost by the portion of water entering the CV that freezes ($\dot{m}_f$). The fourth term is the latent

heat energy released on freezing. The last term denotes sensible energy lost by solid ice as its temperature drops from the equilibrium freezing point to the ice-water interface temperature. The last term has no effect as the ice-water interface is assumed to be at the equilibrium freezing point ($T_i = T_f$). The primary variable of interest in Equation $(A.1)$ is the growth rate of annular ice ($\Delta R_i/\Delta t$) which appears implicitly in the rate of ice formation $\dot{m}_f (= \rho_s 2\pi R_i \, (\Delta R_i/\Delta t) \, \Delta z)$. An expression for $\Delta R_i/\Delta t$ as shown in Equation $(3.5c)$ can be deduced by simplifying Equation $(A.1)$ based on a comparison of relative orders of magnitude of the above energy terms. The parameters required for estimating the orders of magnitude of these terms are listed in Table A.1 for case A.

In addition to the parameters specified in Table A.1, the difference between the water inlet and outlet temperatures for the entire channel (with 2000 CVs) is ~6.8°C, as reported in Table 3.1, and Section 3.2.2. Accordingly, this temperature difference for a single CV, $(T_{in} - T_{out})$, will at most be of the order $10^{-3}$°C, and the temperature difference between the water entering this CV and the freezing temperature $(T_{in} - T_f)$ can at most be of order 10°C. Using these inputs, the orders of magnitude of all energy terms is estimated in Table A.2. It is evident from Table A.2 that the latent heat energy is one or more orders of magnitude greater than each of the convection energy terms. Neglecting the convection energy terms reduces Equation $(A.1)$ to Equation $(3.5c)$, which shows a direct balance between the latent heat released with annular ice formation and the radial heat conduction through the annular ice layer and channel wall. In the above discussion, case A is considered as the representative case to demonstrate the order of magnitude of different energy terms but this scaling analysis is also true for cases B and C.

Table A.1. Parameters for case A used to estimate the orders of magnitude of terms appearing in Equation $(A.1)$. Parameters denoted by * are estimated based on experimental data.

| **Parameters** | **Magnitude** |
|---|---|
| $c_{p,l}$ | 4187 (J/kg-K) |
| $c_{p,s}$ | 1950 (J/kg-K) |
| $L$ | 334000 (J/kg) |
| $\rho_s$ | 916.7 (kg/m$^3$) |
| $\Delta t$ | $10^{-3}$ (s) |
| $\Delta z$ | $10^{-5}$ (m) |
| $R_0$ | 200 ($\mu$m) |
| $\frac{\Delta R_i}{\Delta t}^*$ | 100 ($\mu$m/s) |
| $R_i^* \left(= R_0 - \left(\frac{\Delta R_i}{\Delta t}\right)\Delta t\right)$ | 199.9 ($\mu$m) |
| $T_i (= T_f)$ | 0 (°C) |
| $\dot{m}_{in}^*$ | $8.35 \times 10^{-6}$ (kg/s) |
| $\dot{m}_f^* \left(= \rho_s 2\pi R_i \frac{\Delta R_i}{\Delta t}\Delta z\right)$ | $1.15 \times 10^{-9}$ (kg/s) |

Table A.2. Estimated orders of magnitude of different energy terms appearing in energy balance Equation $(3.5b)$ for case A.

| **Energy terms** | **Order of magnitude** |
|---|---|
| $\dot{m}_{in} c_{p,l}(T_{in} - T_{out})$ | $O(-5)$ |
| $\dot{m}_f c_{p,l}(T_{in} - T_{out})$ | $O(-8)$ |
| $\dot{m}_f c_{p,l}(T_{in} - T_f)$ | $O(-6)$ |
| $\dot{m}_f L$ | $O(-4)$ |

# APPENDIX B. TIME SEQUENCE OF IMAGES SHOWING FLOW FREEZING FOR MICROCHANNEL WITH $D$ = 300 $\mu$m

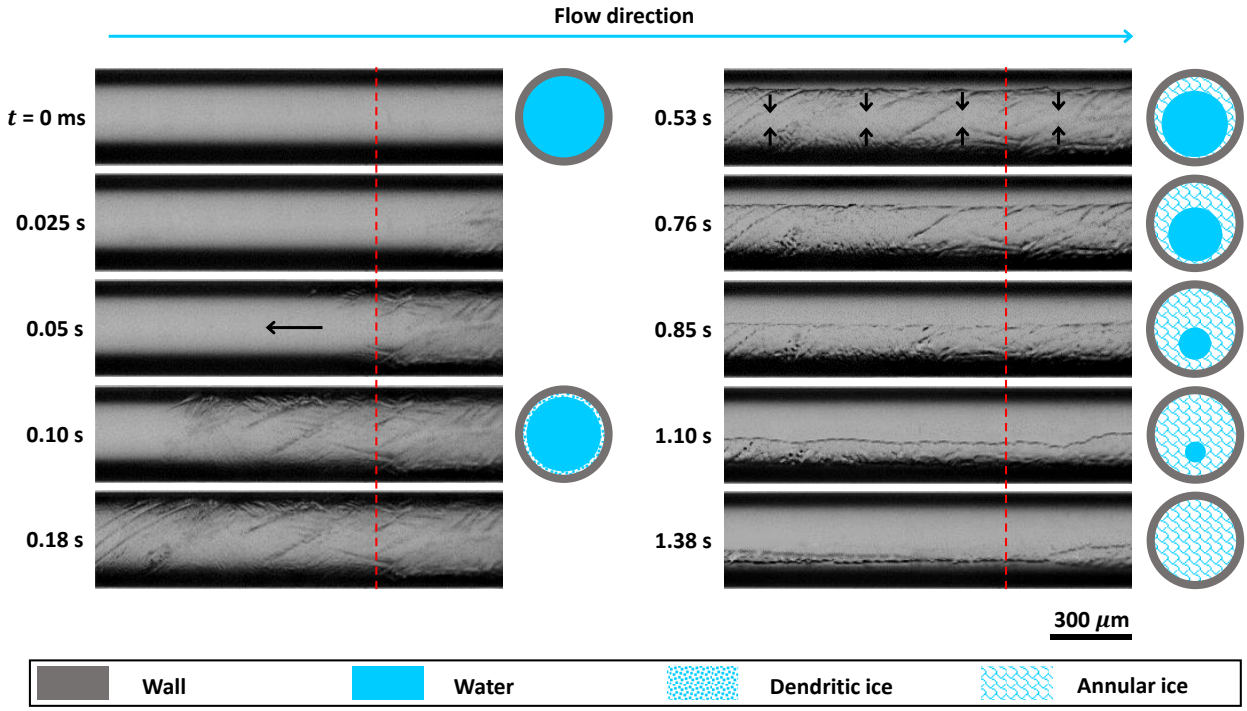


Figure B.1. Time sequence of images showing ice formation, growth and closure during flow freezing in a microchannel for $D = 300$ μm. The schematic diagrams on the right of the channel show the channel cross-section at the closure plane (dashed red line). The channel wall, water, dendritic ice, and annular ice regions are shaded as indicated in the legend. Flow direction is from left to right. The black arrows indicate the direction of ice growth.

# APPENDIX C. ESTIMATION OF CONTACT REGION TEMPERATURE, $T_s$, AND CONVECTIVE HEAT TRANSFER COEFFICIENT, $h$

A 1-D, steady-state thermal resistance network analysis is used to estimate the heat transfer between the cooler base and the ambient through the chip to get an estimate of $T_s$ and $h$ during the test. Figure C.1. (a) and (b) show a schematic diagram of the section over which the analysis is performed and the corresponding thermal resistance network, respectively. The heat transfer across the chip can be written as:

$$q = \frac{T_{coolerbase} - T_\infty}{R_{total}} \tag{C.1}$$

where

$$R_{total} = R_{contact} + R_{cover} + R_{channel,eff} + R_{base} + R_{convection} \tag{C.2}$$

Assuming no heat loss in the chip, the heat transfer across the thermal resistance network can be further written as:

$$q = \frac{T_s - T_{chipbase}}{R_{base} + R_{channel,eff}} = \frac{T_{chipbase} - T_\infty}{R_{convection}} \tag{C.3}$$

where

$$R_{cover} = \frac{x_{cover}}{k_{chip} A_c} \tag{C.4}$$

$$R_{base} = \frac{x_{base}}{k_{chip} A_c} \tag{C.5}$$

$$R_{channel} = \frac{x_{channel}}{k_{fluid} A_{channel}} \tag{C.6}$$

$$R_{||} = \frac{x_{channel}}{k_{chip}(A_c - A_{channel})} \tag{C.7}$$

$$R_{convection} = \frac{1}{hA_c} \tag{C.8}$$

And

$$\frac{1}{R_{channel,eff}} = \frac{1}{R_{channel}} + \frac{1}{R_{||}} \tag{C.9}$$

$R_{channel,eff}$ is the effective resistance of across the channel thickness, as the heat flows through parallel paths via the channel and the chip material adjacent to the channel. However, since the area of the channel is very small compared to the total area of the cooler ($\frac{A_{channel}}{A_c} = \frac{2x_{cover}}{\pi r_c} = 0.02 - 0.04$), resistance of the channel path is much larger compared to the resistance of the parallel path. Therefore, it can be reasonably assumed that all the heat flows through the chip, i.e., $R_{channel,eff} \sim R_{channel}$. This also implies that the channel size and the flow rate effects can be neglected in the calculations for simplicity.

To get an estimate of $T_s$ and $h$, a thermocouple is attached to the base of the chip, underneath the cooler using a thermally conductive paste to ensure proper thermal contact (see Figure C.1. (a)); a new set of experiments is performed using the same experimental procedure, as described in Section 5.1.3 in CHAPTER 5, using both PMMA and glass chips. Since the channel effects are negligible in the analysis, the water flow is kept stagnant. The measurements are taken until the system reaches a steady state (the standard deviation in the chip base temperature reading over 5 minutes is less than 1°C). The measured values of steady-state temperatures from the experiment for each chip material at (listed in Table C.1) are then plugged into Equations ($C.1$) and ($C.3$); a value of $h$ is guessed and these corresponding $T_s$ is calculated. These values are plugged in the numerical model to calculate the rate of change of base temperature from the instant of cooler contact ($t = 0$), which is then compared with the chip base cooling rate from the experiments. This guessing process is repeated until, for a value of $h$ and corresponding $T_s$, the results from the models match the experimental results very closely, i.e., starting from the same initial base temperature, the models have similar rates of reduction of the chip base temperature and have the approximately same value at the steady state. This analysis estimates a value of $h = 9.7$ W/mK and $T_s = -31$°C for PMMA chip and $T_s = -43$°C for the glass chip.

Similarly, solving Equation ($C.5$) in the main manuscript for $x = H$ for the estimated values of $h$ and $T_s$ gives the transient variation of the chip base temperature. A comparison of the transient chip base temperatures between the 1-D axial analytical model, the numerical model, and the experimental results shows reasonable match between the three (Figure C.2).

For further simplification of the models, firstly, all the cases are run with same values of heat transfer coefficient ($h = 9.7$ W/mK) and cooler contact region temperature ($T_s = -31$°C), and secondly, the channel size and the flow rate effects can be neglected in the calculations for simplicity. Furthermore, as can be seen in Figure C.2, the cooler base temperature remains approximately constant throughout the test; it is reasonable to assume that the contact resistance also does not change during the test. Therefore, the assumption that $T_s$ is a constant during the text is justified.

Table C.1. Steady-state temperatures measured experimentally for each chip material.

| **Parameter** | **Value** | |
|---|---|---|
| Material | PMMA | Glass |
| $\boldsymbol{T}_{\infty}$ [°C] | 23.00 | 23.00 |
| $\boldsymbol{T}_{\boldsymbol{coolerbase}}$ [°C] | – 72.14 | – 72.10 |
| $\boldsymbol{T}_{\boldsymbol{chipbase}}$ [°C] | – 25.52 | – 42.85 |
| $\boldsymbol{T}_{\boldsymbol{initial}}$ [°C] | 7.99 | – 5.40 |

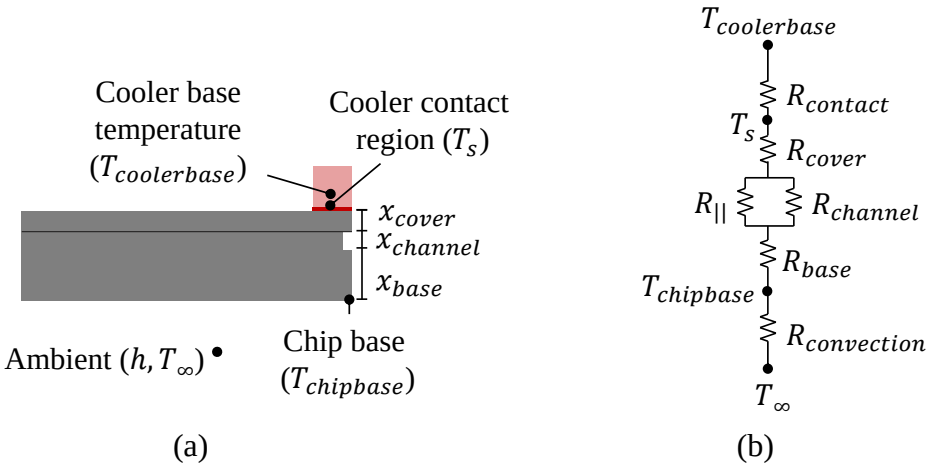


Figure C.1. Schematic diagram showing (a) section A-A of the chip geometry used for the resistance network analysis and (b) thermal resistance diagram for the geometry.

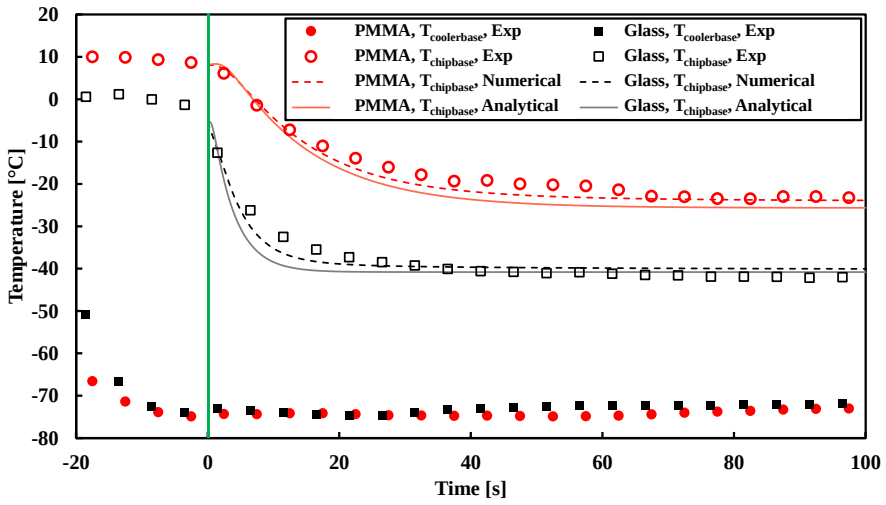


Figure C.2. Comparison of the rate of change of base temperature between the analytical, the numerical and the experimental results. The vertical green line marks the instant of cooler contact ($t = 0$).

# APPENDIX D. LIST OF MAJOR COMPONENTS AND EQUIPMENT

| Component | Manufacturer | Model number |
|---|---|---|
| Optical table | Newport | VH3648W-OPT |
| Pressure regulator | Omega | PRG200-25 |
| Pressure transducer | Omega | PX302-015GV |
| Pressure transducer | McMaster-Carr | 4000K222 |
| Pressure transducer | Wika | Transmitter S-10 |
| Pressure transducer | Wika | Transmitter S-10 |
| Liquid flow meter | Alicat | LC-5CCM-D |
| Microturbine gas flow sensor | Cole Parmer | FF-00368-KV |
| Borosilicate glass channel | Vitrocom | CV5070 |
| Borosilicate glass channel | Vitrocom | CV3040 |
| Borosilicate glass channel | Vitrocom | CV1017 |
| Adjustable DC power supply | Sorensen | DCS40-25E |
| Adjustable DC power supply | Sorenson | XG 100-8.5 |
| Adjustable DC power supply | MPJA | 29601 PS |
| Constant DC power supply | TDK-Lambda | LS50-24 |
| Data acquisition unit | Fluke | NetDAQ 2640A |
| Data acquisition unit | National Instruments | cDAQ-9178 |
| Data acquisition unit | Agilent | 34970A |
| Shunt resistors | Empro | HA 5 100 |
| High-speed camera | Phantom | VEO 710L |
| High-magnification zoom lens | Keyence | VHZ50L |
| High-magnification zoom lens | Keyence | VHZ100L |
| Back light | Advanced Illumination | BL138 |
| Pulse generator | Berkeley Nucleonics Corporation | Model 565-8C-H |
| Pulse generator | Berkeley Nucleonics Corporation | Model 505-4C |
| RTD | Sifang | WZP-100-1/16 |
| Xenon lamp | Sunoptics Technologies | Titan X300 |

| | | |
|---|---|---|
| Relief valve | Ratermann | PR-600 |
| Single channel PMMA chip | microfluidic ChipShop GmbH | 02-0752-0201-01 |
| Single channel PMMA chip | microfluidic ChipShop GmbH | 02-0756-0166-01 |
| Single channel PMMA chip | microfluidic ChipShop GmbH | 02-0773-0394-01 |
| Four channel PMMA chip | microfluidic ChipShop GmbH | 01-0172-0156-01 |
| Single channel Glass chip | Translume Inc. | SC-BU-100100-L |
| Thermocouple | Omega | TJ36-CPIN-116G-12 |
| Thermocouple | Omega | 5TC-TT-T-36-36 |
| Thermocouple | Omega | 5TC-TT-T-40-36 |
| Ice point | Omega | TRCIII |
| 1-D stage | Parker | 4414 |
| 1-D stage | Parker | 4414 |
| 1-D stage | Newport | 38 |
| 1-D stage | Newport | 38 |
| 1-D stage | Newport | 38 |

# REFERENCES


[1] S. M. Kim, S. H. Lee, and K. Y. Suh, Cell research with physically modified microfluidic channels: A review, Lab on a Chip 8 (7) (2008) 1015–1023.

[2] H. Andersson and A. van den Berg, Microfluidic devices for cellomics: a review, Sensors and Actuators B: Chemical 92 (3) (2003) 315–325.

[3] A. J. deMello, Control and detection of chemical reactions in microfluidic systems, Nature 442 (7101) (2006) 394–402.

[4] R. C. R. Wootton and A. J. deMello, Microfluidics: analog-to-digital drug screening, Nature 483 (7387) (2012) 43.

[5] T. Thorsen, S. J. Maerkl, and S. R. Quake, Microfluidic large-scale integration, Science 298 (5593) (2002) 580–584.

[6] K. W. Oh, C. H. Ahn, A review of microvalves, Journal of Micromechanics and Microengineering 16(5) (2006) R13.

[7] L. Gui and J. Liu, Ice valve for a mini/micro flow channel, Journal of Micromechanics and Microengineering 14 (2) (2004) 242.

[8] H. Jerman, Electrically activated normally closed diaphragm valves, Journal of Micromechanics and Microengineering 4 (4) (1994) 210.

[9] H. Kahn, M. A. Huff, and A. H. Heuer, The TiNi shape-memory alloy and its applications for MEMS, Journal of Micromechanics and Microengineering 8 (3) (1998) 213.

[10] D. C. Roberts, H. Li, J. L. Steyn, O. Yaglioglu, S. M. Spearing, M. A. Schmidt, and N. W. Hagood, A piezoelectric microvalve for compact high-frequency, high-differential pressure hydraulic micropumping systems, Journal of Microelectromechanical Systems 12 (1) (2003) 81–92.

[11] P. Shao, Z. Rummler, and W. K. Schomburg, Polymer micro piezo valve with a small dead volume, Journal of Micromechanics and Microengineering 14 (2) (2004) 305.

[12] B. Bae, N. Kim, H. Kee, S.-H. Kim, Y. Lee, S. Lee, and K. Park, Feasibility test of an electromagnetically driven valve actuator for glaucoma treatment, Journal of Microelectromechanical Systems 11 (4) (2002) 344–354.

[13] X. Q. Wang, Q. Lin, Y. C. Tai, A parylene micro check valve, IEEE International MEMS 99 Conference, Twelfth IEEE International Conference on Micro Electro Mechanical Systems, Orlando, FL, USA (1999) 177–182.

[14] Q. Luo, S. Mutlu, Y. B. Gianchandani, F. Svec, and J. M. J. Fréchet, Monolithic valves for microfluidic chips based on thermoresponsive polymer gels, Electrophoresis 24 (21) (2003) 3694–3702.

[15] D. J. Beebe, J. S. Moore, J. M. Bauer, Q. Yu, R. H. Liu, C. Devadoss, and B.-H. Jo, Functional hydrogel structures for autonomous flow control inside microfluidic channels, Nature 404 (6778) (2000) 588.

[16] Y. Liu, C. B. Rauch, R. L. Stevens, R. Lenigk, J. Yang, D. B. Rhine, and P. Grodzinski, DNA amplification and hybridization assays in integrated plastic monolithic devices, Analytical Chemistry 74 (13) (2002) 3063–3070.

[17] R. H. Liu, J. Bonanno, J. Yang, R. Lenigk, and P. Grodzinski, Single-use, thermally actuated paraffin valves for microfluidic applications, Sensors and Actuators B: Chemical 98 (2004) 328–336.

[18] R. Pal, M. Yang, B. N. Johnson, D. T. Burke, and M. A. Burns, Phase change microvalve for integrated devices, Analytical Chemistry 76 (13) (2004) 3740–3748.

[19] C. D. Bevan and I. M. Mutton, Freeze-thaw flow management: a novel concept for high-performance liquid chromatography, capillary electrophoresis, electrochromatography and associated techniques, Journal of Chromatography A 697 (1995) 541–548.

[20] L. Gui, B. Y. Yu, C. L. Ren, and J. P. Huissoon, Microfluidic phase change valve with a two-level cooling/heating system, Microfluidics and Nanofluidics 10 (2) (2011) 435–445.

[21] Y. He, Y. H. Zhang, and E. S. Yeung, Capillary-based fully integrated and automated system for nanoliter polymerase chain reaction analysis directly from cheek cells, Journal of Chromatography. A 924 (1–2) (2001) 271–284.

[22] Z. Chen, J. Wang, S. Qian, and H. H. Bau, Thermally-actuated, phase change flow control for microfluidic systems, Lab on a Chip 5 (11) (2005) 1277–1285.

[23] C. Si, S. Hu, X. Cao, and W. Wu, High response speed microfluidic ice valves with enhanced thermal conductivity and a movable refrigeration source, Scientific Reports 7 (2017) 40570.

[24] A. E. Sgro and D. T. Chiu, Droplet freezing, docking, and the exchange of immiscible phase and surfactant around frozen droplets, Lab Chip 10 (14) (2010) 1873–1877.

[25] S. M. Moore, Separation and identification techniques for membrane proteins using ultra-high pressure liquid chromatography coupled to mass spectrometry, University of North Carolina, Chapel Hill, NC, 2016.

[26] J. Schaible, J. Vollmer, R. Zengerle, H. Sandmaier, and T. Strobelt, Electrostatic microvalves in silicon with 2-way-function for industrial applications, Transducers ’01 Eurosensors XV, Springer, Berlin, Heidelberg, 2001, 900–903.

[27] J. C. Gaiteri, W. H. Henley, N. A. Siegfried, T. H. Linz, and J. M. Ramsey, Use of ice-nucleating proteins to improve the performance of freeze–thaw valves in microfluidic devices, Analytical Chemistry 89 (11) (2017) 5998–6005.

[28] R. P. Welle and B. S. Hardy, Peltier-actuated microvalve performance optimization, ICT 2005. 24th International Conference on Thermoelectrics, Clemson, South Carolina, 2005, 343–346.

[29] J. C. Anderson and R. P. Welle, Thermally-actuated microfluidic systems, JALA: Journal of the Association for Laboratory Automation 13 (2) (2008) 65–72.

[30] G. C. Gerhardt, E. S. P. Bouvier, and T. Dourdeville, Fluid flow control freeze/thaw valve for narrow bore capillaries or microfluidic devices, US6557575B1, 06-May-2003.

[31] P. V. Hobbes, Ice Physics, Oxford University Press, Oxford, New York (2010).

[32] M. Akyurt, G. Zaki, and B. Habeebullah, Freezing phenomena in ice–water systems, Energy Conversion and Management 43 (14) (2002) 1773–1789.

[33] M. E. Sahagian and H. D. Goff, Fundamental aspects of the freezing process, Freezing Effects on Food Quality, Marcel Dekker, New York, (1996) 1–50.

[34] N. E. Dorsey, The freezing of supercooled water, Transactions of the American Philosophical Society 38 (3) (1948) 247–328.

[35] R. R. Gilpin, The effects of dendritic ice formation in water pipes, International Journal of Heat and Mass Transfer 20 (6) (1977) 693–699.

[36] R. R. Gilpin, The effect of cooling rate on the formation of dendritic ice in a pipe with no main flow, Journal of Heat Transfer 99 (3) (1977) 419–424.

[37] R. R. Gilpin, A study of factors affecting the ice nucleation temperature in a domestic water supply, The Canadian Journal of Chemical Engineering 56 (4) (1978) 466–471.

[38] R. R. Gilpin, Modes of ice formation and flow blockage that occur while filling a cold pipe, Cold Regions Science and Technology 5 (2) (1981) 163–171.

[39] H. Inaba, K. Takeya, and S. Nozu, Fundamental study on continuous ice making using flowing supercooled water, JSME International Journal Series B 37 (2) (1994) 385–393.

[40] S. L. Braga and J. J. Milón, Visualization of dendritic ice growth in supercooled water inside cylindrical capsules, International Journal of Heat and Mass Transfer 55 (13–14) (2012) 3694–3703.

[41] N. DesRuisseaux and R. D. Zerkle, Freezing of hydraulic systems, The Canadian Journal of Chemical Engineering 47 (3) (1969) 233–237.

[42] F. B. Cheung and J. L. Baker, Transient freezing of liquids in tube flow, Nuclear Science and Engineering 60 (1) (1976) 1–9.

[43] R. Conde, M. T. Parra, F. Castro, J. M. Villafruela, M. A. Rodríguez, and C. Méndez, Numerical model for two-phase solidification problem in a pipe, Applied Thermal Engineering 24 (17) (2004) 2501–2509.

[44] E. P. Martinez and R. T. Beaubouef, Transient freezing in laminar tube-flow, The Canadian Journal of Chemical Engineering 50 (4) (1972) 445–449.

[45] T. G. Myers and J. Low, An approximate mathematical model for solidification of a flowing liquid in a microchannel, Microfluidics and Nanofluidics 11 (4) (2011) 417–428.

[46] T. A. Dourdeville, US Patent No. 7128081B2, 2006.

[47] C. Neumann, A. Voigt, and B. E. Rapp, A large scale thermal microfluidic valve platform, 15th International Conference on Miniaturized Systems for Chemistry and Life Sciences, Seattle, Washington, 2011, 177-186.

[48] J. M. Ramsey, W. H. Henley, and J. C. Gaiteri, US Patent No. 20180200720, 2018.

[49] H. Tan and E. S. Yeung, Automation and integration of multiplexed on-line sample preparation with capillary electrophoresis for high-throughput DNA sequencing, Analytical Chemistry 70 (19) (1998) 4044–4053.

[50] G. C. Gerhardt and T. A. Dourdeville, US Patent No. 20060053807A1, 2006.

[51] H. Becker, A New Era for Lab-on-a-Chip Technologies?, The Column 11 (7) (2015) 2-5.

[52] A. Zotou, An overview of recent advances in HPLC instrumentation, Open Chemistry 10 (3) (2012).

[53] S. Fletcher and K. Schug, HPLC troubleshooting - autosampler, column & detector issues, https://www.chromacademy.com/hplc_troubleshooting_autosampler_column_detector_issues_Essential_Guide.html.

[54] J. Cheng, L. J. Kricka, E. L. Sheldon, and P. Wilding, Sample preparation in microstructured devices, Microsystem Technology in Chemistry and Life Science, Berlin, Heidelberg, 1998, 215–231.

[55] G. Desmet and S. Eeltink, Fundamentals for LC miniaturization, Analytical Chemistry 85 (2) (2013) 543–556.

[56] H. Yin, K. Killeen, R. Brennen, D. Sobek, M. Werlich, and T. van de Goor, Microfluidic chip for peptide analysis with an integrated HPLC column, sample enrichment column, and nanoelectrospray tip, Analytical Chemistry 77 (2) (2005) 527–533.

[57] H. Yin and K. Killeen, The fundamental aspects and applications of Agilent HPLC-chip, Journal of Separation Science 30 (10) (2007) 1427–1434.

[58] A. Chen, J. J. Lu, C. Gu, M. Zhang, K. B. Lynch, and S. Liu, Combining selection valve and mixing chamber for nanoflow gradient generation: Toward developing a liquid chromatography cartridge coupled with mass spectrometer for protein and peptide analysis, Analytica Chimica Acta 887 (2015) 230–236.

[59] B. J. Kirby, D. S. Reichmuth, R. F. Renzi, T. J. Shepodd, and B. J. Wiedenman, Microfluidic routing of aqueous and organic flows at high pressures: fabrication and characterization of integrated polymer microvalve elements, Lab on a Chip 5 (2) (2005) 184–190.

[60] E. F. Hasselbrink, T. J. Shepodd, and J. E. Rehm, High-pressure microfluidic control in lab-on-a-chip devices using mobile polymer monoliths, Analytical Chemistry 74 (19) (2002) 4913–4918.

[61] B. J. Kirby, T. J. Shepodd, and E. F. Hasselbrink, Voltage-addressable on/off microvalves for high-pressure microchip separations, Journal of Chromatography A 979 (1–2) (2002) 147–154.

[62] D. S. Reichmuth, T. J. Shepodd, and B. J. Kirby, On-chip high-pressure picoliter injector for pressure-driven flow through porous media, Analytical Chemistry 76 (17) (2004) 5063–5068.

[63] G. Sharma, S. Svensson, S. Ogden, L. Klintberg, and K. Hjort, High-pressure stainless steel active membrane microvalves, Journal of Micromechanics and Microengineering 21 (7) (2011) 075010.

[64] S. Ogden, R. Bodén, and K. Hjort, A latchable valve for high-pressure microfluidics, Journal of Microelectromechanical Systems 19 (2) (2010) 396–401.

[65] I. F. Pinto, D. R. Santos, R. R. G. Soares, M. R. Aires-Barros, V. Chu, A. M. Azevedo, and J. P. Conde, A regenerable microfluidic device with integrated valves and thin-film photodiodes for rapid optimization of chromatography conditions, Sensors and Actuators B: Chemical 255 (2018) 3636–3646.

[66] A. Jain, A. Miglani, Y. Huang, J. A. Weibel, and S. V. Garimella, Ice formation modes during flow freezing in a small cylindrical channel, International Journal of Heat and Mass Transfer 128 (2019) 836–848.

[67] T. A. Kingston, J. A. Weibel, S. V. Garimella, An experimental method for controlled generation and characterization of microchannel slug flow boiling, International Journal of Heat and Mass Transfer 106 (2017) 619–628.

[68] C. S. Lindenmeyer, G. T. Orrok, K. A. Jackson, and B. Chalmers, Rate of growth of ice crystals in supercooled water, The Journal of Chemical Physics 27 (3) (1957) 822–822.

[69] W. Kong and H. Liu, A theory on the icing evolution of supercooled water near solid substrate, International Journal of Heat and Mass Transfer 91 (2015) 1217–1236.

[70] J. G. Vlahakis and A. J. Bardhun, Growth rate of an ice crystal in flowing water and salt solutions, AIChE Journal 20 (3) (1974) 581–591.

[71] A. Jain, A. Miglani, J. A. Weibel, and S. V. Garimella, The effect of channel diameter on flow freezing in microchannels, International Journal of Heat and Mass Transfer (2020), *in review.*

[72] H. R. Pruppacher, Growth modes of ice crystals in supercooled water and aqueous solutions, Journal of Glaciology 6 (47) (1967) 651–662.

[73] A. Jain, Y. Huang, J. A. Weibel, and S. V. Garimella, Visualization of ice formation modes and flow blockage during freezing of water flowing in a microchannel, ASME 2016 Heat Transfer Summer Conference, Washington, DC, USA (2016) paper HT2016–7243.

[74] A. Alizadeh *et al.*, Dynamics of Ice Nucleation on Water Repellent Surfaces, Langmuir 28 (6) (2012) 3180–3186.

[75] E. J. Langham and B. J. Mason, The Heterogeneous and Homogeneous Nucleation of Supercooled Water, Proceedings of the Royal Society of London. Series A, Mathematical and Physical Sciences 247 (1251) (1958) 493–504.

[76] N. H. Fletcher, Size Effect in Heterogeneous Nucleation, The Journal of Chemical Physics 29 (3) (1958) 572–576.

[77] Z. Zhang and X.-Y. Liu, Control of ice nucleation: freezing and antifreeze strategies, Chemical Society Reviews 47 (18) (2018) 7116–7139.

# VITA

Aakriti Jain received her Bachelor of Technology degree in 2013 from Indian Institute of Technology Kharagpur, India. She is currently pursuing her Ph.D. in Mechanical Engineering at Purdue University under the advisement of Dr. Suresh V. Garimella and Dr. Justin A. Weibel. Her research interests include design, experimental testing and characterization of ice formation in microchannels for flow control applications in microfluidic devices. She was the recipient of the Frederick N. Andrews Fellowship for outstanding PhD-track students, awarded by the Graduate School at Purdue University.

# PUBLICATIONS

A. Jain, J. A. Weibel, and S. V. Garimella, Ice valve formation mechanism for microfluidic devices, *in preparation.*

A. Jain, A. Miglani, J. A. Weibel, and S. V. Garimella, The effect of channel diameter on flow freezing in microchannels, International Journal of Heat and Mass Transfer (2020), *in review.*

A. Jain, A. Miglani, Y. Huang, J. A. Weibel, and S. V. Garimella, Ice formation modes during flow freezing in a small cylindrical channel, International Journal of Heat and Mass Transfer 128 (2019) 836–848.

A. Jain, Y. Huang, J. A. Weibel, and S. V. Garimella, Visualization of Ice Formation Modes and Flow Blockage During Freezing of Water Flowing in a Microchannel, ASME 2016 Heat Transfer Summer Conference, Washington, DC, USA (2016) paper HT2016–7243.